Edge fast-ion transport study using passive FIDA spectroscopy at the ASDEX Upgrade tokamak

Anton Jansen van Vuuren

München 2020

Edge fast-ion transport study using passive FIDA spectroscopy at the ASDEX Upgrade tokamak

Anton Jansen van Vuuren

Dissertation

der Fakultät für Physik
der Ludwig–Maximilians–Universität
München

durchgeführt am
Max–Planck–Institut für Plasmaphysik,
Garching bei München

vorgelegt von
Anton Jansen van Vuuren
aus Pretoria

München, den 16. April 2020

Erstgutachter: Prof. Dr. Hartmut Zohm
Zweitgutachter: Prof. Dr. Harald Lesch
Tag der mündlichen Prüfung: 08.06.2020

Zusammenfassung

Guter Einschluss schneller supra-thermischer Ionen ist wichtig in Fusions-Experimenten, da die schnellen Teilchen das Hintergrund-Plasma heizen und zum Stromtrieb beitragen können. Darüber hinaus würden schlecht eingeschlossene schnellen Ionen nicht nur die Leistung eines möglichen Kraftwerks beeinträchtigen, sondern möglicherweise auch Wandkomponenten beschädigen. Daher ist insbesondere im Randbereich von Fusionplasmen guter Einschluss wichtig denn hier könnten bereits schwache Störungen ausreichen um schnelle Ionen auf sog. offene Feldlinien umzuverteilen. Eine bekannte Instabilität am Rand von Fusion Plasmen sind sog. Edge Localized Modes (ELM) welche Wärme, Teilchen und Impuls periodisch umverteilen. Jedoch ist hierbei noch nicht vollkommen geklärt wie stark der Einfluss von ELMs auf die schnellen Teilchen ist.

Für die Untersuchung von schnellen Ionen am Plasmarand wurden im Rahmen dieser Doktorarbeit passive Fast-Ionen-Deuterium-Alpha (FIDA) Messungen entwickelt und am ASDEX Upgrade Tokamak angewendet. Die FIDA Technik basiert auf der spektroskopischen Untersuchung der Balmer-Alpha Emissionslinie, welche von schnellen Ionen nach Ladungsaustausch-Reaktionen mit Hintergrund-Neutralen emittiert wird. Die hohe Geschwindigkeit der energetischen Teilchen führt hierbei zu einer Doppler-Verschiebung welche die FIDA-Emission von anderen Beiträgen im Spektrum trennt.

Das bei ASDEX Upgrade installierte passive FIDA-System besteht aus zwei neuen Spektrometern mit sehr hohem Lichtdurchsatz und Sichtlinien, welche für den Plasmarand optimiert sind. Die Spektrometer ermöglichen FIDA-Messungen mit beispielloser zeitlicher Auflösung und ermöglichen gleichzeitig die Messung der Emission von thermischen Hintergrund-Neutralen. Diese sog. thermische Emission enthält wichtige Informationen zur Neutral-Teilchen Dichte, welche für die quantitative Interpretation passiver FIDA-Messungen entscheidend ist. Daher konnte eine neue Methode entwickelt werden, mit der theoretische Profile von Neutralen verifiziert und, falls nötig, skaliert werden können.

Plasma-Entladungen wurden an ASDEX Upgrade durchgeführt in denen mittels Neutral-Teilchen Injektion (NBI) eine hohe Dichte von schnellen Ionen außerhalb des Plasma Zentrums erzeugt wurden. Hierbei konnten starke passive FIDA Signale beobachtet werden welche einen klaren Effekt der periodisch auftretenden ELMs aufzeigen. Während im äusseren Bereich des Plasmas eine klare Reduktion der FIDA Emission beobachtet wird, zeigen Messungen innerhalb der letzten geschlossenen Fluss fläche erhöhte Signale kurz nach dem Auftreten von ELMs. Dies konnte durch den verstärkten Einfluss von Hintergrund Neutralen erklärt werden und ist guter Übereinstimmung mit sog. Neutralteilchen

Messungen (NPA). Der Rückgang der FIDA Emission im äusseren Bereich, aber auch im inneren Bereich nach einer erster Überhöhung, kann auf die Umverteilung der schnellen Ionen zurückgeführt werden.

Detailliertes sensitivitätsstudien bezüglich der Änderungen der Plasmaposition während ELMs zeigen, dass das Ergebnis starker ELM-induzierter Verluste robust ist. Hierbei ist auch zu beachten, dass kleine ELMs beobachtet werden, welche die Dichte der Hintergrund Neutralen und die Plasmaposition nur geringfügig ändern und dennoch einen signifikanten Rückgang der FIDA Emission verursachen.

Die systematische Modifikation der theoretischen Verteilungsfunktion schneller Ionen, welche zur Vorhersage synthetischer FIDA-Signale verwendet wird, zeigt die beste Übereinstimmung mit den Daten, wenn etwa 60 % der schnellen Ionen durch ELMs ausserhalb der letzten geschlossenen Flussfläche verloren gehen. Zudem kann ein Rückgang der schnellen Ionen-Dichte von etwa 20 % in einem Bereich bis zu 4 cm innerhalb der letzten geschlossenen Flussfläche ermittelt werden. Dieses Ergebnis stimmt gut mit den jüngsten Modellierungsergebnissen von ELMs mit Hilfe des nichtlineares MHD Codes JOREK überein und zeigt, dass weniger als 0.3 % aller schnellen Ionen durch ELMs verloren gehen.

Abstract

Good confinement of fast supra-thermal ions is important in fusion experiments because the fast particles should heat the background plasma and contribute to the current drive. In addition, badly confined fast ions would not only affect the power output of a possible power plant, but may also damage wall components. In particular, good confinement of fast-ions located in the outer region of the plasma is important, since already weak perturbations might be sufficient to redistribute the fast ions onto so-called open field lines. A known instability at the edge of magnetically confined fusion plasmas is the so-called Edge Localised Mode (ELM) which is well known to periodically redistribute heat, particles and momentum. However, it is still not completely clear how strong the influence of ELMs are on the fast particles.

To study fast ions at the plasma edge passive fast-ion deuterium-alpha (FIDA) measurements were developed and applied to the ASDEX Upgrade Tokamak. The FIDA technique is based on the spectroscopic investigation of the Balmer-alpha emission line, which is emitted by fast ions after charge exchange reactions with background neutrals. The high speed of the energetic particles leads to a Doppler shift which separates the FIDA emission from other contributions to the spectrum.

The passive FIDA system installed at ASDEX Upgrade consists of two new spectrometers with very high light throughput and lines of sight, which are optimised for the plasma edge. The spectrometers enable FIDA measurements with unprecedented temporal resolution and simultaneously enable the measurement of the emission of thermal background neutrals. The thermal emission contains important information about the neutral particle density, which is crucial for the quantitative interpretation of passive FIDA measurements. Therefore, a new method has been developed, with which the theoretical profiles of neutrals can be verified and, if necessary, scaled.

Plasma discharges were carried out on ASDEX Upgrade in which a high density of fast ions outside the plasma centre was generated by means of off-axis neutral particle injection (NBI). Strong passive FIDA signals were observed which show a clear effect of the periodically occurring ELMs. While a clear reduction in the FIDA emission is observed in the outer area of the plasma, measurements within the last closed flux surface show increased signals shortly after the appearance of ELMs. This can be explained by the increased density of background neutrals and is in good agreement with neutral particle measurements (NPA). The decrease in FIDA emissions in the outer area, but also in the inner area after the initial increase, can be attributed to the redistribution of the fast ions.

Detailed sensitivity studies regarding changes in plasma position during ELMs show that the result of strong ELM-induced losses is robust. It should also be noted here that small ELMs are observed, which only slightly change the density of the background neutrals and the plasma position and nevertheless cause a significant decrease in FIDA emission.

The systematic modification of the theoretical distribution function of fast ions, which is used to predict synthetic FIDA signals, shows the best agreement with the data when about 60 % of the fast ions are lost by ELMs outside the last closed flux surface. In addition, a decrease in the fast-ion density of about 20 % in a range up to 4 cm within the last closed flux surface can be inferred. This result agrees well with the latest modelling results of ELMs using the non-linear MHD code JOREK and shows that less than 0.3 % of all fast ions are lost by ELMs.

Contents

Chapter 1

Introduction

A reduction in the emission of greenhouse gases is of major importance for the mitigation of global warming. Energy production from sustainable sources is therefore necessary. However, the intermittent supply of energy from technologies such as wind and solar power requires practical energy storage solutions not yet available. Therefore, large scale baseline power plants are required to ensure a continuous supply of energy. Here, power plants based on thermonuclear fusion might be attractive. In contrast to fission power plants, those nuclear power plants would not produce long-lasting radioactive waste, be inherently safe from runaway chain reactions and have an abundant supply of fuel.

1.1 Thermonuclear fusion

Nuclear fusion is the process that powers stars by fusing light elements into heavier elements. The sun for example fuses hydrogen into helium in a process known as the proton-proton chain, as illustrated in figure 1.1. The resulting rest mass difference Δm between the fusion reactants and products leads to a release of energy, according to the mass-energy equivalence principle $E = mc^2$. While fusion has a positive energy gain for reactions that produce elements lighter than iron, energy is required to obtain elements with higher charge numbers.

For fusion to occur the positive nuclei need to overcome the Coulomb barrier so they can be joined by the nuclear force. This process can readily be achieved in laboratories using particle accelerators. However, this does not produce an excess of energy as the fusion reaction has a much lower cross-section compared to Coulomb collisions. Therefore the output power is less than the input power ($P_{\mathrm{out}} < P_{\mathrm{in}}$) or alternatively the ratio $Q = P_{\mathrm{out}}/P_{\mathrm{in}}$ is significantly lower than 1. Instead, a confined thermal ensemble of particles is preferable, such that those particles which undergo elastic Coulomb collisions are not immediately lost. A figure of merit describing the conditions required for achieving Q =1, in other words break-even, is given in terms of the density (n), temperature (T) and energy confinement time (τ_{E}) of the ensemble, known as the fusion triple product ($nT\tau_{\mathrm{E}}$), first proposed by Lawson [4].

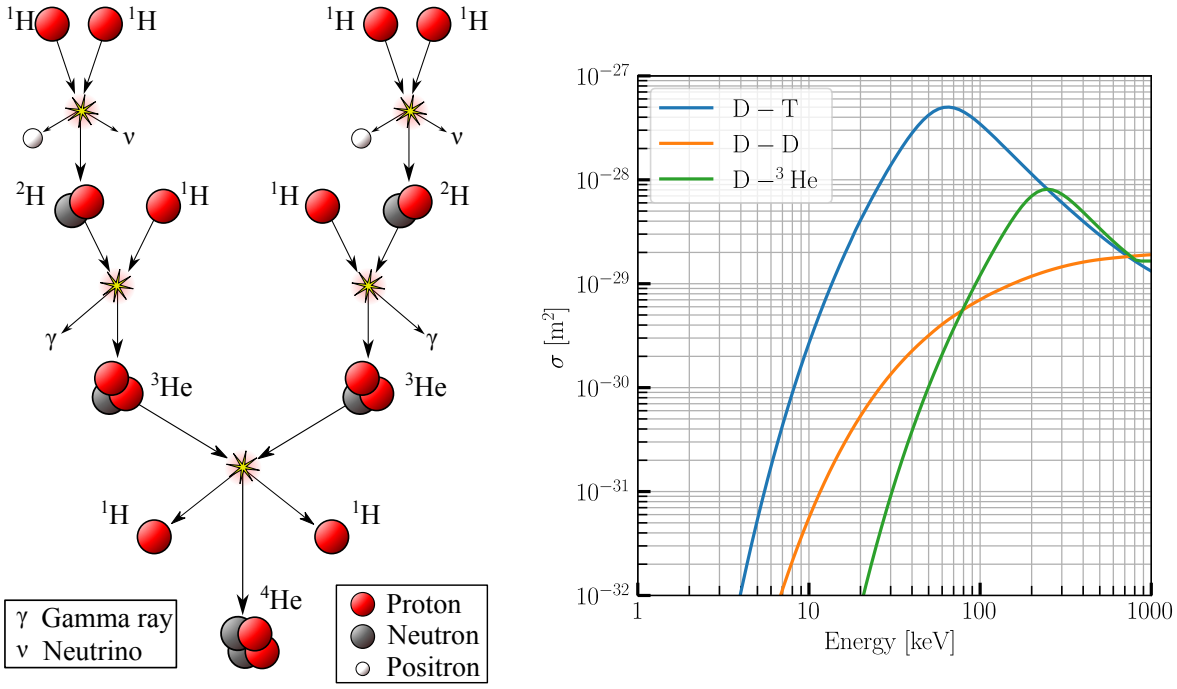

Figure 1.1: Left: The main branch of the proton-proton chain the mechanism by which hydrogen ions are fused into helium in the sun [1]. Right: Cross-sections σ for the fusion reactions between: deuterium and tritium, deuterium and helium and two deuterium ions as a function of the centre of mass collision energy [2] (with data from [3]).

Making use of the proton-proton chain on earth is not feasible as the cross-section for fusing hydrogen with hydrogen is extremely small [5]. The sun can compensate for the small cross-section by very large densities and gravitational confinement. Instead, on earth the fusion of deuterium D and tritium T is one of the most promising reactions:

$$D + T \rightarrow \alpha + n + 17.6\,\mathrm{MeV}\,, \tag{1.1}$$

here, the reaction products α and n are a helium particle and a neutron, respectively. The D-T fusion reaction produces 3.5 MeV per nucleon which is significantly larger than the energy gain per nucleon released by fission reactions (∼0.9 MeV per nucleon). In addition, it has a large cross-section σ which peaks at a moderate collision energy of 64 keV (see figure 1.1). Moreover, the Lawson criterion for D-T fusion has a low minimum $nT\tau_\mathrm{E}$ of $3 \times 10^{21}\,\mathrm{keV\,s^{-1}\,m^{-3}}$ at a temperature of around 160 million K or 14 keV (since 1 eV ≈ 11 605 K). At these temperatures particles form a plasma, a highly ionised state of matter.

Due to the required temperatures, it becomes challenging to confine the high temperature plasmas, as conventional material confinement is not feasible. Various methods have been devised including laser inertial confinement and magnetic confinement. Inertial confinement works by firing an intense, short burst of laser beams onto a small D-T pellet,

heating and compressing the pellet sufficiently for fusion reactions to occur. Magnetic confinement on the other hand takes advantage of the Lorentz force $\vec{F} = q(\vec{E} + \vec{v} \times \vec{B})$, felt by particles with charge q and moving with a velocity $\vec{v}$ in the presence of an electric $\vec{E}$ and magnetic $\vec{B}$ field, to confine the charged particles along magnetic field lines. To generate a magnetic field that effectively confines plasmas, several approaches exist of which tokamaks are one of the most promising concepts.

1.2 The tokamak concept

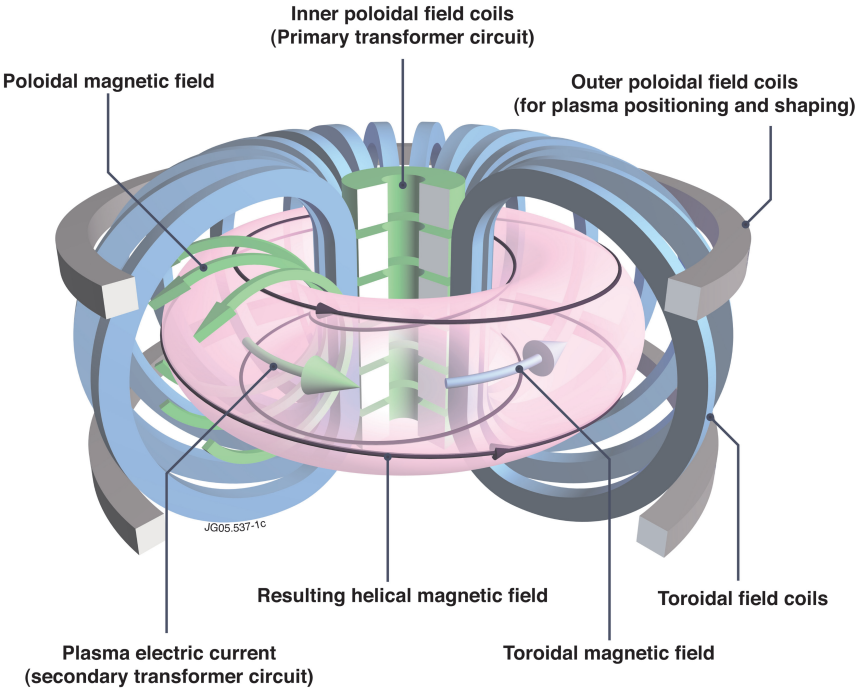

Figure 1.2: Illustration of the tokamak concept depicting the magnetic field coil configuration and magnetic field structure [6].

Tokamaks confine a plasma with a helically twisted toroidal magnetic field, as illustrated in figure 1.2. A strong toroidal field is generated with a set of toroidal field coils and an additional poloidal field component is generated by inducing a current in the highly conductive plasma. The poloidal field primarily acts to confine the plasma while the toroidal component mainly provides stability to the plasma. The plasma current is generated by varying current through a central transformer coil which induces a loop voltage in the plasma that acts as the secondary transformer circuit. Typically the poloidal magnetic field component B_θ generated by the plasma current is one order of magnitude smaller than the toroidal field component B_t.

The helically twisted field lines produce closed nested magnetic flux surfaces. The helicity of the magnetic field for a given flux surface is quantified by the safety factor q

given by:

$$q = \frac{d\Phi}{d\Psi} = \frac{m}{n}\,, \tag{1.2}$$

where m describes the number of toroidal turns needed for n poloidal turns. Φ and Ψ are the toroidal and poloidal magnetic flux defined by:

$$\Phi = \int_{A_{\mathrm{tor}}} \vec{B} \cdot d\vec{A}\,, \quad \Psi = \int_{A_{\mathrm{pol}}} \vec{B} \cdot d\vec{A}\,, \tag{1.3}$$

where A_{tor} and A_{pol} are the surfaces that span the poloidal plane and equatorial midplane, respectively as illustrated in figure 1.3. Note that the definition is valid for an arbitrary choice of the toroidal angle ϕ in the coordinate system (R,z,ϕ), such that Φ and Ψ are uniquely described by the coordinates R and z.

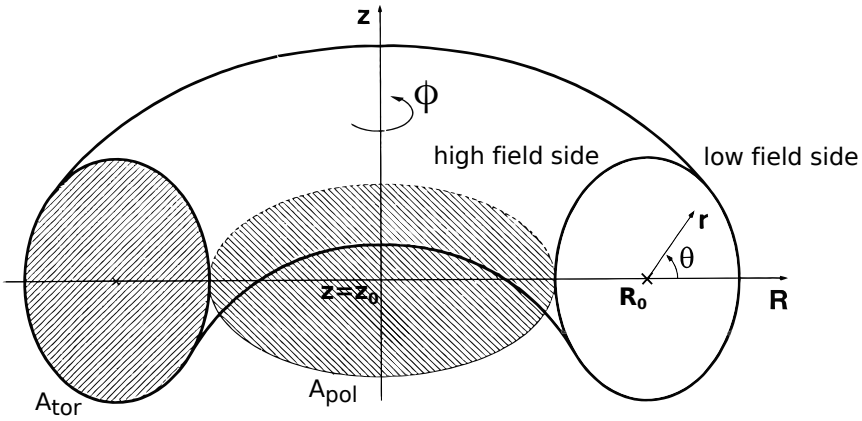

Figure 1.3: Illustration of the A_{tor} and A_{pol} surfaces. Additionally the tokamak coordinate system used in this thesis is indicated. The coordinates define the radius R, height z and toroidal angle ϕ. Additionally the minor radius r and poloidal angle θ are indicated. The midplane is located at $z = 0$ and the magnetic axis at (R_0,z_0) as marked by the cross. Taken from [7].

Magnetic equilibrium

A plasma in the presence of a magnetic field $\vec{B}$ reaches an equilibrium state when the force due to the plasma pressure gradient $\vec{\nabla} p$ is balanced by the magnetic force such that:

$$\vec{\nabla} p = \vec{j} \times \vec{B}\,, \tag{1.4}$$

where $\vec{j}$ refers to the current density. Equation 1.4 means that both $\vec{B}$ and $\vec{j}$ are perpendicular to $\vec{\nabla} p$, such that $\vec{B} \cdot \vec{\nabla} p = 0$. Physically this implies that the plasma pressure is constant along a magnetic field line, or in the tokamak context constant on a flux surface.

The magnetic flux surfaces provide a useful coordinate to map quantities such as the plasma pressure $P(\Psi)$ and current $I_{\mathrm{p}}(\Psi)$. A more intuitive form relating the magnetic flux to a radial length from the plasma centre is given by:

$$\rho_{\mathrm{pol}} = \sqrt{\frac{\Psi - \Psi_{\mathrm{axis}}}{\Psi_1 - \Psi_{\mathrm{axis}}}}, \quad \rho_{\mathrm{tor}} = \sqrt{\frac{\Phi - \Phi_{\mathrm{axis}}}{\Phi_1 - \Phi_{\mathrm{axis}}}}\,, \tag{1.5}$$

where the subscript 1 indicates the flux up to the last closed flux surface (LCFS), such that $\rho = 0$ at the magnetic axis and $\rho = 1$ at the LCFS. Both the toroidal and poloidal flux can be used for this purpose. Note here that the toroidal flux, i.e. the flux of the toroidal magnetic field through a given poloidal flux surface area, is only defined inside the LCFS, provided there are no points where the poloidal field is zero known as X-points. In contrast, the poloidal flux is also defined outside the LCFS.

Plasma heating and fast ions

The plasma current in a tokamak leads to resistive heating of the plasma. However this ohmic heating decreases at increasing temperature as the plasma resistivity is proportional to $T^{-3/2}$. Thus supplementary heating is required to achieve high plasma temperatures.

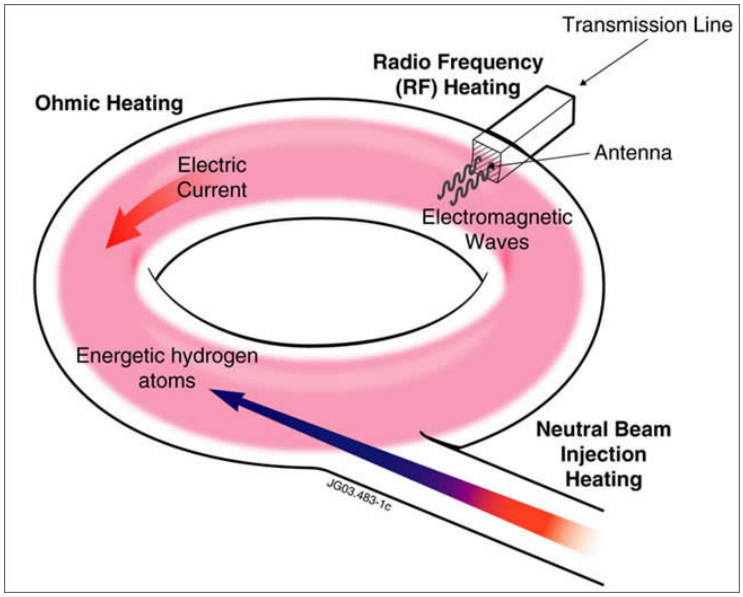

Figure 1.4: Illustration of plasma heating mechanisms used in magnetic confinement fusion devices. Apart from the intrinsic ohmic heating, wave heating and neutral beam injection heating are common methods used. Taken from [8].

Figure 1.4 illustrates two common external heating methods used, namely wave heating and neutral beam injection heating (NBI). Wave heating injects electromagnetic waves with frequencies matching the resonant frequencies of the gyrating electrons (using microwaves) and ions (using radio waves). NBI on the other hand injects energetic neutral particles with energy (on the order of 50 to 100 keV in present day devices) much larger than the thermal plasma ions, which are unaffected by the magnetic field. The neutrals entering the plasma are ionised by charge exchange reactions and collisions with plasma particles and become confined by the magnetic fields as fast ions. These energetic particles heat the bulk plasma by Coulomb collisions during their subsequent slowing down and finally become thermalised. Note, radio frequency heating also produces fast ions that are slowed by collisions. In addition, the alpha particles, produced by the fusion reaction are born with about 3.5 MeV of energy. In burning plasmas, these energetic alphas are supposed to

provide the majority of the plasma heating.

However, several instabilities and mechanisms exist that might degrade the fast-ion confinement. This would reduce the heating performance of the devices and provides even the risk of damaging plasma facing components by localised fast-particle losses. It is for instance calculated that the alpha particle loss tolerance in the next generation experimental fusion experiment "ITER" – currently under construction in Cadarache, France – will be as low as 5 % [9].

The H-mode and ELMs

One prominent type of plasma instabilities are edge localised modes (ELMs) which are linked to the so-called high confinement mode (H-mode). The latter was discovered in 1981 and exhibits improved plasma confinement above a critical input heating power [10]. The regime is characterised by a steep pressure gradient at the plasma edge as demonstrated in figure 1.5a. An edge transport barrier (ETB) leads to the formation of a pedestal, increasing the plasma pressure around a factor 2 compared to an L-mode (low confinement) plasma.

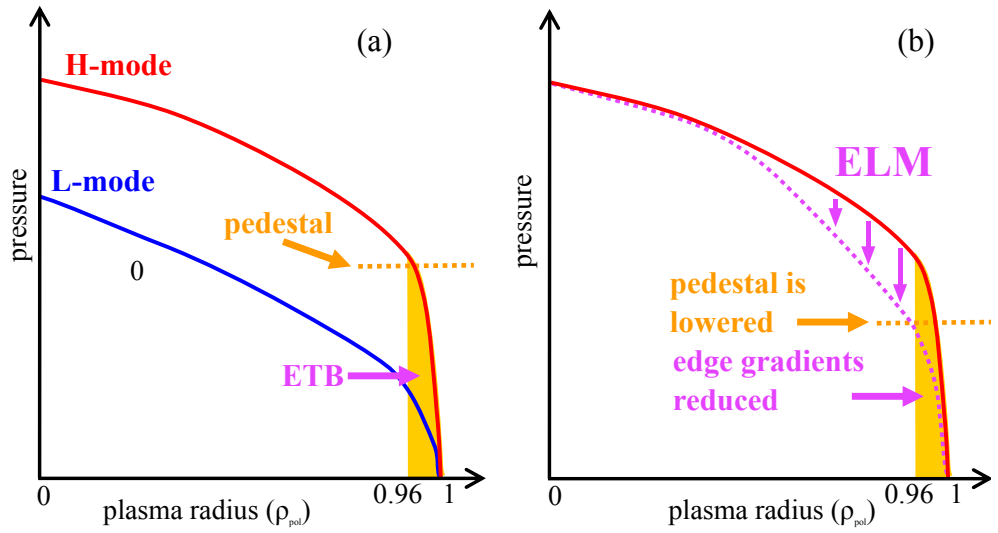

Figure 1.5: (a) Illustration of an H-mode plasma pressure profile compared to that of an L-mode plasma. The H-mode pressure profile is characterised by a steep gradient and pedestal at the plasma edge due to an edge transport barrier (ETB). (b) Illustration indicating the collapse of the H-mode pressure pedestal as a result of an edge localised mode (ELM). Adapted from [11].

The improved confinement associated with the H-mode regime has allowed tokamaks to reach the largest triple product [12], and is the foreseen operating regime for future reactors. However, H-modes are additionally characterised by a type of instability known as the ELM. ELMs result in a sudden expulsion of thermal plasma content from the edge, leading to a collapse of the pressure pedestal, demonstrated in figure 1.5b.

ELMs are especially of interest for this thesis as they have been shown to cause fast-ion losses [13]. However, the absolute magnitude of the losses is yet to be addressed. In order to study their impact the experimental distribution of fast ions in six dimensional phase space

(with three spatial and three velocity coordinates) needs to be obtained. Several fast-ion diagnostics exist that directly measure or infer the fast-ion distribution, including fast-ion loss detectors, collective Thomson scattering, neutron emission spectroscopy, neutral particle analysers and active fast-ion D-alpha spectroscopy (FIDA) [14]. However, most fast-ion diagnostics have limited sensitivity to the confined fast-ion content in the edge region.

1.3 This thesis

In the framework of this thesis, a new edge optimised passive FIDA diagnostic system has been installed at the ASDEX Upgrade tokamak. A pair of two new prototype spectrometers has been assembled and connected to edge lines of sight. The spectrometers have two advantages over previous designs which are especially relevant for edge measurements. Firstly the spectrometers are able to measure the full Balmer alpha spectrum, such that the intense unshifted D-alpha emission and the faint red and blue shifted FIDA emission can be measured simultaneously. This is particularly useful as the D-alpha emission contains information on the background neutral density which contributes a significant passive component to the measured signal. Secondly through the use of a burst mode feature of the attached CCD-cameras, the spectrometers can be configured to measure the full Balmer spectrum at exposure times down to 200 µs. This is a significant increase in temporal resolution compared to conventional systems operated typically with 5 ms long exposure times, and allows to study transient phenomena not previously resolvable. Using the new system as well as a method developed to analyse passive emission, a study of the redistribution of fast ions by ELMs has been carried out and is presented here.

The structure of the thesis is as follows: chapter 2 provides an introduction to several concepts relevant to this work, including the generation and orbits of fast ions in tokamaks. Furthermore the slowing down and transport of fast ions are presented along with the modelling tools used to calculate the fast-ion and background neutral distribution. Chapter 3 presents a detailed description of the ASDEX Upgrade tokamak and the diagnostic systems used during this work. Chapter 4 presents the main analyses and forward modelling tool used during this work, namely FIDASIM. In particular the inclusion of passive FIDA modelling developed during this work is presented. A detailed description of the new edge FIDA system installed during this work is provided in chapter 5. The methodology developed for the analyses of passive FIDA emission at ASDEX Upgrade is presented in chapter 6. Chapter 7 presents a study of the redistribution of fast ions by edge localised modes using measurements from the new edge FIDA system and the analyses of passive FIDA emission. Finally a summary and outlook is presented in chapter 8.

Chapter 2

Theoretical Background

Fast ions refer to plasma ions with energies much greater than the thermal plasma ions and with a velocity distribution that often deviates significantly from a Maxwell distribution. Fast ions are present in fusion devices due to the fusion process itself generating fast alpha particles as well as through the application of external plasma heating and current drive.

Good confinement of fast ions is important to ensure efficient heating and current drive. In particular fusion born alpha particles must be confined long enough such that they are thermalised before being lost. Excessive and localised losses must be avoided in future fusion devices, since these could lead to heat loads on plasma facing components that produce an uncontrollable impurity influx, contaminating the plasma, and possibly damage the components [15]. It is therefore of major importance to understand possible fast-ion transport mechanisms and find ways to control them.

This chapter presents an overview of fast ion topics relevant to this thesis. Firstly the sources of fast ion will be discussed in section 2.1 followed by their orbit topologies in section 2.2. The slowing down of fast ions through Coulomb collisions and the resulting fast-ion distribution function will be covered in section 2.3. Then, section 2.4 will discuss neoclassical fast-ion transport in tokamaks along with transport induced by magnetohydrodynamic modes. Lastly the main fast-ion modelling codes used for this work will be introduced in section 2.6.

2.1 Fast ion sources

Fast ions are generated during fusion reactions and by auxiliary heating systems, specifically neutral beam injection (NBI) and radio wave heating such as ion cyclotron resonance heating (ICRH).

In future fusion devices, the fusion reaction between deuterium and tritium, described by equation 2.1, will generate a 3.56 MeV alpha ($^4He^{2+}$) particle which needs to be confined by the magnetic field structure and transfer its energy to the background plasma via Coulomb collisions. Unlike fast ions generated by auxiliary heating systems, fusion born alphas will have an isotropic velocity distribution. The bulk of the alpha particles will be

generated in the plasma core where the temperature is the highest. For a burning plasma, that is to say a self heating fusion plasma, energetic alphas are expected to be the main plasma heating mechanism.

$$D + T \rightarrow 3.56\,\mathrm{MeV}\,\alpha + 14.03\,\mathrm{MeV}\,n \tag{2.1}$$

ICRH heating on the other hand generates fast ions by accelerating ions through the use of radio waves in the ion cyclotron frequency range, where the resonance frequency f is given by [16]:

$$f = \frac{Z_\mathrm{i} e B}{2\pi m} \approx 15 \frac{Z_\mathrm{i} B}{A_\mathrm{i}}\,\mathrm{MHz}\,, \tag{2.2}$$

where Z_i and A_i is the ion charge and atomic numbers and B the magnetic field strength. The externally injected waves exert a force on the ions via the electric field component of the wave, that cause ions to accelerate or decelerate, depending on their instantaneous velocity vectors as they gyrate along the magnetic field lines. Ions gyrating at the frequency of the incident waves are resonantly accelerated, depending on their phase, and obtain an increase in energy perpendicular to the magnetic field that leads to a highly an-isotropic distribution of velocity vectors. This yields a diffusion in velocity space towards higher energies and impacts mainly the perpendicular motion of fast ions. The resonance condition is fulfilled within a narrow radial location, because of the $1/R$ radial dependence of the tokamak magnetic field resulting in the existence of a resonance layer. For ICRH at ASDEX Upgrade, minority heating is applied which typically means that hydrogen ions are heated which are a minority species in a deuterium plasma. Direct heating of the main species is not possible since the waves are evanescent at the corresponding wavelength such that their perpendicular electric field component vanishes at the resonance layer.

NBI heating produces fast ions by injecting a beam of high energy neutral particles into the plasma which are not deflected by the magnetic fields. The beam neutrals are ionised by charge exchange reactions, which is the dominant ionisation mechanism for beam neutrals with energies below 50 keV/u, and collisions with the background plasma such that fast ions are born. The corresponding fast-ion energies and velocity vectors are determined by the beam acceleration voltage and injection geometry. Figure 2.1 shows a schematic drawing of an NBI source. First, ions are generated in the ion-source that is typically based on an RF discharge or by an emitting filament. The ions are then extracted and accelerated to high energies via a high potential. Before being injected into fusion plasmas, the highly energetic ions are neutralised by the interaction with a cloud of neutrals. Beam ions that have not become neutralised are directed to a beam dump via a strong magnetic field after this stage.

Apart from atomic ions molecular ions are also generally present in the ion source such as D_2^+ and D_3^+. The energy gained per deuterium atom of the accelerated molecules is a half and a third of the full beam energy, and may constitute significant fractions of the beam particles. As an example the beam species ratio of the NBI heating system at ASDEX Upgrade is approximately 0.4:0.4:0.2 (D:D_2:D_3).

In most fusion devices, positive ion sources are used since these are relatively easy

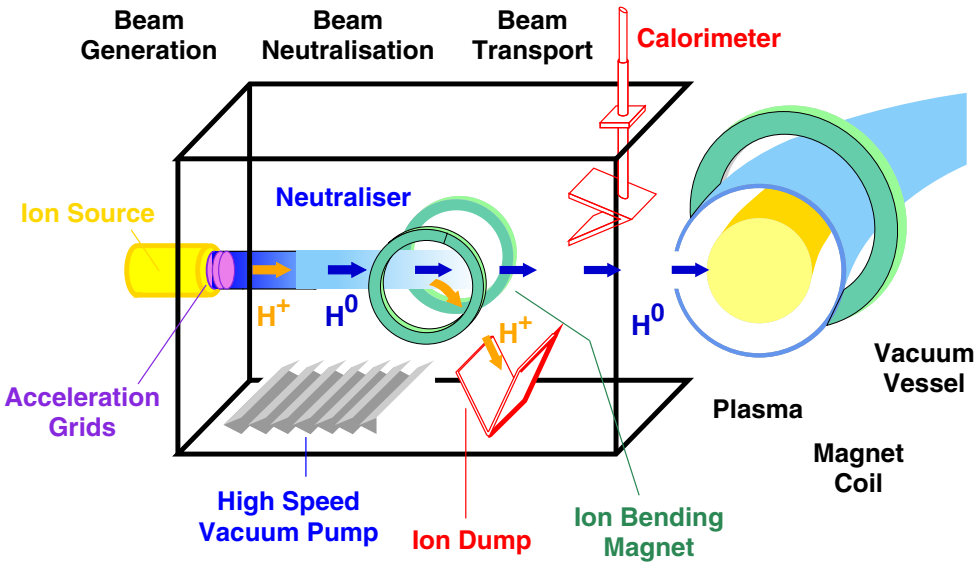

Figure 2.1: Schematic illustrating the fundamental elements of a neutral beam injection system [17].

to generate. With increasing beam energy however, neutralisation efficiency goes down dramatically such that negative ion sources are required. In ITER, for example a 1 MeV NBI will be used which is based on a negative ion source. Hereby, the neutralisation efficiency is high (up to 60% [18]).

2.2 Ion orbits

Charged particles, such as fast ions that move in the presence of a magnetic field $\vec{B}$ experience a Lorenz force ($\vec{F_{\mathrm{LF}}} = \vec{v} \times \vec{B}$). This force will result in a gyro motion around the magnetic field lines. The gyration radius, known as the Larmor radius ρ_{L}, is determined by the velocity of the particle perpendicular to the magnetic field $v_{\perp}$ such that:

$$\rho_{\mathrm{L}} = \frac{v_{\perp}}{\omega_{\mathrm{c}}}, \tag{2.3}$$

where ω_{c} is the angular gyration frequency called the cyclotron frequency defined as:

$$\omega_{\mathrm{c}} = \frac{qB}{m}, \tag{2.4}$$

where q and m are the charge and mass of the particle. The point around which the gyro motion is centred is referred to as the guiding centre. When the particle is subjected to an additional force $\vec{F}$, from an electric field for example, with a component perpendicular to $\vec{B}$ its gyro motion is distorted leading to a drift of the guiding centre. This drift is

perpendicular to both $\vec{F}$ and $\vec{B}$ and is given by:

$$\vec{v_{\mathrm{D}}} = \frac{\vec{F} \times \vec{B}}{qB^2}. \tag{2.5}$$

The toroidally curved magnetic field lines of a tokamak give rise to two dominant forces acting on the gyrating fast-ions. One is due to the gradient of the magnetic field ∇B produced by the toroidal arrangement of the field coils. The gradient force is given by:

$$\vec{F_{\nabla \mathrm{B}}} = -\frac{1}{2} m v_{\perp}^2 \frac{\nabla B}{B}. \tag{2.6}$$

This force points away from the torus centre, due to the $1/R$ dependency of the tokamak magnetic field strength. Another force is the centrifugal force $\vec{F_c}$ felt by the particles as they follow the curvature of the magnetic field lines. The outward acting force is determined by the field curvature radius R_c from the torus centre and is given by:

$$\vec{F}_{\mathrm{c}} = \frac{m v_{\parallel}^2}{R_{\mathrm{c}}^2} \vec{R}_{\mathrm{c}}\,, \tag{2.7}$$

where $v_{\parallel}$ is the particle velocity parallel to the magnetic field.

In the vacuum field approximation, that is to say not considering any magnetic field generated by the plasma, the ratio of the curvature radius and the tokamak magnetic field can be shown to satisfy the following relation:

$$\frac{\vec{R}_{\mathrm{c}}}{R_{\mathrm{c}}^2} = -\frac{\nabla B}{B}. \tag{2.8}$$

These two forces point in the same direction and lead to a combined drift:

$$v_{\mathrm{D}} = v_{\mathrm{D},\nabla \mathrm{B}} + v_{\mathrm{D,c}} = -\frac{m(v_{\parallel} + \frac{1}{2} v_{\perp})}{q} \frac{\nabla B \times \vec{B}}{B^3}. \tag{2.9}$$

The dependency of v_{D} on the charge q leads to ions and electrons drifting in opposite directions. For a tokamak configuration where the toroidal magnetic field points in the clockwise direction as viewed from above, ions will experience a downward drift while electrons experience an upward drift. The separation of charge will produce an electric field resulting in an $\vec{E} \times \vec{B}$ drift radially outwards, according to equation 2.2. Tokamaks avoid this by having poloidally twisted magnetic field lines. Ions and electrons are free to follow the twisted magnetic field lines such that a vertical electric field does not develop.

The radial gradient of the magnetic field combined with poloidally twisted field lines causes a parallel magnetic field gradient $\nabla B_{\parallel}$ to exist, since a given field line will encounter the high-field side and low-field side of the device. This leads to another force, this time parallel to the field, acting on gyrating particles travelling along field lines. For a gradient much larger than ρ_{L}, the force is expressed by:

$$F_{\parallel} = -\mu \nabla B_{\parallel}\,, \tag{2.10}$$

where μ is known as the magnetic moment, and is defined as:

$$\mu = \frac{1}{2}\frac{mv_{\perp}^2}{B}. \tag{2.11}$$

μ is a conserved quantity when the magnetic field does not strongly vary on the scale of the gyro radius, and its temporal variation is much slower than the gyro period. μ is therefore called an adiabatic invariant. Under these conditions a particle with a non-zero magnetic moment will experience a force acting against the magnetic field gradient. Physically an ion moving against the magnetic field gradient from the low to the high field side of a tokamak will compensate the increase in magnetic field strength encountered with an increase in the particles perpendicular velocity to conserve its magnetic moment. The conservation of particle energy requires that the increase in perpendicular energy be compensated by a decrease in the particle's parallel velocity. It is often convenient to express the particle velocity components in terms of kinetic energy E and pitch, with pitch defined as:

$$\text{pitch} = \frac{\mathrm{v}_{\parallel}}{\mathrm{v}} = \cos(\alpha)\,, \tag{2.12}$$

where α is the angle between the velocity and the magnetic field. The pitch of a particle therefore lies between 1 and -1, where a positive pitch is defined to be in the direction of the plasma current (co-current) and negative pitch motion in the direction opposing the plasma current (counter-current). A high enough magnetic field strength can cause the particle motion parallel to the field to be reversed effectively reflecting the particle like a magnetic mirror.

The conservation of the magnetic moment can be understood from Noether's theorem to be a result of the symmetry in the particles gyro coordinate. When considering charged particle motion in a tokamak magnetic field through the lens of Lagrangian mechanics another conserved quantity is exposed from the toroidal ϕ symmetry of the magnetic field known as the toroidal canonical momentum which can be shown to be:

$$P_{\phi} = mR^2\dot{\phi} + q\Psi\,, \tag{2.13}$$

where Ψ denotes the poloidal magnetic flux. The conservation of toroidal canonical momentum ensures that particles drifting from their initial poloidal flux surface eventually return to the same surface during their orbit. P_{ϕ} is also an adiabatic invariant and is only conserved as long as the spatial and temporal changes of the magnetic field are larger than ρ_{L} and slower than the poloidal orbit time of a particle, respectively.

2.2.1 Orbit classifications

In a tokamak several orbit types result from the guiding-centre drift effects described above. They strongly depend on the particle's pitch and energy. The orbits are broadly classified as trapped, passing or stagnation orbits:

Trapped orbits

Trapped orbits result from the magnetic mirror created by the tokamak magnetic field

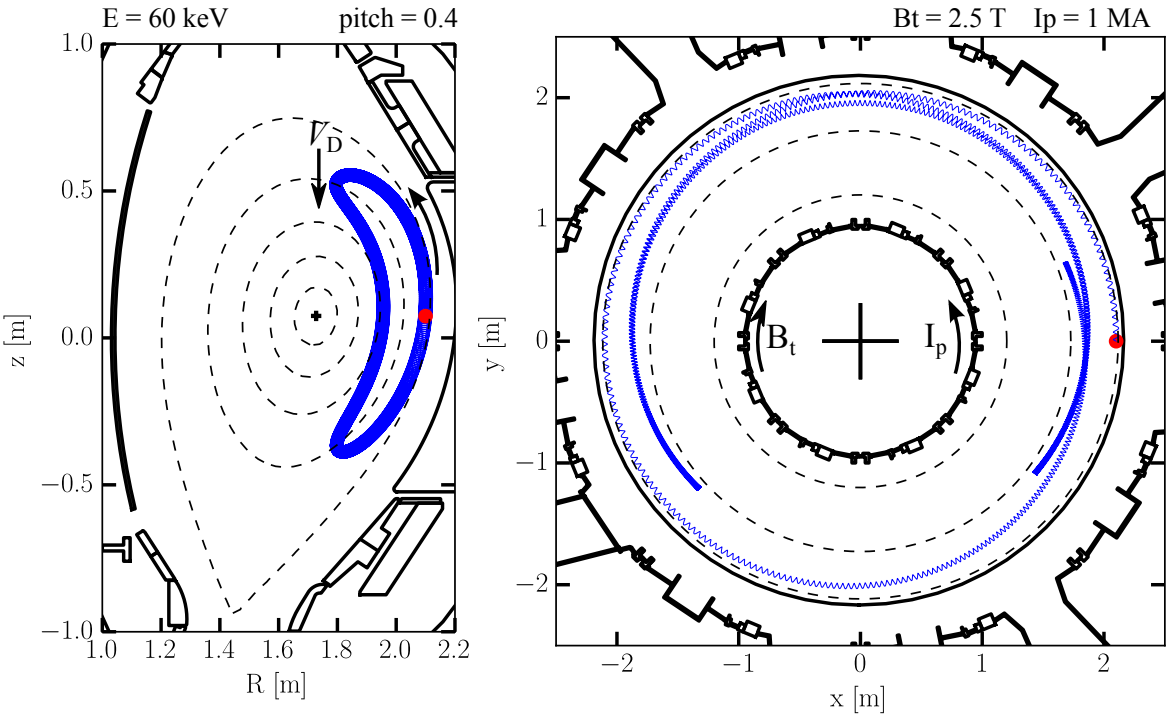

Figure 2.2: Poloidal and toroidal (top down) view of a trapped orbit.

gradient. Particles on the low field side with insufficient parallel velocity to overcome the magnetic field gradient are reflected when travelling to the high field side. Figure 2.2 illustrates the orbit of such particles which are trapped on the low field side. For figure 2.2 we considered a 60 keV fast particle with pitch = 0.4 in the standard magnetic field geometry of ASDEX Upgrade which has a magnetic field of 2.5 T (on axis) in the clockwise direction and a plasma current of 1 MA in the counterclockwise direction. The particle, launched at the position indicated with a red dot, moves upwards, explained by its motion along the helical magnetic field lines. In addition, it experiences a downward-drift away from its starting magnetic surface which becomes most visible at the particle's turning points where the movement along field lines is zero. The displacement with respect to the birth flux surface is however compensated over the course of the orbit such that the particle returns to the same flux surface that it started on. The closure of the orbit in the poloidal projection is enforced by the conservation of the angular canonical momentum. The projection of the orbit in the poloidal plane has the shape of a banana and is therefore also called a banana orbit. From the top view it can be seen that the reflection points move toroidally resulting in a slow toroidal precision. For deeply trapped particles the precession frequency ω_{pr} is approximately $E_{\mathrm{fi}}/q_{\mathrm{fi}}B_\theta R$, where q_{fi} is the fast-ion charge and B_θ is the poloidal magnetic field component [19].

For particles with pitch >0 (counter-clockwise in our example) on the low-field side, the initial drift is directed towards the magnetic axis, which ensures good confinement. In contrast, counter-I_{p} (pitch <0) particles on the low field side move downwards due

to both their motion along field lines and the curvature and grad-B drifts. The drift is therefore away from the magnetic axis which often results in unconfined orbits. Counter NBI injection therefore leads to a larger amount of so-called prompt losses which are fast-ion losses that occur immediately after turning on a fast-ion source and do not involve collisional or anomalous transport.

Passing Orbits

The orbits of particles that follow twisted magnetic field lines reasonably well are called

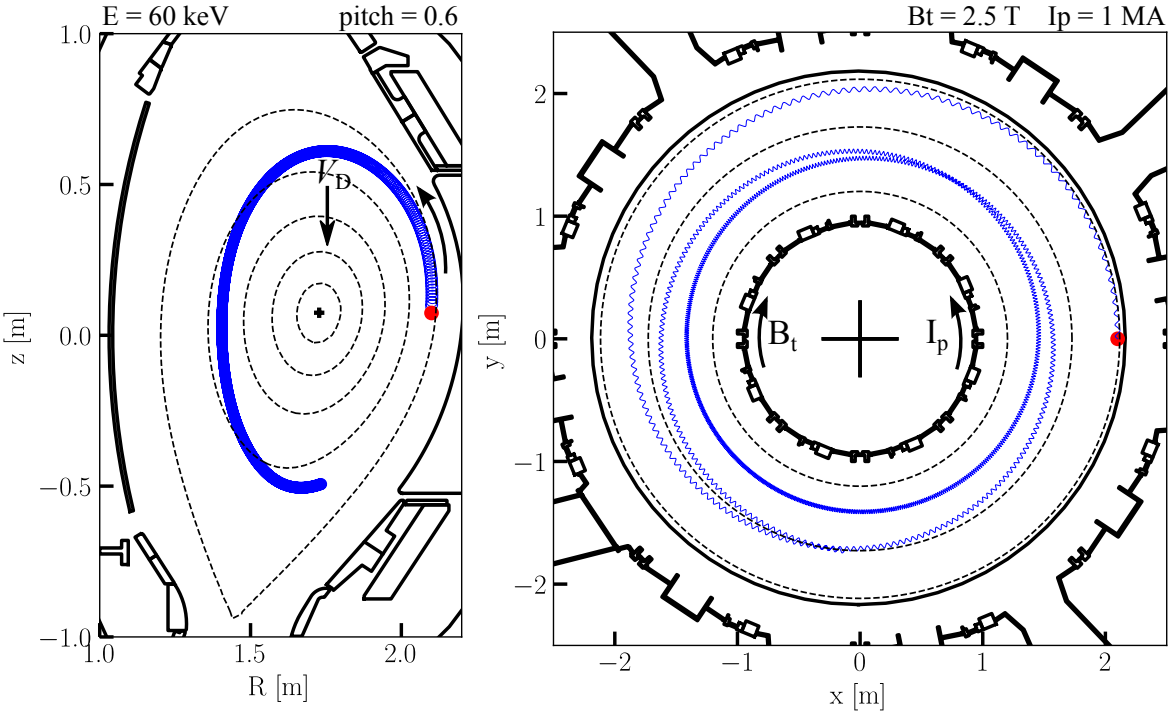

Figure 2.3: Poloidal and toroidal view of a passing orbit.

passing orbits. Passing particles have sufficient parallel velocity to avoid trapping and their orbits form a shifted flux surface shape when projected to the poloidal plane, as demonstrated in figure 2.3. As with banana particles, the passing particles lose parallel velocity leading to a reduction in the pitch angle as shown in figure 2.4. As the particles move to the high field side they drift away from their initial flux surface. The resulting orbit maps out a so-called drift surface. Depending on the direction of the plasma current the centre of the drift surface can be displaced either inwards or outwards with respect to the magnetic axis. Co-current streaming orbits will have their centre displaced outwards whereas counter-current streaming orbits will have their centre displaced inwards.

Stagnation Orbits

Stagnation orbits are a type of passing orbit that do not cross the magnetic axis. These orbits are followed by particles with high energy and large perpendicular velocity that leads to a strong drift closing the orbit before the particle is able to cross the magnetic axis.

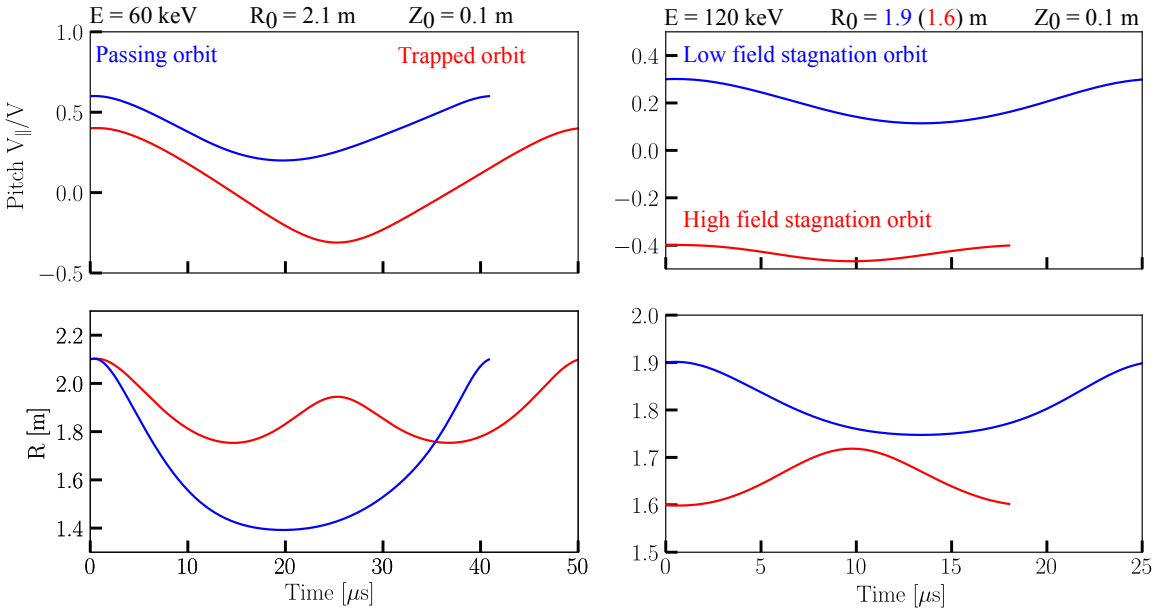

Figure 2.4: Pitch (top row) and radius R (bottom row) during trapped (fig. 2.2), passing (fig. 2.3) and stagnation (fig. 2.5) orbits.

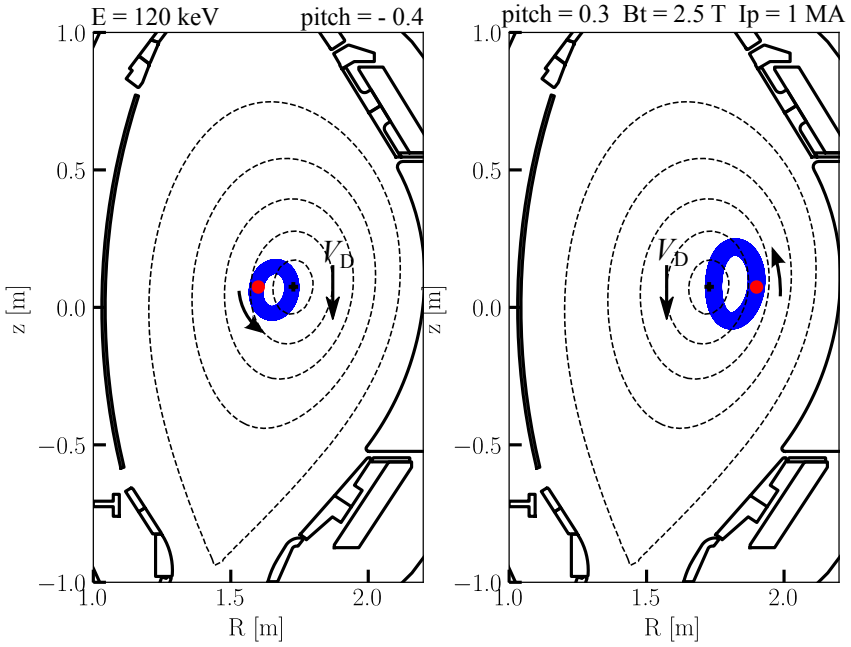

Figure 2.5: Poloidal view of high field (left) and low field (right) side stagnation orbits.

Stagnation orbits are possible on both the high field and low field sides of the axis and are close to the vertical position of the magnetic axis, as demonstrated in figure 2.5.

2.3 The fast-ion distribution function

In plasma physics, the large amount of particles makes it impractical to solve for the exact position and velocity for each ion or electron. It is instead useful to treat the particles as an ensemble described by a distribution function. The distribution of fast ions at a given time in the plasma can be described by a six dimensional function $F(\vec{x}, \vec{v})$, with three spatial and three velocity coordinates. The distribution function gives the number of fast ions in a unit of real space and velocity space, which in SI units is $[\mathrm{m}^{-3}(\frac{\mathrm{m}}{\mathrm{s}})^{-3}]$. Two symmetries of the tokamak magnetic field can be exploited to reduce the function to four dimensions. The first is the toroidal symmetry of the magnetic field. As the field strength does not depend on the toroidal angle ϕ, the spatial coordinates are sufficiently described by the radius R and height z of the fast particle, considering a cylindrical coordinate system (R, z, ϕ).

The second symmetry is along the fast-ion gyro-orbit axis. The velocity of the fast ion can be described by its parallel $v_\parallel$, and perpendicular $v_\perp$ projections with respect to the magnetic field line such that:

$$\vec{v} = v_\parallel \hat{e}_\parallel + v_\perp(\cos\gamma \hat{e}_{\perp,1} + \sin\gamma \hat{e}_{\perp,2})\,, \tag{2.14}$$

where γ is the gyro angle of the fast ion, $\hat{e}_\parallel$ is the unit vector parallel to $\vec{B}$ and $\hat{e}_{\perp,1,2}$ are mutually perpendicular unit vectors with respect to $\vec{B}$. The velocity can therefore be given by $(v_\parallel, v_\perp, \gamma)$ components, which describe a cylindrical coordinate system with $v_\parallel \in (-\infty, \infty)$, $v_\perp \in [0, \infty)$ and $\gamma \in [0, 2\pi]$. Here parallel velocity is parallel to B and positive in direction of the plasma current. As the magnetic field does not vary strongly over the length of the Larmor radius of fast ions, the gyro angle can be ignored. Alternatively one can consider that the fast-ion gyro period is typically much faster than the time scales on which the distribution function is expected to change. Therefore, integrating the distribution in time over several gyro periods would see γ averaged out. The velocity can, therefore, be sufficiently described by the parallel and perpendicular components along the magnetic field.

Instead of $v_\parallel$, $v_\perp$, it is convenient to express the velocity space in a more intuitive coordinate system namely energy E, and pitch. This is because the energy of particles can be directly compared to beam energies or particle temperatures. The relation between velocity and pitch has already been introduced in equation 2.12 and the kinetic energy is given by the well know relation:

$$E = \frac{1}{2}mv^2\,, \tag{2.15}$$

where $v = \sqrt{v_\parallel^2 + v_\perp^2}$.

2.3.1 Fast-ion energy transfer and slowing down

Fast ions transfer energy and momentum to thermal plasma particles through Coulomb collisions. The interaction time dt between colliding particles is inversely proportional to

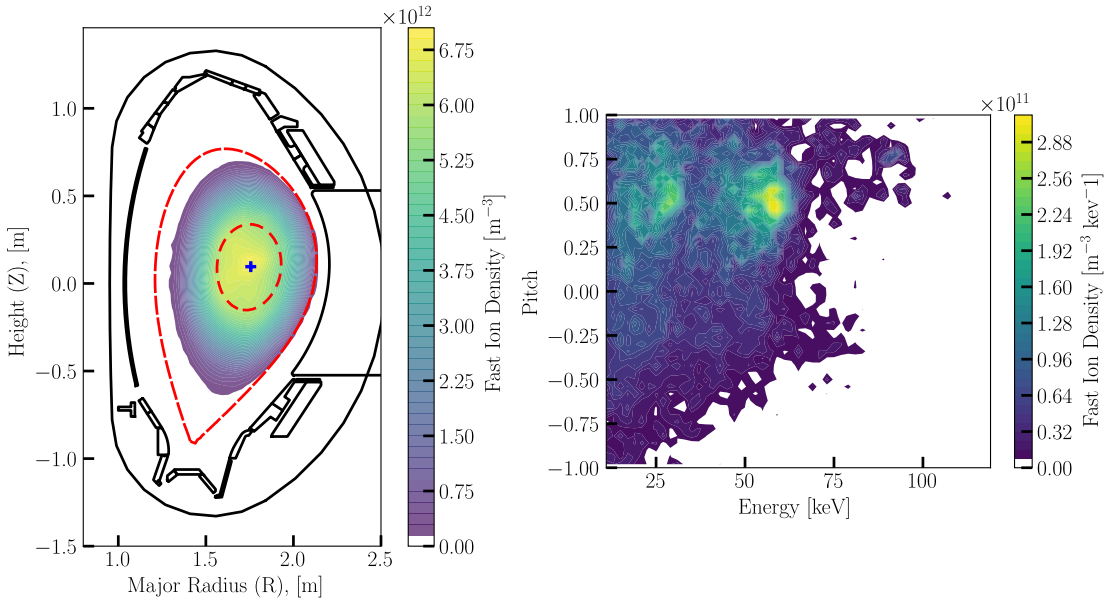

Figure 2.6: Theoretical calculated fast-ion density and velocity space distribution using the TRANSP code (see section 2.6). On the left the fast ion density distribution for a NBI heated ASDEX Upgrade discharge. On the right the velocity space distribution of fast ions at the magnetic axis.

the relative velocity of the colliding particles such that the effective momentum transfer $d\vec{p}$ through Coulomb collisions:

$$d\vec{p} = \vec{F}dt\,, \tag{2.16}$$

scales inversely with the collision velocity. This shows that collisions between species with very different velocities are ineffective.

As an example thermal ions are typically much slower than thermal electrons due to their much larger mass, despite often having similar temperatures. The thermal velocity v_{th} representing the most probable speed of a Maxwell distribution with temperature T is given by:

$$v_{\mathrm{th}} = \sqrt{\frac{2T}{m}}. \tag{2.17}$$

For deuterium ions and electrons in thermal equilibrium the mass difference results in $v_{\mathrm{th,e}} \approx \sqrt{2 \cdot 1836} \cdot v_{\mathrm{th,D}} \approx 61 \cdot v_{\mathrm{th,D}}$. Fast ions on the other hand have intermediate speeds that are faster than thermal ions but also much slower than thermal electrons. As an example a fast deuterium ion with an energy of 100 keV is still significantly slower than a 1 keV thermal electron, $v_{\mathrm{th,e}} \approx \sqrt{2}/\sqrt{100/1836} \cdot v_{\mathrm{f}} \approx 6 \cdot v_{\mathrm{f}}$. The thermal distribution however ensures that there are still some slower electrons present that have comparable speeds to fast ions.

This shows that highly energetic ions will primarily collide with thermal electrons rather than thermal ions such that fast ions mainly heat electrons. In contrast, low energetic fast-

ions in the presence of hot electrons will more likely collide with the background plasma ions, providing ion heating.

Based on these considerations, a critical fast-ion energy E_c can be defined above which mainly electrons are heated while ions are primarily heated below E_c. The critical energy, at which energy transfer between electron-ion and ion-ion collisions are equal, has been defined by [20] and reads:

$$E_\mathrm{c} = 14.8 A_\mathrm{f} T_\mathrm{e} \left(\frac{1}{n_\mathrm{e}} \sum_j \frac{n_\mathrm{j} Z_\mathrm{j}^2}{A_\mathrm{j}} \right)^{2/3} , \tag{2.18}$$

where A and Z indicate the mass and charge numbers of thermal ions species j and A_f indicates the mass number of a given fast ion species. T_e refers to the electron temperature. For fast deuterium ions in a pure deuterium plasma this equation reduces to:

$$E_\mathrm{c} = 18.6 T_\mathrm{e}. \tag{2.19}$$

The total energy transfer to electrons and ions during the entire slowing down time of a fast ion born with energy E_f is equal for $E = 2.41 E_\mathrm{c}$. For this reason 3.5 MeV alpha particles born in the core of ITER with a peak electron temperature of $T_\mathrm{e} = 20\,\mathrm{keV}$ will largely heat the thermal electrons.

Through frequent collisions, fast ions lose energy. The corresponding slowing down time of a fast ion with an initial energy E_f can be expressed in terms of the critical energy:

$$\tau_\mathrm{sd} = \frac{\tau_\mathrm{s}}{3} \ln \left(1 + \left(\frac{E_\mathrm{f}}{E_\mathrm{c}} \right)^{3/2} \right), \tag{2.20}$$

where τ_s is the so-called Spitzer time given by:

$$\tau_\mathrm{s} = 6.3 \times 10^{14} \frac{A_\mathrm{f} T_\mathrm{e}^{3/2}}{Z_\mathrm{f}^2 n_\mathrm{e} \ln \Lambda} , \tag{2.21}$$

where Λ is the ratio of the Debye length to the length at which particles are scattered by 90°. $\ln \Lambda$ is known as the Coulomb logarithm and can be given as [21]:

$$\ln \Lambda = 24 - \ln \left(\frac{\sqrt{n_\mathrm{e}\,[\mathrm{cm}^{-3}]}}{T_\mathrm{e}\,[\mathrm{eV}]} \right). \tag{2.22}$$

The Coulomb logarithm describes the factor by which small angle scattering dominates large angle scattering, and for typical fusion plasmas it can be approximated to 17.

As can be seen, the Spitzer time τ_s is proportional to $T_\mathrm{e}^{3/2}/n_\mathrm{e}$, with $\ln \Lambda$ only weakly dependent on T_e and n_e. The inverse proportionality of the slowing down time τ_sd on E_c and hence $\ln T_\mathrm{e}^{-3/2}$ reduces the T_e dependence of τ_sd but it still increases with T_e such that the slowing down time increases with increasing T_e. Fast ions born in hot thin plasmas, therefore, have longer slowing down times than in cold, dense plasmas as demonstrated in

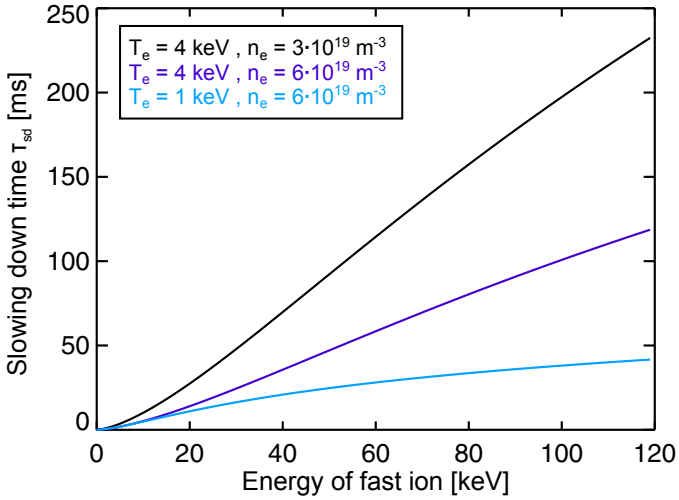

Figure 2.7: Fast-ion slowing down time τ_{sd} calculated using equation 2.20. τ_{sd} is plotted as a function of fast-ion energy for a high temperature and low density case (in black), a high temperature and high density case (in blue) and a low temperature and high density case (in cyan).

figure 2.7. A short slowing down time, as achieved in cold, dense plasmas, is beneficial from the point of heating efficiency, while for experiments which require high fast-ion densities, high temperature and low density plasma conditions are desirable.

The large mass difference between fast ions and electrons results in a small reduced mass involved during collisions. For that reason, momentum exchange is relatively small such that electrons impart relatively small energy and momentum changes to fast ions that do not significantly change their pitch. Ion collisions on the other hand result in more effective momentum exchanges due to their similar mass which can lead to changes in fast-ion pitch called pitch angle scattering. Pitch angle scattering is a diffusive process that acts to reduce gradients in pitch such that a peaked pitch distribution is flattened over time.

2.4 Fast-ion transport

2.4.1 Neoclassical transport

Fast-ion Coulomb collisions with thermal ions lead to a diffusive transport across the magnetic flux surfaces. In a homogeneous magnetic field this is referred to as classical transport. In the toroidal geometry of a tokamak classical transport is enhanced due to particle drifts which is described by so-called neoclassical transport. The magnitude of this transport is determined by the frequency ν_{fi} of Coulomb collisions and the orbit width of the fast ions. Neoclassical transport is divided into several regimes depending

on the collisionality. Due to their high velocity fast ions have long mean free paths and, therefore, their diffusion falls within what is called the banana regime. In this regime the toroidal effects do not considerably modify the transport of passing particles, however, trapped particle transport is affected. Here pitch angle scattering collisions cause the bouncing points of trapped particles to be displaced by ρ_{L}, the Larmor radius, so that the neoclassical diffusion coefficient is given by:

$$D_{\mathrm{neo}} = \frac{1}{2}\rho_{\mathrm{L}}^2 \nu_{\mathrm{fi}}\,, \tag{2.23}$$

with the collision frequency ν_{fi} given by:

$$\nu_{\mathrm{fi}} = \frac{2 \cdot 10^{-21} Z_{\mathrm{fi}}^2 Z_{\mathrm{eff}} n_{\mathrm{e}}}{A_{\mathrm{f}} E_{\mathrm{fi,[MeV]}}^3}\,[\mathrm{s}^{-1}]\,, \tag{2.24}$$

where Z_{eff} is the effective charge defined as:

$$Z_{\mathrm{eff}} = \sum_j \frac{n_{\mathrm{j}} Z_{\mathrm{j}}^2}{n_{\mathrm{e}}}. \tag{2.25}$$

The neoclassical diffusion coefficient therefore is $D_{\mathrm{neo}} \propto 1/\sqrt{E}$ so that the neoclassical diffusion of fast-ions is smaller than that of thermal ions. The fast-ion diffusion coefficient is typically on the order of $0.1\,\mathrm{m}^2/\mathrm{s}$, which is significantly less than the experimentally measured diffusion of thermal plasma on the order of $1\,\mathrm{m}^2/\mathrm{s}$ [22]. Experimental results from many devices show that fast-ion transport can be well described by neoclassical transport under magnetohydrodynamic (MHD) quiescent conditions.

However, several other transport mechanisms have been identified that can cause strong spatial redistribution and losses of confined fast ions. Additional transport often results from asymmetries present in the magnetic and electric fields. Asymmetries may arise from external field perturbations, oscillating MHD perturbations of the flux surfaces or turbulent fluctuations of the plasma density and potential as discussed in the following sections.

2.4.2 Externally induced field perturbations

Externally induced field perturbations are produced by error fields as well as external perturbation field coils. These sources cause asymmetries in the magnetic flux surfaces that may lead to enhanced particle transport. The intrinsic error field is partly caused by small errors in the shape and placement of the magnetic field coils, but this contribution is found to be rather small in ASDEX Upgrade [23]. In addition the discreet n number of toroidal field coils result in slightly corrugated or rippled magnetic field lines. At a given height and radius the magnetic field strength has a maximum B_{max} at toroidal angles closest to field coils and minimum values B_{min} midway between coils. The ripple amplitude δ defined as $\delta = (B_{\mathrm{max}} - B_{\mathrm{min}})/(B_{\mathrm{max}} + B_{\mathrm{min}})$, decreases with the number of toroidal field coils. ASDEX Upgrade has sixteen toroidal field coils which produce a ripple

amplitude less than about 1 % at the outboard midplane edge, where the field ripple is largest since the coils are spaced furthest apart [24, 25]. The calculated fast-ion losses due to the toroidal field ripple on ASDEX Upgrade are on the order of about 0.5 % [26], with the trapped particles most strongly affected.

Magnetic field perturbation coils in the form of saddle coils have been used in multiple devices to mitigate magnetohydrodynamic instabilities known as edge localised modes, discussed in section 2.4.4. The coils produce a radial field component that is small compared to the toroidal field strength, but breaks the axi-symmetry of the flux surfaces near the edge. This increases the heat and particle transport at the edge which reduces the pressure and gradients that drive the instability [27]. ASDEX Upgrade is equipped with two rows of eight in vessel saddle coils, situated above and below the outer midplane [28]. Experiments show that the use of field perturbation coils lead to the loss of fast ions, as measured by fast ion loss detectors on multiple devices [29]. The magnitude of losses is dependent on plasma parameters such as the collisionality and helicity of the magnetic field lines, as well as the perturbation spectrum. A numerical study with a Monte Carlo orbit following code, complemented by experimental measurements from fast-ion loss detectors at ASDEX Upgrade (described in chapter 3), suggests the existence of a resonant transport layer that is responsible for the ejection of fast ions [30].

2.4.3 Turbulence

Micro or small scale turbulence has been found to be the dominant transport process of thermal particles [31, 32]. Turbulent heat and momentum transport of the electrons in particular is orders of magnitude larger than neoclassical transport. Turbulent heat transport scales with the temperature gradient and leads to the occurrence of stiff temperature profiles [33]. The radial structure associated with turbulent fluctuations resemble fluid eddies. The turbulent fluctuations lead to radial transports across the flux surfaces due to the induced $\vec{\tilde{E}} \times \vec{B}$ drift.

Fast ions are found to be much less affected by turbulent fluctuations [19, 15]. It is thought that the large Larmor radii of fast ions lead to an averaging effect that largely cancels out the transport induced by the turbulent eddies, termed gyro averaging. Additionally, the large radial deviation of the orbits from the flux surfaces lead to a further decorrelation of the fast ions with the turbulent structures, known as drift averaging. However, if turbulent structures scale with machine dimensions, these averaging effects might be less effective so that fast ions may well be affected. Experiments at ASDEX Upgrade have found that micro-turbulence does not measurably enhance the neoclassical transport of fast ions on that device [34].

2.4.4 Magnetohydrodynamic modes

A particular concern for future fusion reactors is the effect that magnetohydrodynamic (MHD) modes may have on fast-ion confinement. MHD modes are plasma instabilities driven by the plasma pressure and current, or by fast-ions themselves. The modes deform

flux surfaces or provide an oscillation of magnetic field lines and can have a severe impact on plasma performance. Many MHD modes can mathematically be treated as spatio-temporal perturbations of the flux surfaces characterised by a poloidal m and toroidal n number, describing the periodicity of the structure.

Fast ions can resonantly interact with modes when their characteristic frequency ω_{fi}, such as their (slower) toroidal precession or (faster) poloidal transit/bounce frequency, is close to that of the mode frequency ω causing them to encounter the mode many times. Resonant fast ions may be redistributed radially by the mode such as observed for modes known as fishbones.

Fishbones are (m=1, n=1) MHD modes, known as internal kinks, that resonantly interact with trapped fast ions via their precession frequency. Fishbones are marginally stable and are driven unstable by a critical density of resonant fast ions through inverse Landau damping. Fishbones simultaneously cause a strong redistribution of the resonant fast ions that drive the instability in the first place. The name arises from the characteristic shape of the mode in signals such as soft X-ray emission, where the mode grows rapidly and then fades away as the mode expels fast ions only to grow again. Fishbones have been observed to cause a strong loss in fast ion content.

Non-resonant transport by MHD modes is, however, also observed such as in the case with sawteeth. Sawteeth are also the results of a (m=1, n=1) kink instability, which is primarily driven by the plasma current and causes the flux surfaces inside the q=1 surface to kink or deform. Sawteeth are known to strongly redistribute the core fast-ion content, with passing particles more strongly affected [35, 36].

Another class of modes known as Alfvén eigenmodes resonantly interact with fast ions, through their poloidal transit/bounce frequency. Alfvén modes are a type of transverse magnetic wave, that travel parallel to the magnetic field with the speed of the wave determined by the magnetic field tension due to the plasma density:

$$v_{\mathrm{A}} = \frac{B}{\mu_0 \sum_i n_{\mathrm{i}} m_{\mathrm{i}}}\,, \tag{2.26}$$

where i represents the plasma species present. The dispersion relation is given by $\omega = k_{\parallel} v_{\mathrm{A}}$, with:

$$k_{\parallel} = \left(n + \frac{m}{q}\right)/R\,, \tag{2.27}$$

where q is the safety factor and R the radius, so that $\omega \approx v_{\mathrm{a}}/R$. Alfvén waves are typically strongly damped as a wave packet with a certain radial extent would tear apart due to the frequency and velocity differing on neighbouring flux surfaces. However, various phenomena lead to gaps in the Alfvén dispersion spectrum, where the waves are no longer strongly damped and fast ions travelling at the Alfvén velocity are able to drive the modes unstable. A large "zoo" of Alfvén eigenmodes can exist that can be driven unstable by a sufficiently large density of resonant fast ions, and that redistributes both the resonant and non-resonant fast ions.

Edge Localised Modes

At sufficient heating, turbulence along the edge becomes suppressed creating a transport barrier such that the plasma transitions into a regime with enhanced confinement called the high confinement mode or H-mode [37]. The H-mode was first observed on the ASDEX tokamak [10] and is the foreseen operational regime for ITER [38]. H-mode plasmas are characterised by steep edge density and temperature gradients that form a pedestal close to the separatrix. The H-mode exhibits edge MHD instabilities that lead to quasi periodic collapse of the pedestal, expelling plasma particles and energy, known as edge localised modes ELMs [39].

ELMs pose a serious risk to future reactors such as ITER as they produce large transient heat loads on plasma facing components that reduce their lifespan through enhanced erosion. ELMs however also serve as a useful mechanism for flushing plasma impurities that otherwise dilute the plasma and radiate power away. For ITER ELMs will need to be mitigated or fully suppressed, and various techniques are being researched such as the use of RMP coils, pellet pacing [40, 41], or regimes with inherently small ELMs or that are completely free of ELMs.

Several ELM types have been classified with the most frequently encountered known as type I and III ELMs. Type III ELMs are smaller, leading to less energy loss per ELM as compared to type I ELMs that can eject up to 10 % of the plasma energy. Type III ELMs occur at heating power above but close to the L-H power threshold. Their frequency is observed to decrease with increasing heating power, and typically falls in the range 0.5 to 10 kHz. Furthermore type III ELMs are preceded by oscillations in the radial magnetic signal measured by pickup coils. Type I ELMs occur at heating power well above the L-H power threshold, and have much lower frequency in the range of 10 to 150 Hz. They occur as single events with relatively large periods compared to the profile recovery times. Type I ELMs have rarely been found to possess magnetic precursors, although a precursor oscillation in the edge temperature is observed. Type I ELMs are believed to be caused by a combined peeling-ballooning instability driven unstable by critical pressure and current. In this work we will consider type I ELMs.

An ELM burst lasts for a few 100 µs, causing a relaxation of edge profile gradients and affecting the profiles up to $\rho \sim 0.8$. The subsequent recovery of the plasma profiles to pre-ELM conditions lasts several milliseconds and has been observed to occur in phases with differing timescales for temperature and density. The recovery of the electron density gradient is found to be the most rapid on ASDEX Upgrade, recovering within 2 ms followed by the electron temperature gradient in 5 to 7 ms [42, 43, 44]. It is believed that separate transport mechanisms affect the electron density and temperature during their recovery. The ion temperature is found to recover on a similar time scale as the plasma density [45].

At the JET tokamak measurements of ion cyclotron emission (ICE) suggest that ELMs expel fast ions from the edge [46]. Measurements by fast-ion loss detectors installed at ASDEX Upgrade show increased fast-ion losses during ELMs [13]. These measurements also point to a filamentary structure of the fast-ion losses as is typically observed for the bulk plasma expelled by ELMs. Furthermore a possible acceleration of fast ions by ELMs

has been reported by [47].

2.4.5 Charge exchange losses

Plasma recycling, fuelling and to a lesser extent plasma recombination leads to the presence of background neutrals within the vacuum vessel. These neutrals serve as donor particles for charge exchange (CX) reactions with fast ions that acts as both a loss and redistribution mechanism:

$$D^0_{\text{donor}} + D^+_{\text{fi}} \rightarrow D^+_{\text{donor}} + D^{0*}_{\text{fi}}. \tag{2.28}$$

Fast ions that undergo a CX reaction effectively retain their initial momentum. Depending on their velocity vector at the moment of the reaction they might fly outward and be lost, or fly inward and be re-ionised. On smaller devices the presence of a large neutral density is found to contribute significantly to the loss of fast ions [48, 49, 50].

2.5 Neutral modelling

2.5.1 EMC3-EIRENE

The coupled plasma fluid (EMC3 [51]) and Monte Carlo neutral (EIRENE [52]) code EMC3-EIRENE has been used to calculate the 3D neutral density distribution for an ASDEX Upgrade discharge, as can be seen in figure 2.8. The modelling shows that density of the background neutrals is highest at the plasma edge and rapidly decreases towards the plasma centre, due to ionisation by the plasma. Since neutrals are not bound by the magnetic field the density distribution is both poloidally and toroidally asymmetric and depends strongly on the source. In the poloidal plane recycling is largest at the divertors due to the large plasma flux directed towards this region. Wall recycling is caused by ion fluxes against the plasma facing components and is relevant in the divertor region where the plasma strikes the first wall. The result is that the neutral density is two orders of magnitude larger at the divertor compared to the top of the device. However, at the outboard midplane, between $z = -0.5$ and 0.5 m the neutral density is found to not vary significantly, which is the region of interest for this work. As modelling the full 3D distribution is time consuming a more practical solution is to approximate the neutral density by a 1D model.

2.5.2 KN1D

Modelling of the 1D background neutral density is performed using the kinetic neutral transport code KN1D [53]. KN1D calculates the neutral D density profile in slab geometry given the plasma kinetic profiles namely the density (n_e), plasma temperatures ($T_{i,e}$) and the neutral D_2 pressure at the wall as input. KN1D additionally requires the magnetic field line connection length profiles as input, which is used to model the recycling of molecular deuterium D_2 on the sides of the local limiter surfaces.

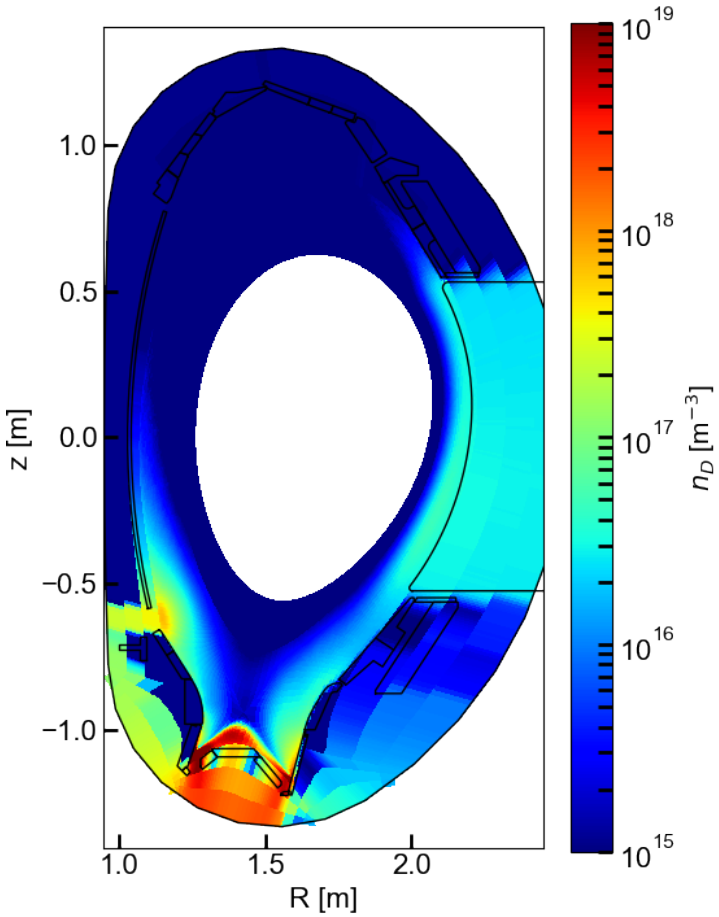

Figure 2.8: Poloidal projection of the background neutral D density calculated for ASDEX Upgrade using EMC3-EIRENE.

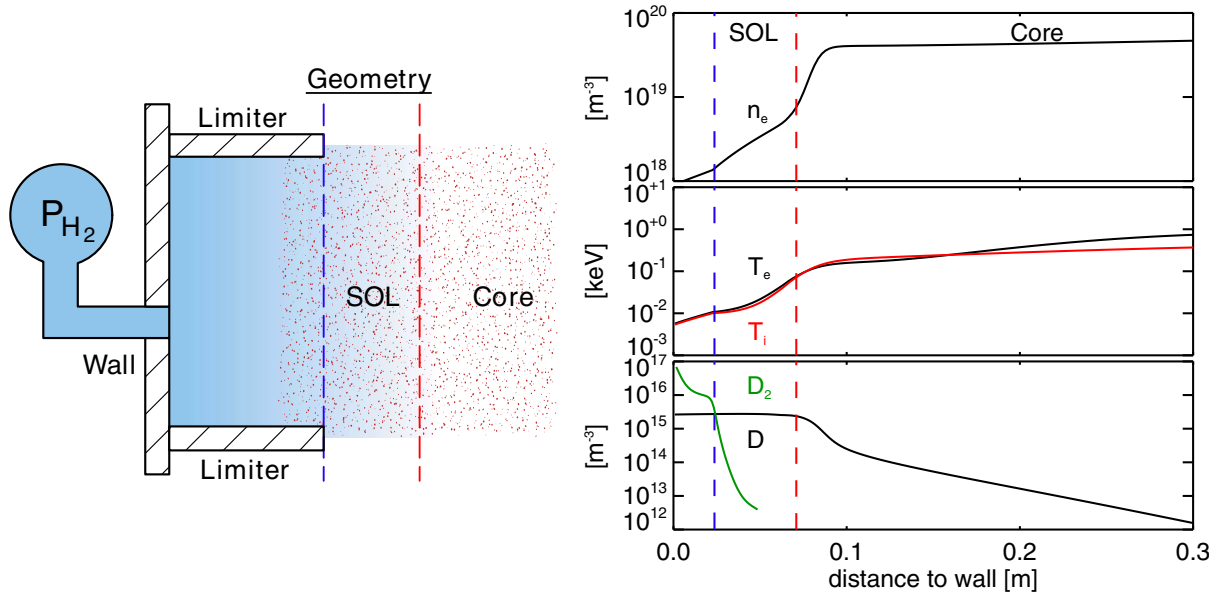

Figure 2.9: Left: Illustration of KN1D slab geometry taken from [53]. Right: Example input plasma density and temperature profiles plotted in the first two panels. The bottom panel presents the calculated neutral molecular and atomic D density profiles.

An illustration of the KN1D slab geometry is presented to the left in figure 2.9. The simulation domain extends from the wall up to a user defined distance into the plasma. The model includes effects of local limiters of the scrape-off-layer plasma, with the edge of the limiter shadow indicated by the blue dashed lines in figure 2.9. The separatrix, providing the boundary between open and closed field lines, is indicated with the red dashed lines. On the right are example profiles of n_e (top) and $T_{i,e}$ (middle) used to calculate the D_2 (in green) and D (in black) neutral densities profiles in the bottom panel.

Provided with the input described above the KN1D algorithm firstly calculates the phase space distribution function of the neutral D_2 followed by that of the neutral D. The evolution of the distribution functions are calculated using a method of successive collision generations, considering charge exchange reactions, electron-impact ionisation, dissociation, elastic self-collisions as well as elastic cross-collisions (atom-ion, atom-molecule, molecule-ion). The input wall pressure, assumed to be from neutral D_2 at room temperature (0.025 eV), is prescribed as a boundary condition for the molecular distribution calculation. The molecular calculation additionally provides the velocity space distribution of D resulting from the D_2 dissociation processes and is used as input for the atomic distribution calculation. KN1D finally provides atomic and molecular density profiles as output. In addition, neutral heat and particle fluxes, neutral temperatures, ionisation and molecular dissociation rate profiles, as well as Lyman and Balmer alpha emission are also provided.

The bottom panel of figure 2.9 shows the D_2 (in green) and D (in black) neutral densities profiles calculated from the example input. The molecular deuterium density is observed

mainly in the limiter shadow and sharply falls off in the SOL. The atomic deuterium shows a roughly constant density in the SOL, however, rapidly decreases across the plasma pedestal followed by a gradual decrease in the core.

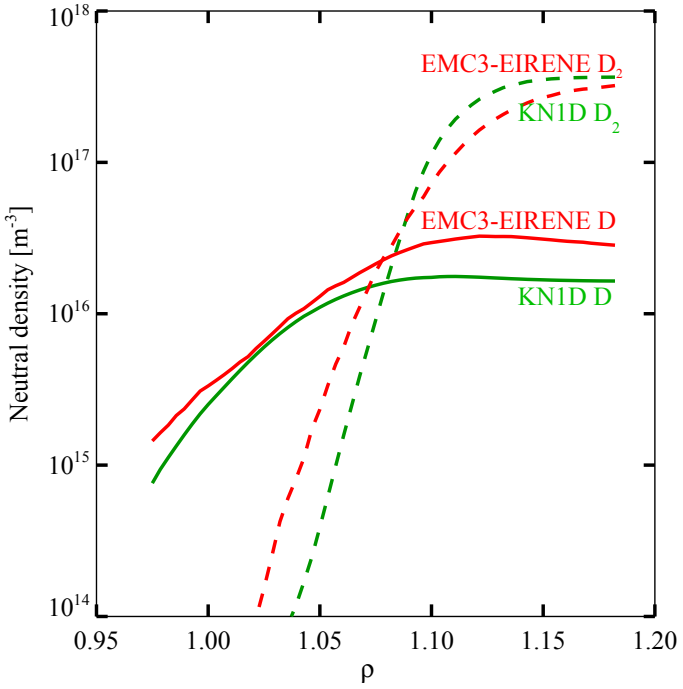

Figure 2.10: A comparison between the EMC3-EIRENE outboard midplane neutral D (solid lines) and D_2 (dashed lines) density profiles and the KN1D calculated profiles.

Figure 2.10 shows a comparison between the EMC3-EIRENE neutral density profiles (in red) taken at the outboard midplane and the KN1D neutral densities (in green) calculated with the EMC3 plasma kinetic profiles and molecular wall density. The dashed curves represent the molecular deuterium and the solid curves the atomic deuterium. The KN1D molecular density profile is larger compared to that predicted by EMC3-EIRENE in the far SOL ($\rho_{pol} > 1.1$). KN1D, however, predicts a rapid decay of the D_2 profile in the near SOL. This differs from the weaker molecular attenuation predicted by EMC3-EIRENE. The result is a higher atomic neutral D density predicted by EMC3-EIRENE, particularly in the far SOL. Nevertheless the agreement is sufficiently good that the 1D representation is considered to be a reasonable simplification for this work.

2.6 Fast-ion modelling

2.6.1 TRANSP and the NUBEAM module

TRANSP is a 1D plasma transport simulation code for tokamaks, developed and maintained by the Princeton Plasma Physics Laboratory (PPPL) [54]. TRANSP models plasma transport by solving a set of time dependent equations for particle, energy and momentum balance as well as poloidal field diffusion, given a necessary amount of input data. Quantities are mapped to a 2D equilibrium obtained from an internal solver, with the condition that quantities remain constant on a given flux surface. From this TRANSP is able to calculate various diffusion profiles and confinement times including a large amount of supplementary information of the plasma state, resolved in time. Importantly TRANSP is coupled to a fast-ion heating code that is able to calculate the time evolving 4D fast-ion distribution function resulting from NBI heating.

TRANSP can be used in an interpretative mode with plasma kinetic profiles and other experimentally measured quantities provided as input to perform an analysis of the plasma confinement properties. For this work TRANSP was used in the interpretative mode with the evolution of the plasma boundary, toroidal field, plasma current, loop voltage as well as the plasma kinetic and initial q profiles provided as input. Information of the heating systems such as power, timing and geometry is also provided.

TRANSP makes use of an auxiliary module called NUBEAM to model NBI heating [55]. NUBEAM calculates the deposition, slowing down and thermalization of fast ions from NBI heating. The code uses a Monte Carlo approach, injecting a user defined number of markers and calculating the birth locations resulting from ionisation reactions. The resulting fast ions are tracked on gyro centre orbits with their slowing down due to Coulomb collisions with charged plasma particles considered. Additionally charge exchange collisions with beam and background neutrals are also considered that may result in a redistribution or loss of the fast particle. Fast ion losses from unconfined orbits are also considered.

TRANSP uses another auxiliary module called FRANTIC to calculate background neutral particle transport [56]. FRANTIC calculates the 1D neutral density profile, for the corresponding plasma species, considering CX reactions and plasma impact ionisation reactions. For the calculation three neutral sources are considered namely neutrals resulting from recycling, gas flow and recombination. All sources are assumed to be evenly distributed around the flux surfaces. In this work gas flow neutrals are not considered. The magnitude of the recycling flux is, in part, determined by the flux of escaping ions (obtained from a particle balance calculation performed in TRANSP) which are considered to be 100 % recycled. Additionally, two options are available to control the magnitude of the recycling flux and provide the user control over the neutral density profile. The first option provides only indirect control as a user defined ion confinement time may be specified. In this case a larger confinement time results in a lower recycling flux and background neutral density (and vice versa). On the other hand the recycling flux can be directly specified as input. The recycling flux is further divided into warm and cold contributions by FRANTIC, with the warm recycling neutrals assigned the ion temperature at the plasma

boundary and the cold neutrals to a user defined temperature. The fraction of warm to cold recycling neutrals is given as input and provides additional control over the profile shape. Lastly the SOL neutral density is not modelled, but set to a user defined value.

2.6.2 LOCUST

LOCUST (the Lorentz Orbit Code for Use in Stellarators and Tokamaks) is a 3D full-orbit Monte Carlo code that simulates fast-ion motion in the presence of a plasma [57]. The code integrates the Lorentz equation for charged particle motion,

$$m\frac{d\vec{v}}{dt} = q\vec{v} \times \vec{B}\,, \tag{2.29}$$

in three dimensions and calculates the 5D fast-ion slowing down distribution function $F(R, z, \gamma, \cos\alpha, |\vec{v}|)$ for a given time point. Where γ is the particle gyro-angle and $\cos\alpha$ the pitch angle. Importantly LOCUST tracks and provides the fast-ion distribution outside the separatrix.

LOCUST is run on a GPU cluster at the Culham Centre for Fusion Energy (CCFE). The code requires as input the electron density, electron temperature and ion temperature profiles as well as the magnetic equilibrium for the desired time point. Additionally the fast-ion birth locations along the active NBI beams and the total beam heating power is required. The NBI birth locations can be obtained from a TRANSP simulation as they are calculated by NUBEAM. However, in this work FIDASIM (presented in chapter 4) is used instead as it is able to calculate the fast-ion birth locations outside the separatrix as well.

LOCUST has been benchmarked against an established 3D fast-ion code ASCOT, which uses a guiding centre approximation and a good agreement is found between the two codes [58]. However, unlike TRANSP these codes do not include CX reactions with a background neutral density.

Chapter 3

The ASDEX Upgrade Tokamak

The experimental work conducted during this PhD work was carried out at the ASDEX Upgrade tokamak. This chapter presents an overview of the device along with the relevant heating and diagnostics systems necessary for this work.

3.1 Overview

ASDEX Upgrade (AUG), pictured in figure 3.1, is a medium sized tokamak experiment in Garching Germany operated by the Max-Planck Institut für Plasmaphysik (IPP) [59]. The device was commissioned in 1991 as a successor (hence upgrade) to the ASDEX tokamak (1980-1990), the device on which the H-mode regime was discovered. AUG has a major radius of $R = 1.65\,\mathrm{m}$ and an elliptical cross section with a horizontal minor radius of $a = 0.5\,\mathrm{m}$ and vertical radius of $b = 0.8\,\mathrm{m}$. The sixteen "D-shaped" toroidal field coils can produce a magnetic field up to 3.1 T on axis. The standard field strength is 2.5 T and points in the clockwise direction as viewed from above. The plasma current I_P induced by the central solenoid is typically up to 1 MA, and plasma discharges can be as long as 10 s. The plasma position is controlled by a set of twelve poloidal coils and a passive stabilising loop. The plasma density typically ranges between 1×10^{19} and 1×10^{20} electrons per m^3 and temperatures can reach up to 20 keV [59].

The term ASDEX is an acronym for Axially Symmetric Divertor Experiment which refers to the use of a divertor, as tested by the predecessor of AUG. The concept of the divertor is to create a separatrix or last closed flux surface (LCFS) where field lines beyond the separatrix end in a region well separated from the main plasma. Compared to the use of limiters, this reduces the influx of impurities produced by sputtering of first-wall components. The reduction of the impurity influx is important since impurities provide strong cooling via line-radiation from bound electrons. Even at the high fusion relevant temperatures, heavy impurities are typically not fully ionised. In addition, the presence of impurities dilutes the fuel mixture which in turn reduces the efficiency of a fusion power plant. In the divertor concept the open field lines are guided to designated surfaces at an increased distance from the main plasma. Here, pumps are used to extract particles which

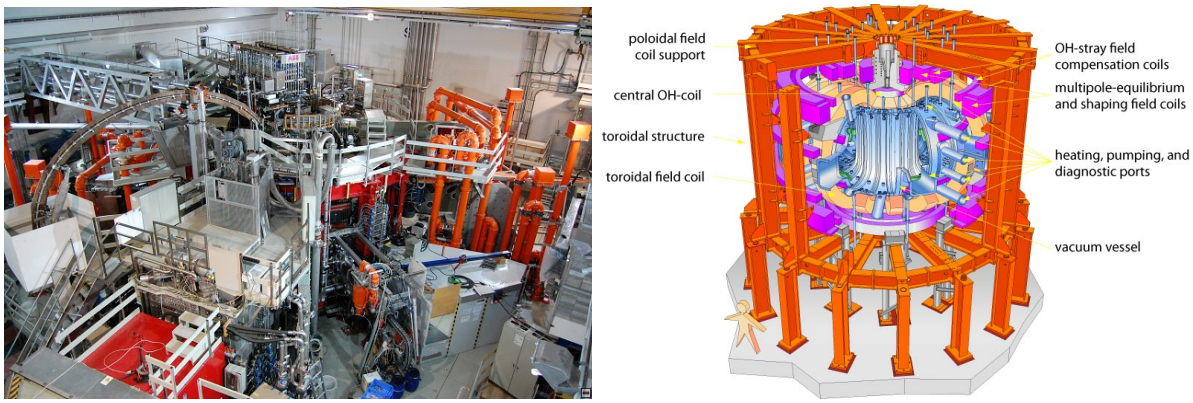

Figure 3.1: Left: AUG as seen from the outside. Right: A 3D CAD representation of AUG.

allows for better control of impurities. AUG is equipped with a pumped, lyre shaped lower divertor (see figure 3.2), optimised to meet the requirements of a future fusion reactor, as well as an open upper divertor without pumps. The standard plasma shape in AUG makes use of the lower divertor to form a single lower null plasma. Here null refers to the poloidal magnetic field component that vanishes at an X-point above the divertor.

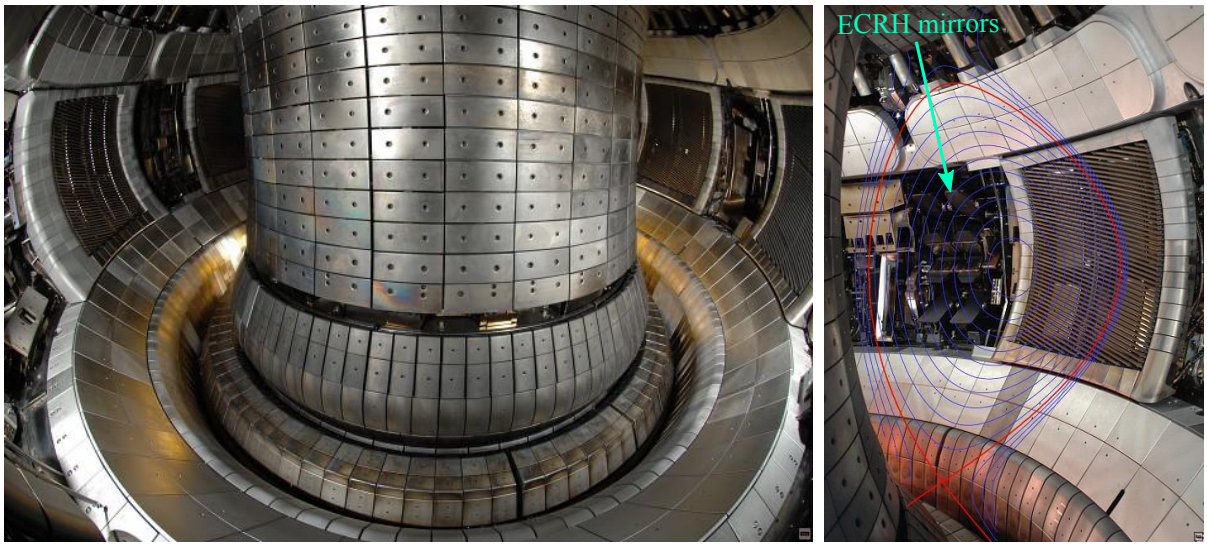

Figure 3.2: Left: A picture of the interior of AUG demonstrating the tungsten wall tiles and lower divertor. Right: A poloidal view of the interior of AUG with the magnetic flux surface geometry illustrated. The red line represents the separatrix. The X-point can be seen above the lower divertor.

AUG was designed to test fusion relevant design aspects and plasma conditions for future reactors, in particular ITER [59]. The magnetic geometry of AUG is close to that of ITER at one fourth the dimensions. An important contribution of AUG is to assess

the feasibility of tungsten as a first wall material. Carbon is typically used in many fusion devices due to its ability to tolerate high heat loads and its low atomic number Z. The latter implies that carbon becomes fully ionised at relatively low temperatures in the range of 500 eV such that no radiative power losses occur in the plasma core. However, carbon readily binds with hydrogen and its isotopes leading to chemical erosion and re-deposition in remote areas. In particular the bonding of tritium with carbon leads to a significant safety concern over uncontrolled tritium storage. The first walls of AUG have therefore been covered with tungsten, to study this high Z element as a wall material. Hereby, it could be shown that radiative losses from tungsten are well tolerable and that reliable tokamak operation is possible. This together with the JET tokamak ITER like wall project following the strategy of AUG [60] led, e.g. to the decision to equip ITER with a tungsten divertor.

3.2 Heating systems

AUG possesses powerful and flexible heating capabilities through neutral beam injection (NBI), electron cyclotron resonance heating (ECRH) and ion cyclotron resonance (ICRH) heating systems. These additional heating sources are needed to reach high temperatures since the efficiency of Ohmic heating due to the plasma current decreases with $T_e^{-3/2}$. The total available heating power at AUG amounts to more than 30 MW and allows studies with (P/R) values that are comparable with ITER [61]. In the following, NBI and ECRH are described as these two heating methods are relevant for this thesis project.

3.2.1 Neutral beam injection heating

AUG is equipped with two neutral beam injectors, referred to as boxes one and two, installed in sector 15 and 7, respectively as indicated in figure 3.3. Both boxes have four sources each with maximum extraction voltages of 60 and 93 kV respectively, where box one uses arc sources and box two uses radio frequency ion sources. The injected beams are labelled from Q1 to Q4 for box one, and Q5 to Q8 for box two, where Q stands for "Quelle" meaning source in German. Typically deuterium is injected for which the maximum injection power is 2.5 MW per beam for both boxes. The species-mix between D^+, D_2^+ and D_3^+ (i.e. full, half and third energy) beam particles are 0.47:0.36:0.17 for box one and 0.43:0.39:0.18 for box two.

The beam orientation is indicated in figure 3.3. As can be seen box one has a geometry that is more perpendicular to the magnetic field lines than box two. In particular beams Q6 and Q7 are close to tangential to the magnetic field lines. Unlike the other beams these two beams inject off axis to allow for off-axis current drive, and are particularly useful for the work presented here, as they produce the largest edge fast-ion density. Another important beam is Q3 which serves as the active diagnostic beam for the edge FIDA system discussed in chapter 5.

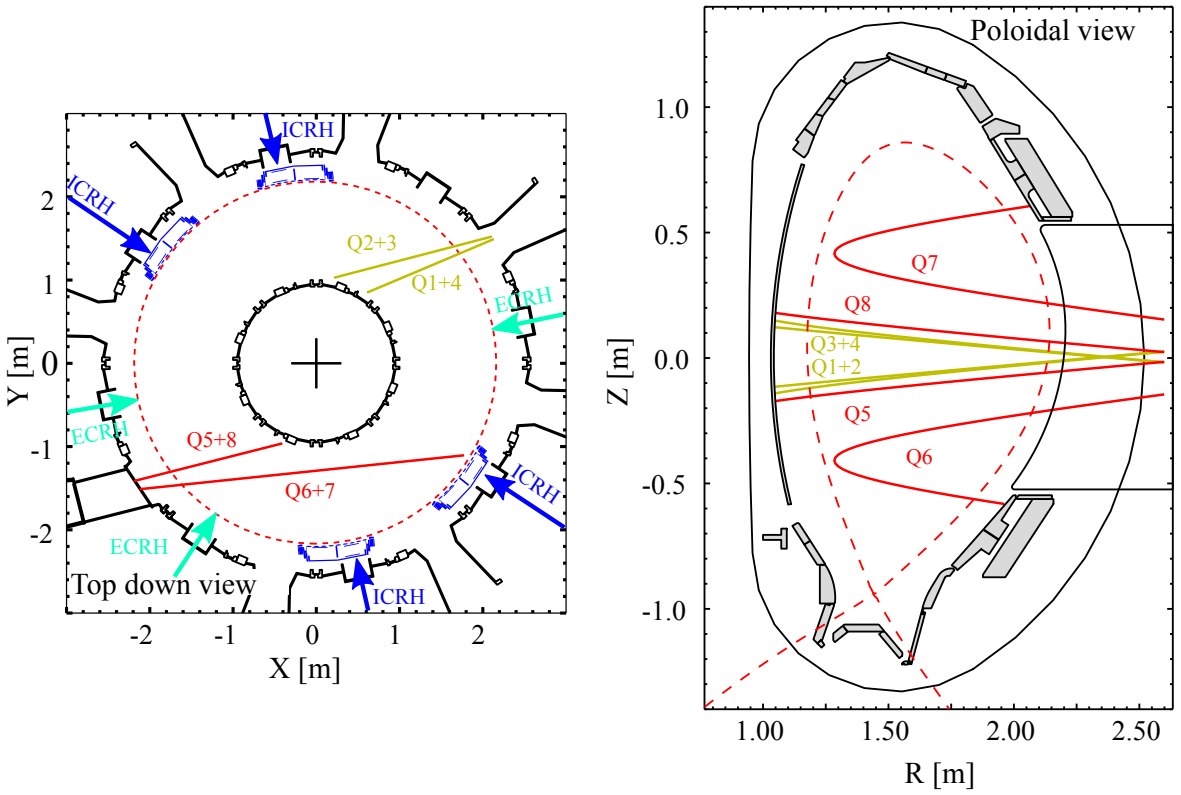

Figure 3.3: Left: Top down view of AUG illustrating the location of the NBI, ECRH and ICRH heating systems. Right: Projection of the beam paths in a poloidal plane of AUG illustrating the NBI injection geometry.

3.2.2 Electron cyclotron resonance heating

Electron cyclotron resonance heating (ECRH) works by accelerating electrons perpendicular to the magnetic field lines, through the injection of micro-waves with frequencies in the GHz range that interact resonantly with the gyro-motion of electrons. The wavelength of the applied microwaves is on the order of ∼2 mm, and the resonance condition allows highly localised heating, with a small broadening occurring due to relativistic effects. The ECRH system at AUG consists of eight gyrotrons which reliably deliver up to 5 MW of heating power to the plasma. The waves generated by the gyrotrons are transported through oversized wave-guides from the gyrotrons, to the torus, where the wave beam enters via a vacuum-window and is then steered to different locations in the plasma via turn-able mirrors (see figure 3.2). The system is able to operate at two frequencies, 105 GHz and 140 GHz. 140 GHz corresponds to the second harmonic frequency at the plasma centre (1.65 m) for 2.5 T operation and 105 GHz radiation can be used for central deposition during 1.8 T operation. The standard wave mode heating used on AUG is X-mode.

On axis heating with ECRH is typically required at AUG to prevent the accumulation of tungsten in the core, that would otherwise lead to a radiative collapse. The core electron

heating increases the level of plasma turbulence such that radial transport of tungsten is enhanced [62].

3.3 Diagnostics

AUG is equipped with a large suite of diagnostics to investigate and characterise plasma experiments. Below follows an overview of the most important diagnostics used during this work which include plasma kinetic profile, neutral pressure, and fast-ion diagnostics.

3.3.1 Kinetic profiles

Kinetic profiles refer to density, temperature and rotation velocity of the thermal distribution of ions and electrons. These are assumed constant on the magnetic flux surfaces such that they can be expressed as 1D profiles when being mapped onto ρ.

Electron temperature

Electron temperature T_e measurements are obtained from the electron cyclotron emission (ECE) and Thomson scattering diagnostics. The viewing geometry of these diagnostics is shown in Fig. 3.4. The ECE diagnostic measures the cyclotron radiation emitted by the gyrating thermal electrons. The frequency of this emission depends on the local magnetic field according to equation 2.4, such that radial information is obtained when observing different frequencies (remember that the magnetic field has a $1/R$ dependence). At AUG, the ECE diagnostic measures secondary X mode radiation across 60 channels with different frequencies with a sampling rate of 15 kHz and features a radial resolution in the mm range.

The intensity of the radiation contains information on the electron temperature. Radiation at the local cyclotron frequency is strongly absorbed such that the plasma can be considered optically thick and the emission can be treated as black body radiation. The emission intensity is given by Planck's law and is a function of the local T_e. However, the condition of optical thickness is often not met at the plasma edge and measurements might exhibit so-called shine-through [63].

This is why the Thomson scattering diagnostic is applied to infer information on the plasma edge temperature. Thomson scattering (TS) works by measuring the light scattered from an intense laser beam by the interaction of photons with electrons. The observed Doppler broadening of the scattered radiation contains information on T_e. AUG has two TS systems for core and edge measurements with 16 and 11 radial channels respectively [64]. The repetition rate of the lasers allows for profiles to be constructed every 12.5 ms for the core and 8.3 ms for the edge.

Electron density

TS allows to simultaneously obtain the electron density n_e from the intensity of the scattered light such that both T_e and n_e are obtained for the same measurement volume. The core electron density n_e measurements are obtained by the TS system as well as a system of interferometers.

The AUG interferometry system, as illustrated in figure 3.4, consists of five LOS from which the line averaged plasma density can be obtained with a sampling rate of 10 kHz [65]. Interferometry works by measuring the phase difference between laser light passing through the plasma and light travelling the same distance in vacuum. The phase difference is determined from the interference pattern produced by the two laser beams, and is proportional to the line integrated n_e.

The edge electron density is obtained from measurements with the lithium beam emission (Li-BES), thermal helium beam (HEB) and TS systems. The Li-BES diagnostic injects neutral Li particles into the plasma with an energy of 45 keV [66]. The excitation and ionisation of Li depends on T_e and n_e. A collisional radiative model is used to calculate n_e from the emission intensity. The Li-BES system provides a radial resolution of about 6 mm, with a time resolution of 50 µs. The attenuation of the Li beam means the profile is usually only obtainable up to the pedestal top. Measurements from the Li-BES and interferometry diagnostics are combined through a Bayesian modelling method to construct profiles of n_e, with a time resolution of 1 ms [67].

In addition, a thermal helium beam diagnostic has recently been installed on AUG. The diagnostic works by injecting neutral helium into the plasma. A line ratio technique is applied to determine the edge electron density from up to four He emission lines measured over 32 channels [68]. The tightly spaced lines of sight of the system provide a radial resolution of about 3 mm, with a time resolution of 1 ms.

Ion temperature and rotation

The ion temperature and rotation profiles are obtained from an extensive charge exchange recombination spectroscopy (CXRS) suite at AUG [69]. The principle of CXRS is to measure light emitted by a fully ionised impurity ion A with charge Z after a CX reaction with a donor deuterium neutral D from the NBI system:

$$A^{Z+} + D^0 \rightarrow A^{(Z-1)+*} + D^+. \tag{3.1}$$

After a CX reaction the captured electron, now bound to the impurity ion has a certain probability to be in an excited state (*) and will quickly relax to a lower state emitting a photon in the process. The CX reaction has little effect on the initial momentum of the impurity particle, therefore information of the particle velocity can be extracted from the Doppler shift of the associated emission lines. The thermal velocity distribution of the impurity particles leads to a Doppler broadening, while the rotation leads to a wavelength shift of the emission peak. The impurity density can be inferred from the emission intensity.

The CXRS system at AUG consists of in vessel optics that provide multiple LOS intersecting NBI beam Q3 at different radial locations for core and high resolution edge measurements as illustrated in figure 3.4. A second core CXRS system views beam Q8, but can also infer information when beam Q7 is operational. The light collected is transferred by optical fibres to spectrometers, with variable wavelength ranges to observe emission from different impurity species such as boron (BV 494.47 nm) or carbon ions (CVI 529.06 nm). The lowest time resolution of these systems is 2.3 ms, and is typically set when using NBI blips, however the standard time resolution is 10 ms, which provides improved signal strength.

It is assumed that the impurity and bulk plasma is in thermal equilibrium and thus have the same temperature and rotation. The advantage of measuring impurity CX emission, instead of deuterium, is that the spectrum is rather simple as it does not contain the beam emission and fast-ion contribution and can therefore be fitted with a Gaussian curve whose width corresponds to the impurity ion temperature.

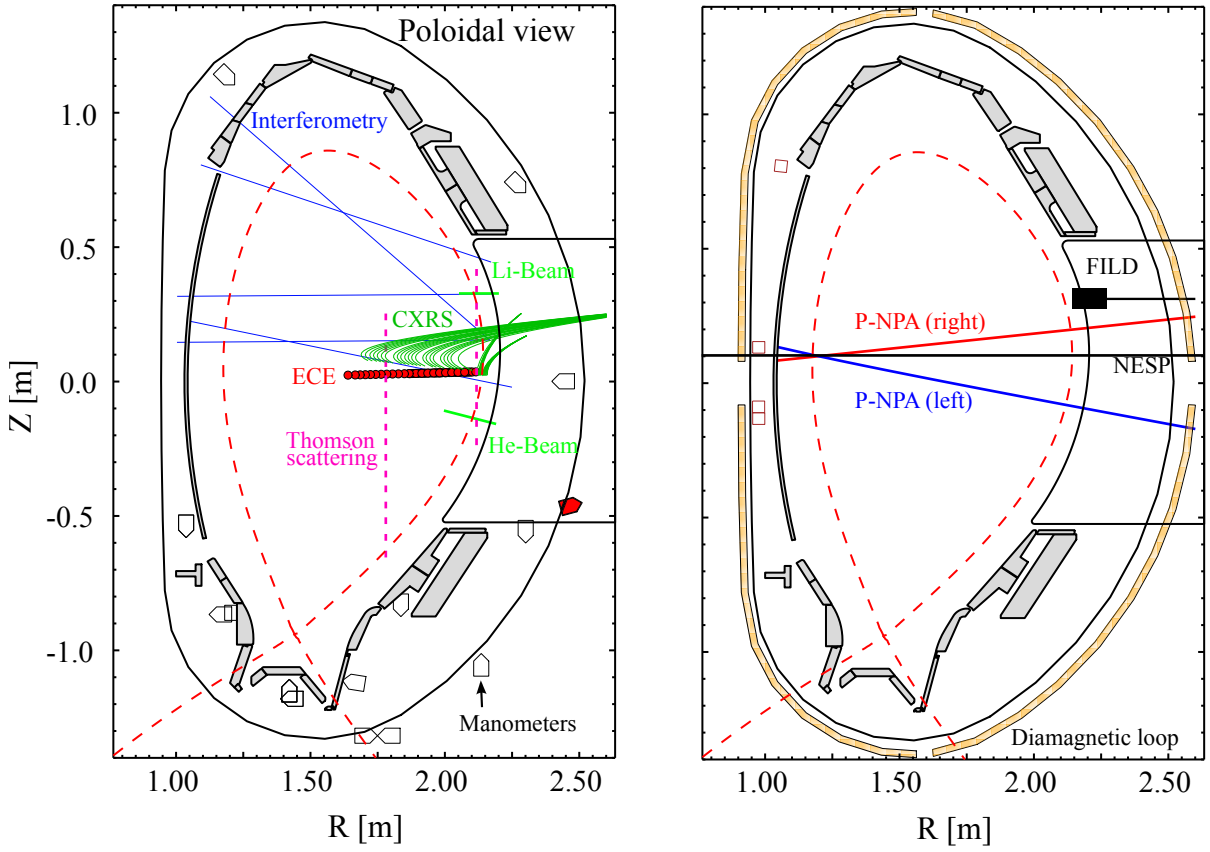

Figure 3.4: Poloidal geometry of the diagnostics systems made use of for this thesis work. The kinetic profile diagnostics and pressure gauges are presented on the left and the fast-ion diagnostics on the right.

3.3.2 Pressure gauges

AUG is equipped with a set of 20 poloidally and toroidally separated hot cathode ionisation gauges, from which the pressure can be inferred. The gauges are able to function at high magnetic field strengths and varying field-line angles [70], and provide a measurement of the neutral deuterium flux density F.

The density of neutral deuterium D_2 can be calculated from the measured flux F, with the assumption that the neutrals are at wall temperature ($T_{\text{wall}} = 0.025\,\text{eV}$). The relation

of density to flux is given by:

$$n_{\mathrm{D}_2} = \frac{F}{v_{\mathrm{D}_2}/m_{D_2}}\,, \tag{3.2}$$

where v_{D_2} is the average speed of the wall temperature neutral deuterium molecules ($310\,\mathrm{m\,s^{-1}}$), and m_{D_2} is the mass of a deuterium molecule (2 u). The neutral wall pressure can then be obtained from the ideal gas law $P_{\mathrm{wall}} = n_{\mathrm{D}_2} T_{\mathrm{wall}}$. This is an important parameter when modelling the background neutral density.

3.3.3 Fast-ion diagnostics

Apart from FIDA spectroscopy discussed in detail in the following chapter, there are several diagnostics measuring fast ion related information at AUG.

Fast Ion Loss Detector

Fast Ion Loss Detectors (FILD) measure escaping fast ions in the scrape-off-layer of the plasma. The detectors consist of a probe head, with a small collimating slit, through which fast ions may enter. The fast ions impinge on a scintillator plate that emits light on impact. The measurement of the fast-ion velocity distribution is possible since fast ions with different pitch values and energies will end up at different positions on the scintillator. The light emitted by the scintillator is typically measured by a CCD camera that observes the full scintillator with a frame rate of 25 to 100Hz, and an array of high speed photomultiplier tubes (PMT) that allow for measurements at 1 MHz with reduced velocity space resolution [71]. AUG has 5 FILD detectors at different R, Z positions that can address different parts of the fast-ion phase space.

Neutral Particle Analyser

Neutral Particle Analysers (NPAs) measure neutralised ions exiting the plasma. Neutralisation of both fast and thermal ions occurs through CX reactions with donor neutrals present in the plasma, which is further discussed in chapter 4. CX reactions with background neutrals lead to a passive flux of escaping neutrals while CX reactions with beam or halo neutrals would provide active NPA signals. AUG is equipped with one active [72] and two passive NPA systems. The two analysers of the passive systems (referred to as left and right) allows for energy resolved measurements of the neutral H and D flux along two views. However, it should be noted that only the passive NPA have been used during this thesis project.

The analysers are based on the design by [73], and work by collimating and ionising the arriving neutrals through the use of a gas stripping cell. The generated ions are deflected by means of a magnetic field, perpendicular to the collimated flux, that separate their trajectories according to their energy. An electric field parallel to the magnetic field causes an additional, perpendicular separation of the particles according to their mass. This allows to distinguish between the H and D flux. By choosing different magnetic and electric field strengths different energy ranges can be studied.

The analysers each have 2 rows of 10 detectors that serve as the species and energy channels respectively. The detectors measure individual counts which are binned in time

to obtain flux spectra with reasonable signal strength. Typically 1 ms provides sufficient signal strength for thermal particles, however this depends on plasma conditions.

A typical configuration used during this work is to measure high energetic D neutrals with $E = 8$ to 110 keV on one analyser and thermal D neutrals with $E = 0.5$ to 7.5 keV on the other. The pitch of escaping neutrals able to reach the detectors is determined by the angle between the LOS and the magnetic field. The observation angle of the analysers can be adjusted such that the pitch angle of escaping particles observed can be modified. In the standard configuration the left analyser observes particles with pitch angles around -0.35 and the right particles with pitch angle around ~ 0.

Diamagnetic Flux Loop

Poloidal plasma currents arise in presence of finite plasma pressures which, in turn, generate a toroidal magnetic field. This field can be measured via the so-called diamagnetic flux going through a coil that is wound around the poloidal cross-section. The diamagnetic flux is the difference in flux $\Delta\Phi$ generated due to the plasma field:

$$\Delta\Phi = -\int B_\Phi - B_{\Phi 0} dS\,, \tag{3.3}$$

where B_Φ is the toroidal magnetic field with a plasma and $B_{\Phi 0}$ without, and the integral is taken over the poloidal surface S of the plasma. It can be shown that $\Delta\Phi$ is proportional to the kinetic energy W related to the perpendicular motion of the particles [74]. $\Delta\Phi$ thus provides an indirect measure of W without the need for plasma profiles. The fast-ion pressure contributes to the diamagnetic flux such that the measurement is sensitive to fast-ion losses.

AUG is equipped with a diamagnetic flux loop diagnostic, which calculates $\Delta\Phi$ from the difference in the flux measured by a measurement loop Φ_m and a compensation loop Φ_c that accounts for changes of the magnetic flux caused by e.g. control coils [74]:

$$\Delta\Phi = \Phi_\mathrm{m} - \alpha_\mathrm{c}\Phi_\mathrm{c}\,, \tag{3.4}$$

where α_c is chosen so that $\Delta\Phi = 0$ with no plasma. The time resolution of this system is 1 ms, and a recent upgrade to the system with fast compensation probes allows for measurements down to 50 µs [75].

Neutron Emission

Measuring the neutrons produced by the fusion of deuterium ions provides another method to indirectly assess the fast-ion confinement. Deuterium-deuterium fusion has two reaction branches:

$$\mathrm{D} + \mathrm{D} \rightarrow 0.82\,\mathrm{MeV}\,{}^3\mathrm{He} + 2.45\,\mathrm{MeV}\,\mathrm{n} \quad (50\%) \tag{3.5a}$$

$$\mathrm{D} + \mathrm{D} \rightarrow 1.01\,\mathrm{MeV}\,\mathrm{T} + 3.02\,\mathrm{MeV}\,\mathrm{p} \quad (50\%)\,, \tag{3.5b}$$

of which only reaction 3.5a produces a neutron. The DD fusion cross-section strongly increases with energy, such that fast ions generated by the heating system are the predominant fusion reactants and may fuse with either other fast ions or thermal ions. The latter

is found to be the dominant process in typical experiments at AUG [76]. The number of fusion reactions and thus the neutron flux depends on the density of fast ions. AUG is equipped with a set of neutron detectors that cover different count-rate regimes and their data can be compared to the theoretically expected neutron rates from codes such as TRANSP.

Chapter 4

Fast-ion D-alpha Spectroscopy

Fast-ion D-alpha spectroscopy (FIDA) is a diagnostic technique used to investigate the density and distribution function of confined fast ions. This chapter presents first a description of FIDA spectroscopy, the main diagnostic method used during this thesis work, followed by the modelling tool used for the interpretation of FIDA data.

4.1 The FIDA technique

FIDA relies on measuring the Doppler shifted Balmer alpha emission from charge exchange (CX) reactions between fast hydrogenic ions and donor neutrals [77]. In the following we consider D plasmas and D fast ions, however, the same would apply to H or T.

$$D^0_{\text{donor}} + D^+_{\text{f}} \rightarrow D^+_{\text{donor}} + D^{0*}_{\text{f}} \tag{4.1}$$

During the CX reaction a fast deuterium ion D^+_{f} captures the electron from a donor neutral deuterium D^0_{donor}, ionising the donor neutral (D^+_{donor}), and neutralising the fast ion (D^{0*}_{f}). Before the reaction the donor neutral may be in an arbitrary excitation state, while the neutralised fast particle has a high probability to be in an excited state after the reaction. Additionally the fast particle is no longer bound by the magnetic field and will travel in a straight line. After a short time, and distance (<2 cm [78]), the excited particle will relax to a lower state emitting a photon. The large kinetic energy of the fast ion in comparison to the low binding energy of the electron to the donor neutral (<13.6 eV), results in a negligible change in momentum for the fast particle after the reaction. This means information of the local fast-ion distribution function can be extracted by measuring the emission of neutralised fast ions.

Several emission transitions are possible for excited deuterium. For FIDA spectroscopy, the transition from the $n = 3 \rightarrow 2$ state, known as the Balmer alpha (hence D-alpha) is used. The Balmer alpha emission has an un-shifted wavelength of 656.1 nm which corresponds to visible radiation such that standard and readily available optical components and cameras can be used.

FIDA spectroscopy can be performed actively by introducing a controlled source of donor neutrals via neutral beam injection. By using lines of sight that cross the NBI path at different radial locations, profile information is obtained. Additionally background neutrals present serve as a passive source of donor neutrals for CX reactions.

The radiance of the measured active and passive Balmer emission contains information on the fast-ion density, as CX reactions result in a population of fast neutrals in the $n = 3$ state. The number of these particles depends, however, not only on the density of fast ions, but also on the donor neutral density and CX cross-section, as well as other population mechanisms. The probability ($prob_{\mathrm{m}}$) for a fast ion to undergo a CX reaction and to be in the $n = 3$ state is given by:

$$prob_{\mathrm{m}} = \sum_{n} n_{0,\mathrm{n}} \left\langle \sigma_{\mathrm{cx(n\rightarrow m)}}(v_{\mathrm{rel}}) \cdot v_{\mathrm{rel}} \right\rangle , \tag{4.2}$$

where $\sum_n n_{0,\mathrm{n}}$ is the sum over the density of donor neutrals in the various excitation states n. The CX cross-section $\sigma_{\mathrm{cx(n\rightarrow m)}}$ depends not only the initial n and final m states, but is also function of the relative collision velocity v_{rel}. Therefore the product $\sigma_{\mathrm{cx(n\rightarrow m)}}(v_{\mathrm{rel}}) \cdot v_{\mathrm{rel}}$, known as the rate coefficient, must be averaged over the relative velocity between a given fast ion and the ensemble of donor neutrals, here indicated by the brackets.

Other mechanisms that contribute to the density of fast neutrals in the $n = 3$ state include the de-excitation of fast neutrals in higher excited states by spontaneous de-excitation or through collisions with electrons and ions. Collisions with electrons and ions also excite a fraction of fast neutrals from lower states to the $n = 3$ state. However, for particles with energy in the range of 10 to 50 keV, the dominant population mechanism is CX reactions. Thus the majority of FIDA emission results from emission of fast neutrals in the n=3 state due to CX reactions and the FIDA radiance measured along a line of sight can then approximated by:

$$I_{\mathrm{FIDA}} \approx \int n_f \sum_{n} n_{0,\mathrm{n}} \left\langle \sigma_{\mathrm{cx(n\rightarrow 3)}}(v_{\mathrm{rel}}) \cdot v_{\mathrm{rel}} \right\rangle f_{3\rightarrow 2} dl \, , \tag{4.3}$$

with $f_{3\rightarrow 2} = A_{32}/(A_{32} + A_{31})$, where A_{32} and A_{31} are the Einstein coefficients for spontaneous de-excitation from the $n = 3$ to $n = 2$ and $n = 1$ states, respectively [79]. Here collisional de-excitation is considered negligible.

The spectral shape of the measured emission provides information on the fast-ion distribution function. This is because the motion of the emitting deuterium atoms causes a Doppler shift of the emission when observed with a given line of sight, such that these contributions are generally shifted from $\lambda_0 = 656.1\,\mathrm{nm}$. The magnitude of the Doppler shift $\Delta\lambda_{\mathrm{Doppler}}$ is determined by the projection of velocity vector $\vec{v}_{\mathrm{n}}$ of the excited neutral with the line of sight unit vector $\vec{e}_{\mathrm{LOS}}$:

$$\Delta\lambda_{\mathrm{Doppler}} = \lambda_0 \frac{\vec{v}_n \cdot \vec{e}_{\mathrm{LOS}}}{c} \, , \tag{4.4}$$

where c is the speed of light. As an example $\Delta\lambda_{\mathrm{Doppler}}$ for a 20 keV emitting deuterium, with its velocity parallel to the LOS will be about 3 nm and for a 90 keV particle it will be about 6.4 nm.

A small additional shift in wavelength (typically <1 nm) occurs due to the motional stark effect (MSE). The MSE results from the electric field experienced in the particle frame of reference due to its velocity in the presence of a magnetic field, $\vec{E} = \vec{v} \times \vec{B}$. The electric field causes a separation of the otherwise degenerate states such that the n-th level splits into $(2n-1)$ finer energy levels. For $n = 3$, fifteen transitions are possible with two linear polarisation components arising from transitions with $\Delta m = 0$ (the difference in magnetic quantum number) known as the π lines, perpendicularly polarised to the magnetic field, and transitions with $\Delta m = \pm 1$ known as σ lines, parallel polarised to the magnetic field [80].

Directly calculating the fast-ion velocity-space distribution from the measured FIDA spectra is difficult for two reasons. Firstly the relation between the velocity of an emitting particle and the emission wavelength is ill-posed as the observed Doppler shift does not uniquely correspond to a given pitch or energy of the particle. This is because a given Doppler-shift can be reached by a variety of pitch values, energies and gyro-angles, since only the projection of the velocity vector to a given line of sight matters. This limits the velocity space resolution as observed in the wavelength domain which is worsened by the D-alpha line splitting due to the MSE. The energy dependence of the CX cross-section further complicates the direct interpretation of FIDA spectra. To mitigate this multiple lines of sight which provide access to different projections of the velocity space can be used. Furthermore, to directly calculate the fast-ion density from the measured spectra requires precise knowledge of the donor neutral densities. Secondly, the emission from other D-alpha contributions obscures a part of the faint FIDA emission, such that only the large Doppler shifted FIDA emission is discernible from these large noise sources. A quantitative interpretation of the FIDA emission, therefore, requires forward modelling [81] or tomographic reconstructions [82].

4.2 Forward modelling using FIDASIM

For this work forward modelling was performed, using the FIDASIM Monte Carlo code [81, 8]. FIDASIM is able to calculate synthetic D-alpha spectra and neutral particle fluxes, from a given theoretical fast-ion distribution as well as the plasma kinetic profiles, magnetic equilibrium, NBI injection power and geometry and the diagnostic sight line geometry. The degree of match between the calculated and measured spectra and fluxes determines how well the input data, in particular, the fast-ion distribution, represents the actual quantities.

4.2.1 The FIDASIM approach

FIDASIM calculates the density and excitation states of various donor and CX neutrals within a 3D grid for a single time point. This is done by launching and tracking neutral Monte Carlo (MC) markers, on straight trajectories through the simulation grid. A collisional radiative (CR) model is used to model the interaction of the neutral particles with the plasma. The plasma kinetic profiles and the magnetic equilibrium are therefore

required as input and are mapped to the simulation grid. The CR model calculates the state-resolved neutral flux associated with the MC markers. Importantly the CR model is able to calculate the emission resulting from the excited neutrals.

4.2.2 The FIDASIM collisional radiative model

The CR model of FIDASIM models the ionisation and attenuation of neutral hydrogenic atoms due to the interaction with the plasma. The following set of atomic processes are considered by the model:

$$\begin{aligned}
e^- + H(n) &\rightarrow e^- + H^+ + e^- && \text{electron impact ionisation} \\
e^- + H(n) &\rightarrow e^- + H(m) && \text{electron impact (de-)excitation} \\
\\
H^+ + H(n) &\rightarrow H(m) + H^+ && \text{proton charge exchange} \\
H^+ + H(n) &\rightarrow H^+ + H^+ + e^- && \text{proton impact ionisation} \\
H^+ + H(n) &\rightarrow H^+ + H(m) && \text{proton impact (de-)excitation} \\
\\
I^{Z+} + H(n) &\rightarrow I^{(Z-1)+} + H^+ && \text{impurity charge exchange} \\
I^{Z+} + H(n) &\rightarrow I^{Z+} + H^+ + e^- && \text{impurity impact ionisation} \\
I^{Z+} + H(n) &\rightarrow I^{Z+} + H(m) && \text{impurity impact (de-)excitation} \\
\\
H(n) &\xrightarrow{n>m} H(m) + \gamma && \text{spontaneous de-excitation}\,,
\end{aligned} \tag{4.5}$$

where H refers to all isotopes of hydrogen, as their cross-sections are nearly identical when considering collision energies per atomic mass unit. Here m and n are the initial and final excitation states respectively and I^{Z+} refers to an impurity ion with charge Z. Usually only one impurity species is considered in FIDASIM, namely carbon, although nitrogen, boron and beryllium can be used instead. The emission of Balmer alpha photons is modelled by spontaneous de-excitation with the probability of de-excitation and the emission of a photon γ described by Einstein coefficients.

Since the different excited levels are coupled to each other, the collisional radiative model solves a set of coupled linear differential equations. In FIDASIM exited states up to n=6 are typically considered while excitation to higher levels is treated as a loss mechanism.

For the collisional radiative model, reaction rates are needed for the individual processes which are given by the product of the corresponding densities (e.g. the electron density for electron impact ionisation) and the effective rate coefficients. The latter can be calculated by the Maxwell average of cross-sections times the relative collision velocity $\langle \sigma \cdot v \rangle$ and have been tabulated for FIDASIM.

The CR model calculates the marker associated neutral flux, density and importantly the radiation resulting from excited neutrals, which is used to calculate synthetic spectra.

4.2.3 FIDASIM synthetic spectra

Based on the amount of photons calculated per cell by the CR model, FIDASIM then determines synthetic spectra observed by user defined lines of sight with realistic diagnostic geometry. The wavelength of the photons is calculated from the projection of the marker velocity with the LOS vector to obtain the Doppler shift, according to equation 4.4. The wavelength splitting due to the MSE is calculated considering the electric field strength experienced in the particle frame of reference, $\vec{E} = \vec{v} \times \vec{B}$ by means of the following equation:

$$\Delta\lambda_{\mathrm{MSE}} = |\vec{v} \times \vec{B}| \cdot S_\lambda(i) \cdot 10^{-17} \cdot \lambda_0^2 \quad [\mathrm{nm}]\,, \tag{4.6}$$

where i indicates the individual transitions with the values for $S_\lambda(i)$ used from [83].

The emission intensity in $[\mathrm{Ph\,s^{-1}\,nm^{-1}\,cm^{-3}}]$ is weighted by the LOS length through the cell and multiplied by $10^4/4\pi$ to convert the intensity to $[\mathrm{Ph\,s^{-1}\,nm^{-1}\,m^{-2}\,sr^{-1}}]$. Lastly the intensity of the individual Stark lines is obtained by multiplying each contribution by the relative intensity calculated by:

$$\begin{aligned} I_{\mathrm{rel}}(i) &= S_{\mathrm{I}}(i) \cdot \left(1 \pm \cos\left(\hat{e}_{\mathrm{LOS}}, \vec{v}_{\mathrm{n}} \times \vec{B}\right)\right) \\ I_{\mathrm{rel}} &= \frac{I_{\mathrm{rel}}(i)}{\sum_i I_{\mathrm{rel}}}\,, \end{aligned} \tag{4.7}$$

where the plus in the brackets applies to the σ lines and the minus to the π lines and the values for $S_{\mathrm{I}}(i)$ also obtained from [83].

4.2.4 Active contributions

The active contributions to the D-alpha spectrum consist not only of FIDA emission but also of emission from excited beam neutrals and emission of thermal neutrals known as the beam halo. These contributions along with a description of the FIDASIM procedure for simulating the associated neutrals is presented here.

The manner in which the basic FIDASIM approach described in section 4.2.1 is carried out differs according to the type of donor neutral. For simulations of the active contributions the beam neutrals are simulated first.

Beam emission and simulation

Injected beam neutrals are excited through electron and ion impact collisions and produce a distinct spectral feature in the D-alpha spectrum. This is because NBI neutrals have a well defined injection energy and velocity vector, resulting in well defined Doppler shifts. Typically 3 beam emission contributions are present as a result of the full, half and third energy beam particles as demonstrated in figure 4.1a. In addition, the motional Stark (MSE) effect splits the individual energy components into 15 lines, each. Those lines feature pi and σ lines as illustrated in figure 4.1b.

FIDASIM simulates the beam neutrals by launching beam markers from the position of an NBI-ion source given as input. The number of markers to be launched is calculated from the user defined total number of markers, divided by the number of sources to be

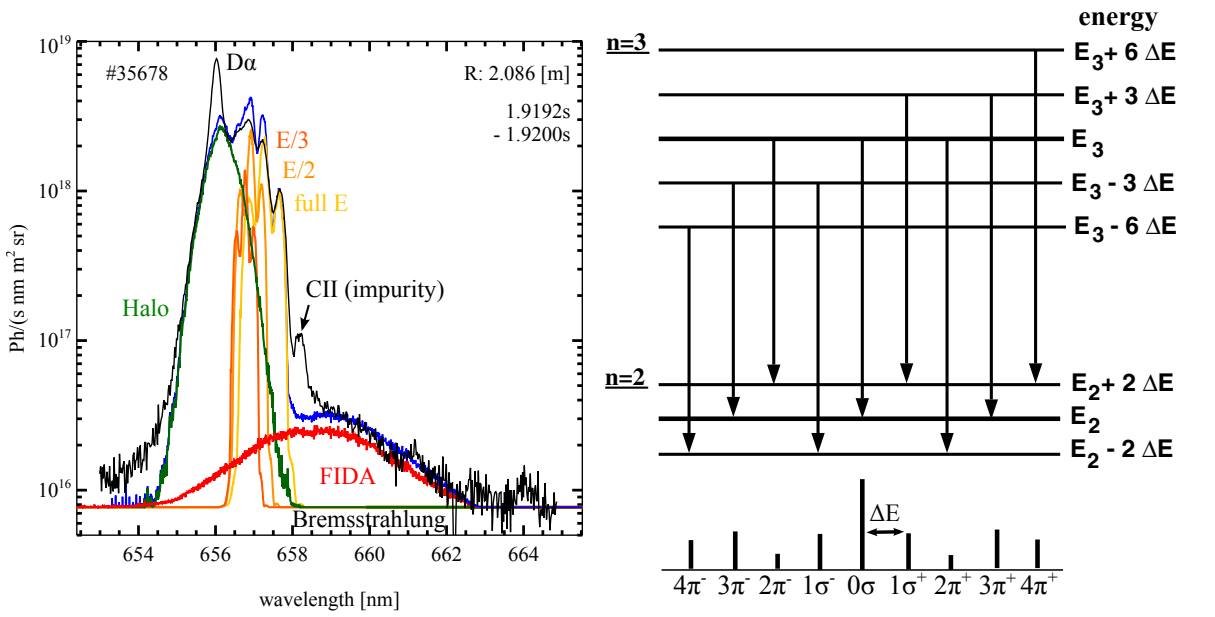

Figure 4.1: Left: Example of the Balmer alpha spectrum measured at AUG (black) along a LOS viewing NBI Q3. The FIDASIM calculated synthetic spectrum is over plotted in different colours according to the contribution type. Note here that the calculated passive FIDA contribution is omitted (see fig. 4.3a). Right: Illustration of the energy level splitting due to the linear Stark effect, and resulting transitions allowed by selection rules.

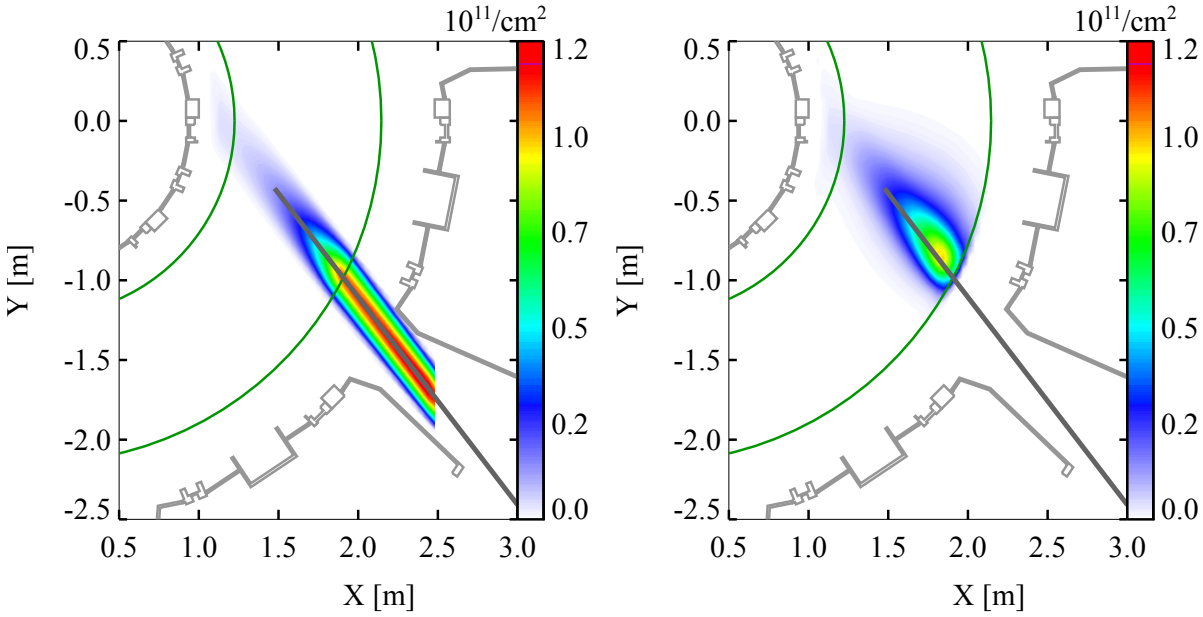

Figure 4.2: Top down view of the FIDASIM calculated beam neutral density (left) and halo density (right) for NBI Q3. The green lines indicate the midplane separatrix positions.

simulated and weighted by the given NBI source species mix. The velocity of each marker is determined from the species energy. The direction and the velocity is determined from the beam geometry that includes for the beam sources divergence and focus. In addition, NBI vectors that would intersect the beam aperture, as defined in the inputs, are discarded. The initial neutral flux associated with the marker is determined from the beam power divided by the average energy per beam particle, with the marker neutrals set to be in the ground state before entering the grid. The density of beam neutrals is calculated along the path of a given marker and for each cell resulting in the spatial n_{beam} distribution as shown in figure 4.2a.

Halo emission and simulation

The halo refers to a cloud of plasma thermal neutrals that forms around the injection beam due to CX reactions with thermal plasma ions. The halo consists of neutrals born directly through CX between the injected beam neutrals and the thermal plasma ions, referred to as direct charge exchange (DCX) neutrals, as well as secondary neutrals resulting from CX reactions between the DCX neutrals and thermal ions. This secondary process may repeat several times, but diminishes as the neutrals are ionised through impact processes that ensure only a few generations occur. The halo spectral shape is determined by the Doppler shift due to the thermal velocity distribution of the plasma ions. The result is a Gaussian feature with a width determined by the local ion temperature and an offset from λ_0 due to the plasma rotation as shown in green in figure 4.1a.

The FIDASIM halo simulation is carried out in two parts, firstly the DCX neutrals are simulated followed by the secondary halo neutrals. The simulation starts by calculating the number of MC markers to launch per cell. This is determined by the total fraction of beam neutrals times the ion density in each cell multiplied by a user defined number of markers to simulate. The simulation then iterates over each cell in the grid and calculates the CX rate of beam neutrals with the local density of thermal ions. To obtain the marker associated number of neutrals the beam and ion density is multiplied with the tabulated CX reaction rate, discussed in section 4.2.2. Each marker is then launched with a velocity vector sampled from a Maxwell distribution, offset by the local toroidal rotation velocity. The density of DCX neutrals is stored for each cell and used to calculate the density of secondary halo neutrals in the next part of the halo simulation.

The secondary halo neutrals are simulated very similarly to the DCX neutrals with the only difference that now the DCX neutrals are considered as donor neutrals. This is repeated up to 20 generations or until the current density of halo neutrals is less than 1% of the DCX neutral density. The ionisation of the halo neutrals leads to less donor neutrals for successive generations, such that typically only a few generations need to be simulated. The combined density of DCX and secondary neutrals are stored for each cell. Figure 4.2b shows an example of the halo neutral density calculated for beam Q3.

Active FIDA simulation

Active FIDA emission results from CX reactions between fast ions and either beam or halo neutrals. The FIDA emission has a large Doppler shift that separates the emission from other Balmer-alpha contributions such as the beam and halo emission and makes the measurement of the relatively weak fast-ion emission possible (see fig. 4.1a). The measured

spectral shape and intensity contains information of the fast-ion velocity distribution and density as described in section 4.1.

The FIDASIM simulation of the active FIDA neutrals requires that a theoretical fast-ion distribution is provided as input. The simulation starts by calculating the number of MC markers to launch per cell. This is determined from the density of beam and halo neutrals times the fast-ion density in each cell multiplied by a user defined number of markers to simulate. The simulation then iterates over the simulation grid and for each cell iterates further over the number of markers calculated. The fast-ion marker velocity is sampled from the input fast-ion distribution. A calculation is performed to determine the position of the fast ion based on its Larmor radius. The probability for the fast ion to neutralise is calculated from the CX cross-section which depends on the NBI velocities and thermal velocities. The FIDA neutral is then tracked and the density of FIDA neutrals stored for each cell. Additionally the position at which a FIDA neutral is born, is stored if the marker path crosses a LOS, which allows to assess the radial resolution of a given LOS as shown later.

4.2.5 Passive contributions

Passive contributions to the radiation in the D-alpha wavelength range include Balmer emission due to CX reactions of background neutrals as well as unshifted Balmer emission from recycling neutrals referred to as cold D-alpha.

FIDASIM simulates the passive CX as well as Bremsstrahlung emission independently from the active signals. The passive CX simulations require a background neutral density to be provided, that is mapped to the simulation grid. As the passive emission is not well localised the grid size needs to be appropriately large to cover the full LOS path through the plasma.

Passive FIDA

Of particular interest to the work of this thesis is the passive FIDA emission, which results from CX reactions between background neutrals and fast ions. In contrast to active FIDA light the passive emission is not well localised. Instead the emission occurs predominantly along the plasma edge where the background neutral density is highest and exponentially decreases towards the plasma core due to the attenuation of the neutral density. Passive FIDA radiation is useful as it contains not only information on the edge fast-ion density and distribution but also on the background neutral density. However, the dependence of the emission on two quantities results in an ambiguity. Information on both, the fast-ion and background neutral density is required to interpret the emission.

FIDASIM performs the passive FIDA simulation in the same manner as the active FIDA simulation. However, instead of the beam and halo neutrals the user defined background neutral density is considered for calculations. Furthermore before calculating the probability for a fast ion to be neutralised, the CR radiative model is applied to determine the equilibrium population of states of the background neutrals. The neutralisation probability is then calculated with the neutrals considered to be thermal and assigned the local ion temperature. Figure 4.3a demonstrates the synthetic passive FIDA spectrum cal-

culated by FIDASIM compared to the experimentally measured spectrum for an example discharge.

Passive thermal CX

Another CX emission contribution results from reactions between background neutrals and thermal ions, here referred to as passive thermal emission. As with the halo contribution, the spectral shape of the emission is characterised by a Doppler broadening due to the ion temperature. The spectral shape, however, resembles a Gaussian due to the ion temperature variation along the LOS, as can be seen in figure 4.3a. The intensity of the emission is proportional to the density of background neutrals, but also depends on the plasma density and temperature.

Modelling of the passive thermal emission has been included to the FIDASIM project during the course of this PhD work. This was motivated by a need to constrain the background neutral density in order to resolve the ambiguity when assessing the passive FIDA intensity which is dependent on both the fast-ion and background neutral densities. Knowledge of the plasma kinetic quantities allows to unambiguously assess the background neutral density through forward modelling of passive thermal emission.

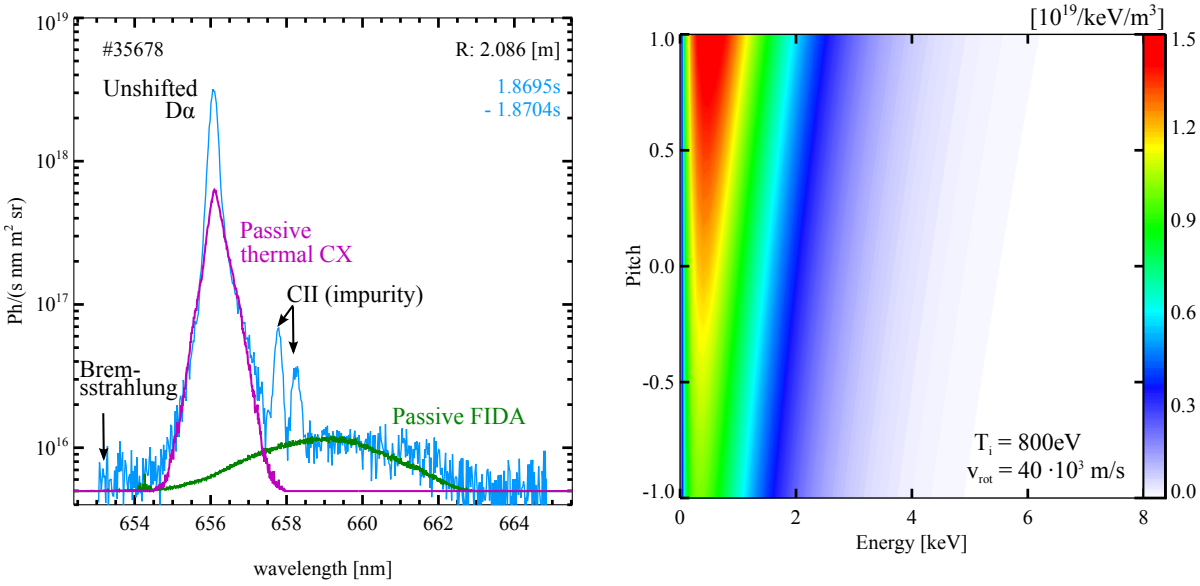

Figure 4.3: Left: Example passive Balmer alpha spectrum measured on AUG (blue) with the passive thermal CX (magenta) and FIDA (green) emission calculated by FIDASIM over plotted. Right: Representation of the thermal velocity distribution corresponding to the plasma conditions calculated with eq. 4.8.

The simulation method is once again similar to the active FIDA simulation. However, here a shifted Maxwell distribution is used when sampling MC marker velocities. "Shifted" refers to the offset caused by the toroidal rotation. The formulation for a shifted Maxwell

distribution in terms of pitch and energy is presented in [7]:

$$F(E, \text{pitch}) = \frac{n_\text{D}}{T_\text{i}^{3/2}} \sqrt{\frac{E}{\pi}} \cdot \exp\left(-m \frac{\left(v_\parallel - v_{\text{rot}\parallel}\right)^2 + v_\perp^2}{2T_\text{i}} \right), \tag{4.8}$$

with:

$$v_\parallel = \sqrt{\frac{2E}{m}} \cdot \cos\alpha \quad v_\perp = \sqrt{\frac{2E}{m}} \cdot \sqrt{1 - \cos^2\alpha}\,, \tag{4.9}$$

where pitch $= \cos\alpha$.

Figure 4.3a demonstrates the synthetic thermal CX spectrum calculated by FIDASIM which compares well to the experimentally measured spectrum. The neutral density is, therefore, considered to be representative of the experimental conditions and the passive FIDA spectrum can be calculated unambiguously. The synthetic passive FIDA spectrum also matches with the measured spectrum reasonably well meaning the theoretical fast-ion distribution is representative of the experimental distribution. Figure 4.3b illustrates a shifted Maxwell distribution, in terms of energy and pitch, used by FIDASIM for the calculation of the passive thermal CX spectrum presented in fig. 4.3a.

Bremsstrahlung

Bremsstrahlung results from Coulomb collisions of electrons with ions. The intensity of the Bremsstrahlung depends on the plasma density, temperature and impurity concentration and has a weak wavelength dependency described by equation 4.10. Bremsstrahlung contributes to the photon noise measured, therefore experiments are often carried out with low density plasma to reduce the Bremsstrahlung intensity. This has the added benefit of large fast-ion fractions due to the longer slowing down time and increases the FIDA signal.

The FIDASIM Bremsstrahlung calculation is performed by iterating over each LOS path and calculating the cumulative emission along the path as given by [84]:

$$I_\text{bremss}(\lambda) = 7.57 \cdot 10^{-8} \cdot \frac{1}{\text{s nm m}^3\,\text{sr}} \cdot \text{nm}\sqrt{\text{eV}}/\text{cm}^6 \cdot \frac{g n_\text{e}^2 Z_\text{eff}}{\lambda\sqrt{T_\text{e}}} \exp\left(\frac{-hc}{\lambda T_\text{e}}\right), \tag{4.10}$$

with: $g = 5.42 - (3.108 - \ln T_\text{e}[\text{eV}])(0.6905 - 0.1323/Z_\text{eff})$.

Other contributions not modelled by FIDASIM

The following passive contributions are not simulated by FIDASIM, but their description is included for completeness.

Cold D-alpha

The brightest contribution to the D-alpha spectrum results from recycled neutrals excited dominantly by electron impact collisions. This contribution is orders of magnitude larger than the FIDA contributions representing a significant challenge to measure both given the limited dynamic range of cameras. It is desirable, however, to measure this contribution along with the passive thermal emission as it also contains information on the density of background neutrals.

Impurity and molecular radiation
Radiation from impurity sources presents another unwanted source of noise. Line emission within the FIDA range complicates the interpretation of the FIDA emission and may completely obscure the FIDA contribution if the intensity is large. The largest impurity contributions in the D-alpha wavelength range are typically from carbon and oxygen. Metallic impurities such as tungsten may also appear but generally have multiple, less intense, closely spaced lines that merge to form a continuum. Similarly molecular lines such as from D_2 also contribute to the background continuum emission. This is especially observed during gas puff injections.

4.2.6 FIDASIM neutral flux

FIDASIM is able to simulate the energy resolved neutral flux for a user defined NPA detector, discussed in section 3.3.3. The simulation is again similar to the active FIDA approach, however, only cells that fall within the opening angle of the detector are considered and only markers with gyro angles that can reach the NPA detector are spawned and followed. This greatly increases the speed of the simulation as many cells and marker trajectories may be ignored. Markers that may reach the detector are followed and the CR model applied to determine the flux of particles that reach the detector as shown in figure 4.4. As with the synthetic spectra it is possible to simulate both the active and passive neutral fluxes given a fast-ion distribution and background neutral density. Figure 4.4 also compares the synthetic NPA flux to the measured flux for an example discharge.

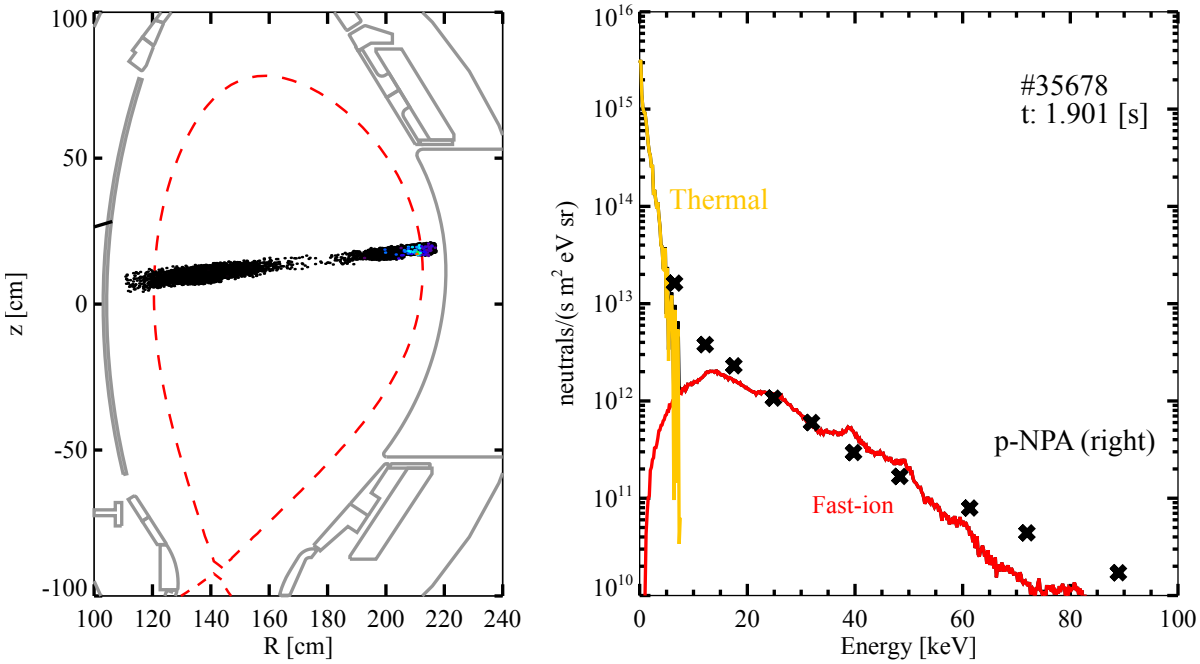

Figure 4.4: Right: Poloidal projection of FIDASIM MC markers that reach the detector. The passive NPA detects particles from as far as the high-field side. Left: The FIDASIM calculated thermal (yellow) and energetic (red) particle flux compared to measured flux by the passive NPA for an example discharge.

Chapter 5

The new edge FIDA diagnostic at ASDEX Upgrade

During this Ph.D work an edge fast-ion D-alpha (FIDA) system has been installed at ASDEX Upgrade. The system makes use of two newly designed prototype spectrometers connected to edge lines of sight. This chapter presents the installation of the edge-FIDA system. First a detailed description of the spectrometer design will be presented followed by a description of the lines of sight geometry. The calibration procedures will then be discussed and finally measurements obtained with the new edge FIDA system are presented. Parts of this chapter are published in [85].

5.1 A pair of new prototype spectrometers

A pair of spectrometers has been developed that are both able to observe red and blue shifted Balmer alpha radiation simultaneously. Moreover, the spectrometers were designed to additionally measure and resolve the unshifted D-alpha emission which was not possible with previous generations of FIDA spectrometers. Measuring the unshifted D-alpha emission is important as it provides valuable information on the background neutral density along a line of sight. In particular, when studying passive FIDA light this becomes essential. However, simultaneously measuring both, the FIDA and unshifted D-alpha contributions is challenging since their intensities can differ by several orders of magnitude (see section 5.5). Thus, a spectrometer with high dynamic range is required.

Moreover, high temporal ($<1\,\mathrm{kHz}$) and reasonable spectral resolution ($<0.2\,\mathrm{nm}$) are required. While high temporal resolution is necessary to be able to resolve edge instabilities, the spectral resolution is necessary to identify possible impurity line emissions in the spectrum and to exclude them from the analysis.

Both spectrometers follow a high photon throughput Czerny-Turner like design [86] using lenses instead of mirrors. Each consists of a movable plane holographic grating, and two lenses with an opening angle, ϕ, of 25° as illustrated in figure 5.1. The grating is mounted on a rotational stage (Newport RVS80-CC) to allow fine adjustments or modifications of

the central wavelength. The figure illustrates the working principle of the spectrometer design. At the spectrometer entrance, a bundle of vertically stacked fibres with a diameter of 400 µm each is attached. The light coming from the bundle is reduced by an entrance slit and then reaches the first lens which parallelizes the light on its path to the grating. The grating disperses the light according to wavelength in the horizontal plane. The light reaching the second objective lens is focused onto a (Princeton Instruments ProEM) camera with an electron multiplying charge-coupled device (EM-CCD) chip.

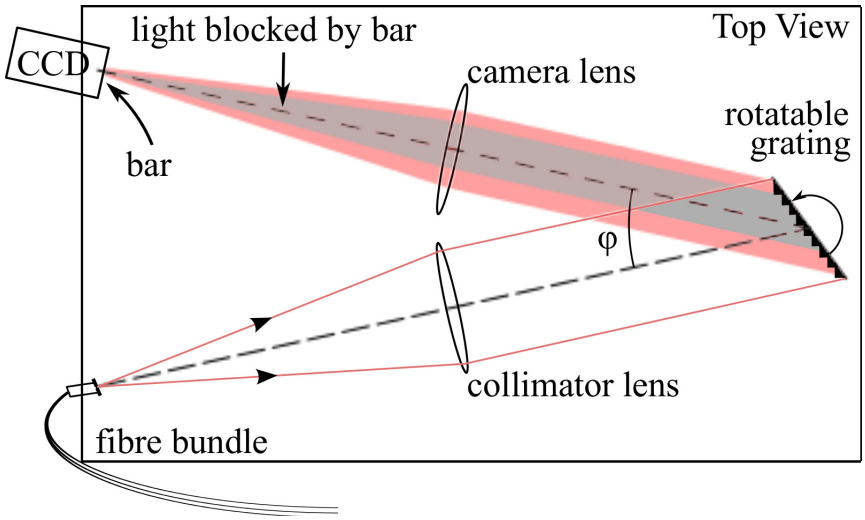

Figure 5.1: Edge FIDA spectrometer conceptual design.

The first spectrometer, which has been built during this work is depicted on the left in figure 5.2. It makes use of two Sigma EX objective lenses with focal lengths of 300 mm and f-numbers of 2.8. The gold coated grating, from Richardson Gratings, has an effective grating area of 102×102 mm with 1760 lines/mm. The light sensitive area of the EM-CCD chip is 1024×1024 pixels with a pixel size of 13 µm. The spectral width of the spectrometer measuring at 656 nm is approximately 17 nm with an average dispersion of 0.017 nm/pixel.

The second spectrometer is based on a very similar design but makes use of two single aspherical lenses (made of BK7) to reduce possible transmission losses of objective lenses consisting of 10 or more individual lenses. The aspherical lenses have focal lengths of 200 mm for light with a wavelength λ of 650 nm and f-numbers of 2. The lenses are each mounted on top of separate linear stages (Newport MFA-CC), that can move the lenses along the optical axis to be focused. Furthermore, a larger aluminium coated grating with a larger effective area of 102×128 mm and 2000 lines/mm is installed. The EM-CCD chip is smaller with a sensitive area of 512×512 pixels and a pixel size of 16 µm. The smaller detector area and lower dispersion from the grating results in a spectrum width of 11.8 nm with an average dispersion of 0.023 nm/pixel. To optimise the spectrometer for FIDA measurements, a central wavelength of 660 nm is chosen.

The high quantum efficiency of the EM-CCD chip is ideal for low light acquisition with a dynamic range of 16 bits. To reduce thermal noise (dark charge), the chip is cooled to

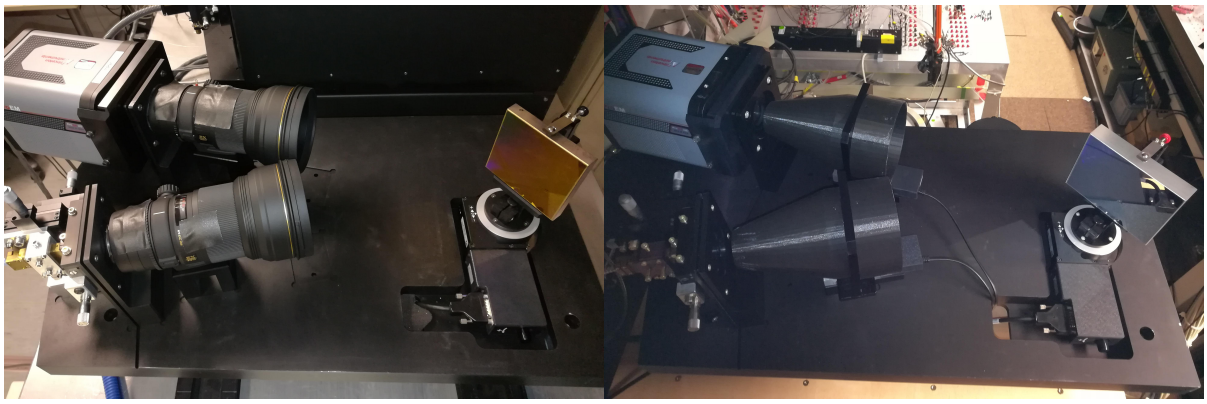

Figure 5.2: Side view of first (left) and second spectrometer (right). The first spectrometer uses Sigma EX lenses and a gold coated grating, whereas the second uses two single quartz lenses placed on linear stages as well as a larger aluminium coated grating.

−55 °C (−70 °C) with a built in Peltier cooler. Here, the value in brackets indicates the smaller camera of the second spectrometer. On-chip multiplication (gain of 20 typically selected) of the photo generated charge further reduces the readout noise.

The FIDA emission is typically a factor of 1000 smaller than the un-shifted edge emission. Observing the FIDA contributions with reasonable photon statistics is challenging since the detector would saturate at the unshifted line. Therefore, a 2 mm wide 3D printed blocking-bar is positioned in front of the CCD chip, as shown in figure 5.3.

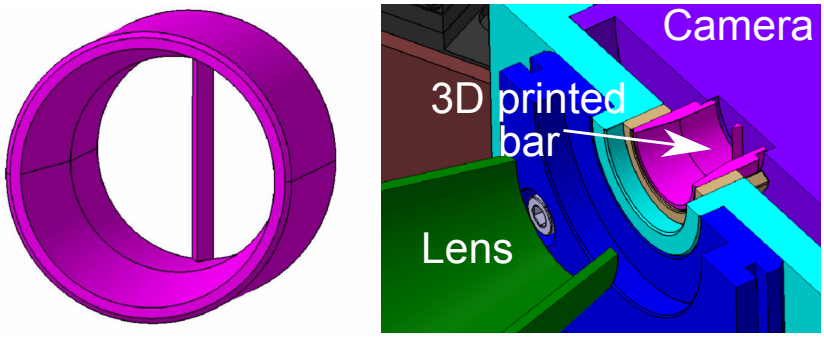

Figure 5.3: Left: CAD drawing of the 3D printed bar designed to obstruct light within a narrow wavelength band. Right: The bar is positioned directly in front of the CCD chip.

The purpose of the bar is to dim but not completely block the incident light within a narrow wavelength range. The bar is placed directly in contact with the protective glass of the camera, 8 mm in front of the chip. A triangular cross-section of the bar is chosen to provide a well defined blocking plane at the back of the bar. The bar affects the spectrum in a 6 nm wide range as can be seen from the effective transmission curve in figure 5.4, where the black curve corresponds to the first spectrometer and the red curve to the second spectrometer. The blocking width can be increased by moving the bar further from the chip, however, this also increases the transmission of the affected region.

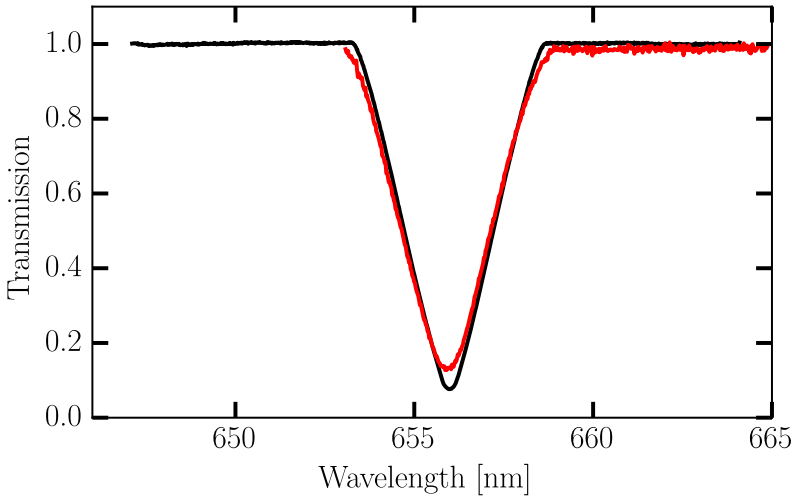

Figure 5.4: Measured transmission curves due to the blocking bar, with the black curve representing the first spectrometer and red the second spectrometer. The transmission around 656 nm is strongly reduced by the 2 mm thick bar, placed in front of the CCD chip.

The smaller spectral width of the second spectrometer required that the bar be positioned off centre, with respect to the CCD chip, to view roughly the same red shifted wavelength range as the first spectrometer. The equivalent blue shifted wavelength range, including the unshifted D-alpha emission can be viewed by rotating the blocking bar 180° in its holder and adjusting the central wavelength by rotating the grating. This was, however, not necessary since the combination of the line-of-sight geometry and fast-ion distribution functions at AUG mainly produces red-shifted FIDA light.

The spectral shape of the measured spectra can be recovered by applying the inverse of the transmission curve when applying the intensity calibration. It should be noted that the use of blocking bars using an intermediate image is commonly applied in FIDA spectroscopy systems [87, 88, 89], but these systems typically use an intermediate lens. The latter reduces the photon throughput and imagining quality such that the new approach without intermediate image provides an overall better system performance.

5.2 Edge FIDA setup

5.2.1 Lines of sight

The first spectrometer is connected to in-vessel optics from an existing edge CXRS system [45] (see figure 5.5). The optics define 22 toroidal lines of sight that cross a 60 kV, 2.5 MW heating beam (Q3) in the steep plasma gradient region. The lines of sight are tangential to the flux surfaces at their intersection with the NBI path and thereby offer high spatial

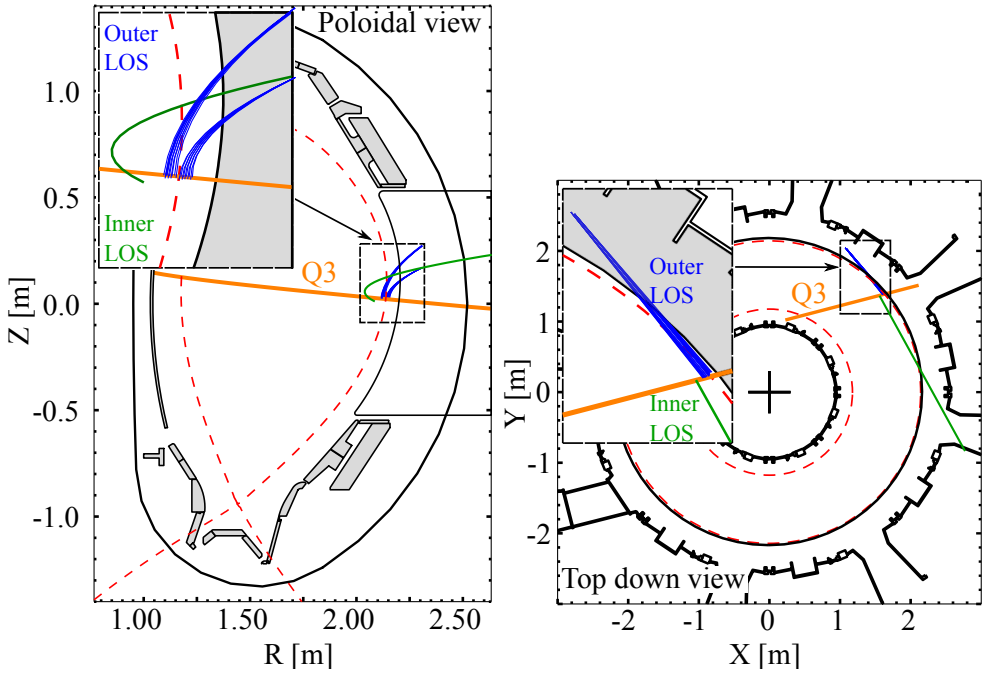

Figure 5.5: Poloidal (left) and top down (right) view of the edge lines of sight used to expand the existing ASDEX Upgrade FIDA system.

resolution.

The second spectrometer is connected to a single edge line of sight (LOS) from the core CXRS optical system [69], as indicated green in figure 5.5. The LOS crosses the same heating beam, namely Q3, near the plasma edge. The LOS has a less tangential angle with respect to the flux surfaces in the region that intersects the heating beam, as compared to the edge CXRS views. The tangency radius of the LOS is at $R = 2.04\,\mathrm{m}$, while the intersection with the beam is at $R = 2.09\,\mathrm{m}$, compared to $R = 2.12\,\mathrm{m}$ of the edge CXRS LOS with the deepest view. In the following, the innermost edge CXRS view will be referred to as outer-LOS and the LOS from the core-CXRS system will be referred to as inner LOS.

5.2.2 Radial resolution

The radial resolution of FIDA measurements has been calculated using the FIDASIM Monte Carlo code, discussed in section 4.2, which includes that neutralised fast ions might travel a short distance before emitting their characteristic D-alpha radiation. In FIDASIM, kinetic profiles and a TRANSP (see section 2.6.1) predicted fast-ion distribution function have been considered from a representative experiment. Figure 5.6 shows the positions in the poloidal plane where simulated fast ions have become neutralised, before travelling into the view of a given line of sight and contributing to the radiation collected. Here, the simulation data for the innermost (blue) and outermost (red) edge LOS, as well as the inner

LOS (green) are given. The combined NBI beam and halo neutral density is indicated by black contour lines and the separatrix is provided in red. As can be seen, the region from where information on fast-ions is obtained is localised along the LOS with an extent of about 3 cm in the radial direction for the edge views. Figure 5.6 shows the positions binned to the normalised poloidal flux coordinate, ρ_{pol}, and fitted with a Gaussian function. The average FWHM of the emission for the edge views is 0.03 in terms of ρ_{pol} or 1.5 cm when mapped onto the midplane radius. The less tangential view of the inner LOS results in a larger measurement range of 0.09 in terms of ρ_{pol} or 3.4 cm in radius.

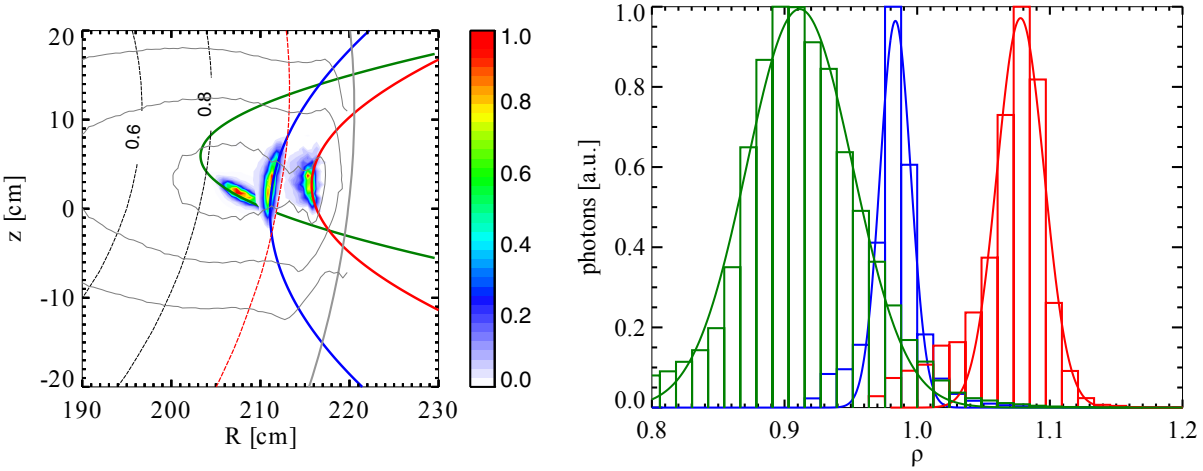

Figure 5.6: Poloidal view of active FIDA emission observed by two edge LOS calculated by FIDASIM. Active FIDA location calculated by FIDASIM mapped and binned with respect to the normalised poloidal flux coordinate. A Gaussian fit is used to describe the radial width.

5.2.3 Fast-ion velocity space sensitivity

The fast-ion velocity-space sensitivity of the edge-FIDA system is illustrated in figure 5.7 in terms of weight functions. Weight functions display the part of the velocity space that can be accessed by a given LOS in a defined wavelength range. That is to say, the weight functions show the probability for a fast ion of a certain energy and pitch range to be neutralised and to subsequently emit D-alpha radiation into a given wavelength range [8]. The weight functions have been calculated by FIDASIM and display the possible locations in velocity space of the fast ions which can emit detectable light for a given line of sight and wavelength range. As can be seen, the toroidal LOS are largely sensitive to co-rotating fast ions, for wavelengths with Doppler shifts well separated from the un-shifted Balmer alpha radiation of D at 656.1 nm. As can be seen in figure 5.5, the inner LOS is orientated in the opposing toroidal direction compared to the edge LOS. Hence the FIDA emission for the wavelength range 659.5 to 660 nm measured on the inner LOS results in roughly the same velocity space coverage as the edge views measuring from 652 to 652.5 nm.

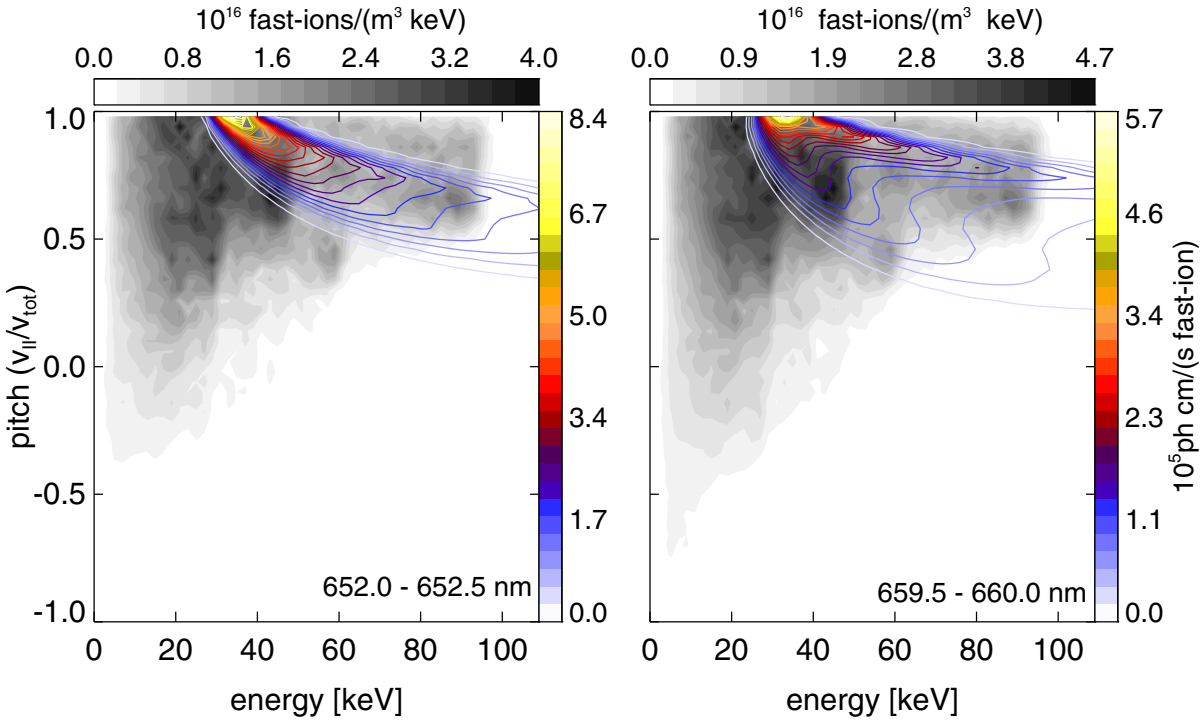

Figure 5.7: FIDA weight functions (in colour) calculated by FIDASIM for the outer (left) and inner (right) LOS. The wavelength range selected is well separated from the beam emission. The grey contours illustrate a fast-ion distribution as calculated by TRANSP for an off-axis NBI heated discharge.

5.3 High speed FIDA configuration

Two different readout options of the camera are used here. First, the frame-transfer mode, typically applied by the suite of CXRS systems [69] at ASDEX Upgrade allows for continuous imaging. The EM-CCD chip has an additional region of 1024×1037 (512×528) pixels that are covered and not illuminated, as illustrated in figure 5.8. After an exposure the photo-electrons (charge) are shifted row by row to this masked region, at a rate of 0.7 (0.3) µs per row. Once all of the charges have been shifted to this area the following exposure starts. During this time the charge in the masked region is read out by the serial registers and converted to digital signals at a rate of 20 (10) MHz. To reduce the read out time, regions of interest (ROI) covering each imaged fibre are defined serving as the spectrometer channels. During read out the charge of each channel is binned in the vertical direction allowing for faster operation. The binning of charge also increases the signal to noise ratio (SNR). The size of the camera chip can accommodate up to 21 fibres with the lowest readout time and thus exposure time of 3.1 ms. The readout time is reduced to 2.5 ms when only 10 fibres are used. The smaller chip on the second spectrometer can accommodate up to 13 fibres with the lowest readout time and thus exposure time of 1.35 ms. The significantly faster readout time of the smaller camera is due having only half the number of

pixels to read per row as well as the faster shift time of 0.3 µs per row.

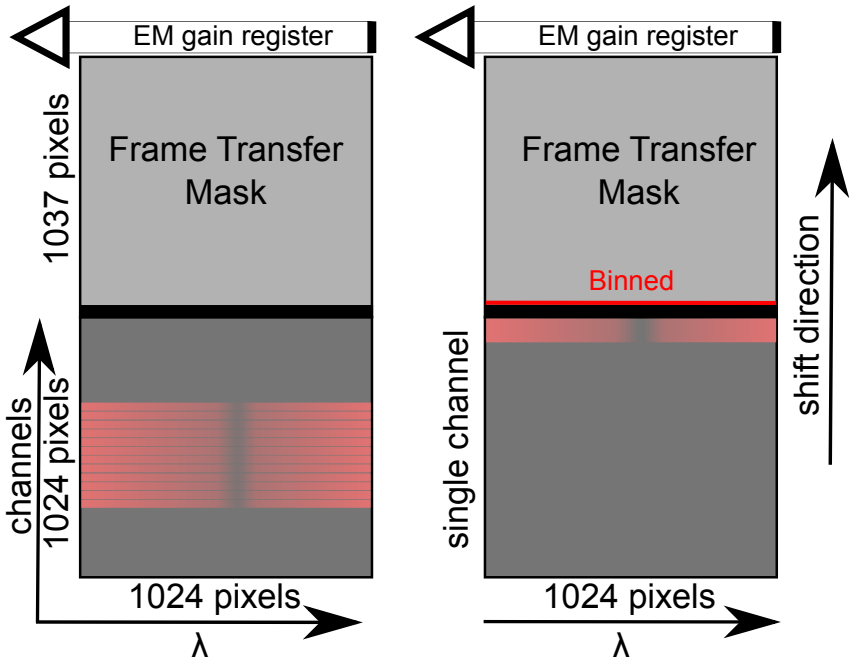

Figure 5.8: Diagram displaying the difference in configuration between the standard multi-channel "frame transfer" mode and the single channel "spectra-kinetics" mode.

Second, the spectra-kinetics mode can be used, which allows for significantly faster exposure times (down to the μs range) at the cost of having only one single channel available adjacent to the non-illuminated part of the chip. Spectra-kinetics takes advantage of the fast transfer and binning of charge to the covered part of the chip. After an exposure the charge collected in the ROI is binned and shifted to this region where it is stored in one of the 1037 (528) rows. Thus, 1037 (528) exposures can be performed continuously without the slow readout of the data. The frame rate is determined by the combined vertical shift (t_{shift}) and programmed exposure (t_{exp}) time. The shift time is determined by the size of the ROI which for 120 rows would be 84 µs. Here, we use an exposure time of 200 µs, translating into a time-window of about ($(t_{exp} + t_{shift}) \times 1037 \approx$) 300 ms. Lower exposure times (84 µs) are possible but come with reduced photon statistics, i.e. reduced SNR. The low photon integrated flux during the fast acquisitions increases the significance of readout noise. It should be noted that this noise source can be greatly reduced for the larger camera of the first spectrometer by reading out not with 20 MHz but with only 10 MHz, at the cost of a longer dead-time between bursts but with no effect on time resolution within a burst. Finally, it should be noted that, it is important that only the defined ROI is illuminated during the measurement, since the charge collected in the pixels below the ROI cannot be removed between exposures. Fibres imaged to regions not covered by the ROI are therefore unplugged and covered when the system is operated in the spectra-kinetics mode.

5.4 Calibration

5.4.1 Intensity calibration

FIDA spectroscopy relies on absolutely calibrated spectra for a quantitative interpretation. The intensity calibration of the spectrometer is performed measuring the light produced by an integrating sphere (Labsphere, Model Unisource 1200). The sphere produces a spectrum with a well known radiance. From the calibration the conversion factors from digital counts to photons, [Ph/(s sr m^2 nm)] is determined.

Correcting for camera effects such as the bias, smear and gain by electron multiplication is necessary before the calibration can be applied to the raw spectra. Several dark frames measured immediately after each discharge are used to correct for the EM-CCD charge bias. A non-illuminated channel is used to estimate the smearing in the multi-channel configuration. During spectra-kinetics operation, a separate smear channel is not possible. Instead the effective exposure time is calculated considering the additional time pixels remain exposed to light as they are shifted. This additional exposure is equal to half the width of the ROI multiplied by the shift time. The multiplication factor of the EM-gain has been characterised by detailed measurements using the integrating sphere. A non-linearity of about 1 % has been found which is corrected for using data from the EM-gain characterisation.

An absolute calibration of the spectrometer allows for a direct comparison with other spectrometers installed at ASDEX Upgrade. Figure 5.9 shows the calibration conversion factors of the new edge FIDA spectrometers in black and red compared to those of a core (COR) CXRS spectrometer[69] in blue. Here the applied gain factors have been adjusted for and the difference in slit width between the two spectrometers taken into account. The COR spectrometer is an optimised f/2.8 spectrometer, using a ProEM 512×512 pixel EM-CCD camera. As can be seen, the new prototype spectrometers show good photon throughput characteristics compared to the COR system at 650 nm, especially the second spectrometer has a photon throughput that is twice as large.

Some uncertainty in the calculated spectral intensity can arise from transmission degradation of the optics due to coating of the in-vessel objective lenses, or damage to the optical transmission fibres. In addition, uncertainty arises when switching fibres between the edge FIDA and CXRS system since the applied FC-connectors might not reproduce conditions by 100 % when disconnected and connected again.

These sources of uncertainty are difficult to quantify. One routinely applied method is to compare experimental spectra to forward modelling of the neutral beam emission as suggested by [90]. The expected emission of this contribution can be calculated using FIDASIM. Good agreement of the beam emission can be obtained for multiple channels simultaneously providing an indication of channels with unreliable fibre connections.

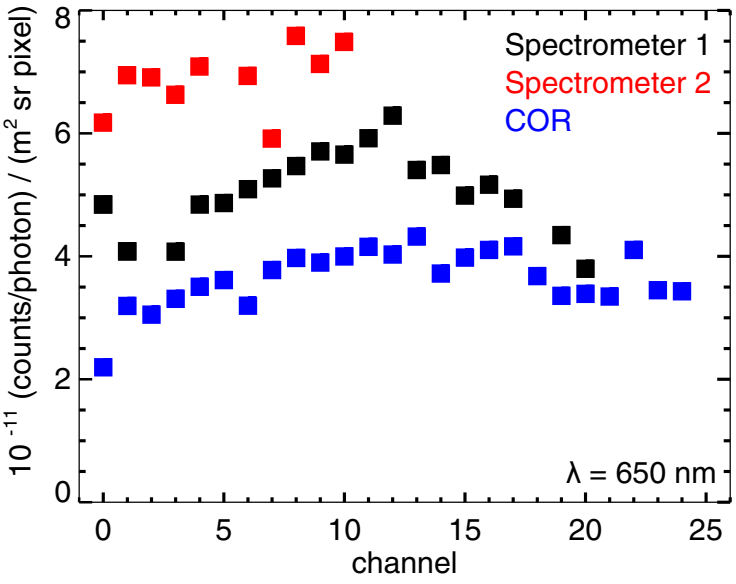

Figure 5.9: Comparison of the spectrometer calibrations for the new edge FIDA spectrometers and the 'COR' CXRS spectrometer (blue) installed at ASDEX Upgrade.

5.4.2 Wavelength calibration

An accurate wavelength calibration is performed by measuring and fitting a forward model to the emission lines from a neon lamp. Example spectra and fits are shown in figure 5.10. The wavelengths of Ne emission lines are well known and the tabulated values of the NIST database [91] are used here. The forward model fits a synthetic spectrum constructed of Gaussian functions to the Ne spectrum for each channel. The free parameters of the grating equation [92] obtained from the fit are used to calculate the wavelength axis per channel. The spectral width of emission lines determines the spectral resolution of the spectrometer and is described as an instrument function. The instrument function is modelled here by a convolution between a box function and a Gaussian curve which well recovers the spectral shape, in part determined by the wide spectrometer entrance slit (box) and by the aberrations of the lenses and the grating (Gaussian). A comparison between the measured and fitted data is shown in the right hand side graph of figure 5.10. The average instrument widths of the two spectrometers are 0.21 nm and 0.16 nm respectively.

The slight decrease in the intensity, observed by the first spectrometer, to the left of the emission lines in figure 5.10 appears to be a camera readout error associated with the sharply increased intensity. Fortunately this only affects a few pixels and is generally not observed in the wavelength ranges of interest of spectra measured during experiments. Furthermore, this effect is not observed with the camera of the second spectrometer.

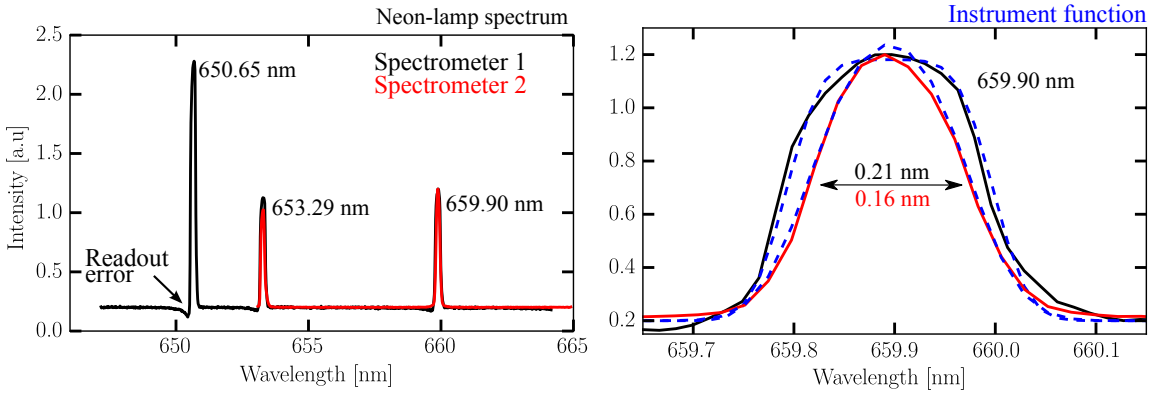

Figure 5.10: Left: Measured emission spectrum of a neon lamp used for wavelength calibration. Right: A single neon emission line demonstrating the spectral resolution with the fitted instrument functions plotted in dashed lines.

5.5 Edge FIDA Measurements

Edge FIDA measurements have been carried out with the first spectrometer connected to 10 toroidal LOS of the edge CXRS system. For those multi-channel measurements every second LOS of the edge CXRS lines is used. In this manner edge ion temperature and velocity profiles can still be obtained, which is important for the analysis. Spectra measured during a low density H-mode discharge are shown in figure 5.11. The experiment was heated continuously by two off-axis beams (Q6 and Q7) and several 50 ms long NBI phases of the active beam (Q3) were added for CXRS and FIDA measurements. The spectrum in red represents a passive spectrum (without NBI Q3), averaged over 4 sequential frames (10 ms). From short to long wavelength, the passive spectrum contains the BV and OV impurity lines followed by passive FIDA, observable from about 650 to 655 nm. The emission between about 655 and 658 nm originates from background neutrals whose density decays exponentially towards the plasma core. This so-called passive thermal CX emission is discussed in chapter 4. The emission exhibits intense and unshifted radiation from the cold edge neutrals and a broader feature from neutrals inside the last closed flux surface. The double peak observed for the unshifted D-alpha emission line appears to be a remnant of the bar shadow (see figure 5.4) which has not been calibrated out perfectly. To the right of the unshifted Balmer alpha radiation are two CII impurity lines with tabulated wavelengths of 657.805 nm and 658.288 nm (from NIST).

In addition the active+passive spectrum during operation of NBI Q3 is plotted in black. This spectrum features additional active FIDA radiation, the beam emission (BES) as well as the thermal charge exchange (or halo) component. Finally, a synthetic spectrum from FIDASIM is plotted against the measured spectra, with the sum of all contributions indicated by a brown dashed curve. The calculated emission indicates that the passive FIDA contribution (in magenta) is comparable in magnitude to the active contribution (in green). This shows that background subtraction or detailed modelling of the passive

radiation is required when trying to interpret active FIDA signals.

The lack of red shifted FIDA emission in the spectrum can be attributed to the predominantly co-passing fast-ion content generated by the off axis beams as illustrated in figure 5.7.

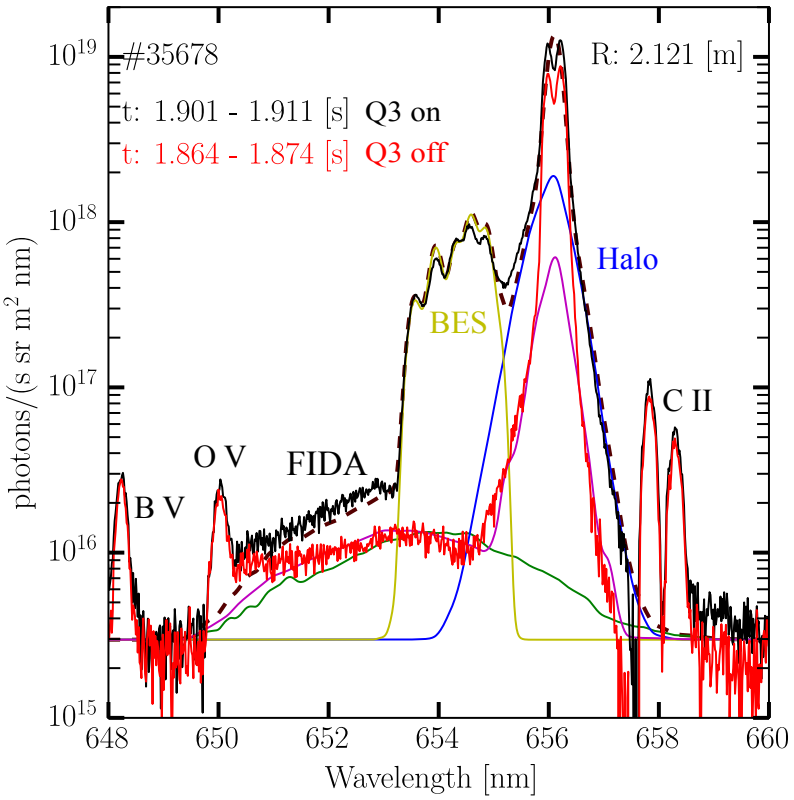

Figure 5.11: Active (black) and passive (red) edge spectra measured during a discharge with 2.5 MW of off-axis NBI heating. The active (green) and passive (magenta) FIDA contributions calculated by FIDASIM are over plotted with the sum of all contributions indicated by a brown dashed curve. The magenta line also includes the thermal CX contribution.

By integrating the spectra in wavelength for each LOS, radial profiles can be studied. Figure 5.12 compares synthetic profiles from FIDASIM with the measurements. Here, both the synthetic and experimental spectra have been integrated between 651 nm and 652.5 nm. As can be seen, the experimental data tends to be higher than the prediction. This might be explained by the assumption of an exponential decay of the fast-ion density outside the LCFS which has been made, since TRANSP does not calculate fast-ion densities for this region.

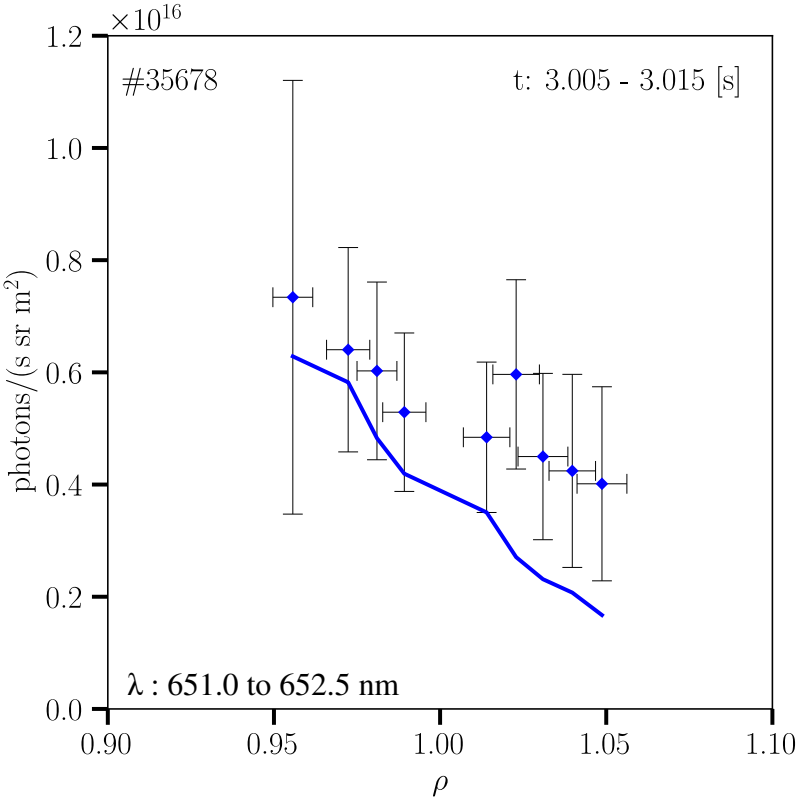

Figure 5.12: Profile of active FIDA emission integrated over the indicated wavelength range of the spectra measured by the edge FIDA system using the first spectrometer. The solid line represents the profile obtained from FIDASIM calculated spectra.

5.6 Fast edge FIDA measurements

Edge FIDA measurements with exposure times of 200 µs have been performed at ASDEX Upgrade making use of the spectra-kinetics readout mode. Figure 5.13 demonstrates how the new high speed edge-FIDA installation reveals dynamics of the full D-alpha spectrum not resolvable on the standard FIDA diagnostic of ASDEX Upgrade. The graph on the left shows a spectrum measured for the outermost LOS of the standard FIDA system in black. The spectrum is obtained from a single frame with an exposure time of 5 ms. The spectrum over plotted in red is obtained from a single frame measured by the second spectrometer, with an exposure time of 200 µs. The shorter exposure time results in a larger amount of photon noise as compared to the standard FIDA system. However, not only is the full spectrum obtained for the inner LOS, where the un-shifted emission of the standard FIDA system has been completely blocked out, but also transient phenomena are captured not clearly observable on the standard system as seen in the time traces plotted on the right in figure 5.13. The time trace of the passive FIDA emission measured for the inner LOS

shows a sharp, short lived, increase at the ELM crash, before decreasing. The effect of ELMs on the FIDA emission are discussed further in chapter 7.

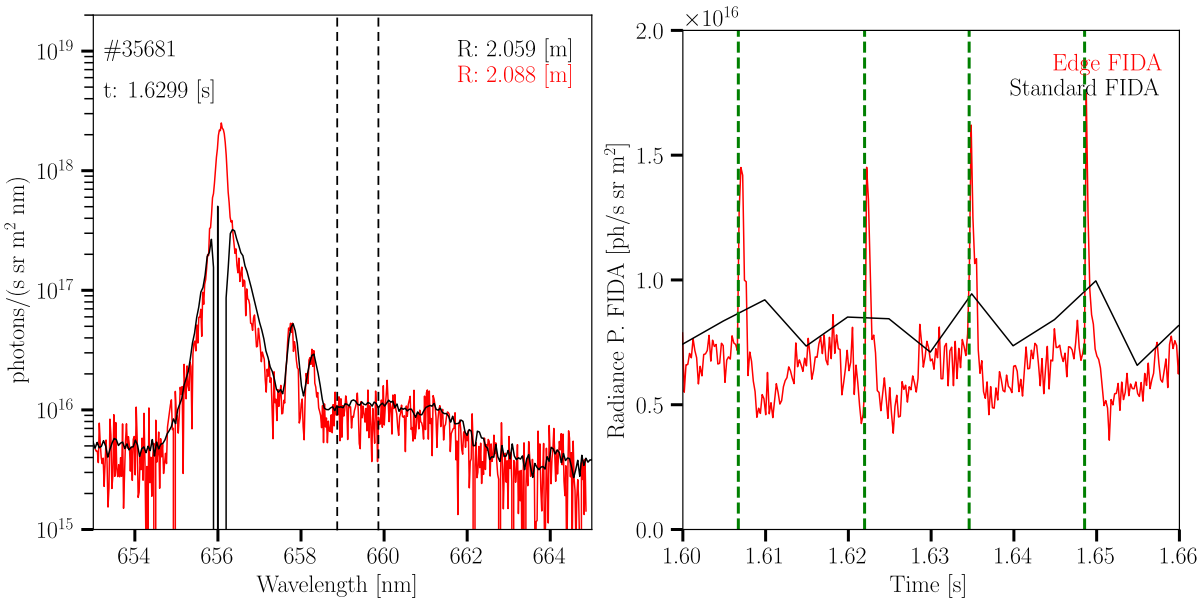

Figure 5.13: Left: Passive spectrum measured for the inner LOS (red) compared to spectrum from the standard FIDA system measuring on an adjacent LOS (black). Right: Passive FIDA time traces for the same discharge in figure 7.4, for the emission integrated between the black vertical dashed lines.

Chapter 6

Analysis of passive FIDA light

The interpretation of FIDA spectra requires a careful treatment of passive FIDA light. This can be achieved by subtracting passive spectra obtained either from reference views or from passive spectra that are measured in phases when the active beam is briefly turned off. At AUG the latter is applied as reference views are not available. However, such background subtraction can only be applied when plasma conditions are constant. In the presence of ELMs for instance, the plasma parameters are changing too quickly such that background subtraction is not applicable. To get ELM-resolved data using background subtraction, the NBI would need to be modulated at about 1 kHz or faster which is beyond the capability of ASDEX Upgrade. Therefore, this work focuses on the interpretation of passive FIDA light rather than avoiding it. Forward modelling of the passive emission is applied which not only allows to assess theoretical fast-ion distributions, albeit with coarser spatial resolution compared to active emission, but also extracts information on the background neutral density. The latter is important not only for passive FIDA measurements but also to determine the level of CX-losses which affect the fast-ion calculations of the slowing down distribution.

This chapter focuses on the methodology developed for the analysis of passive FIDA emission at AUG. Modelling of the background neutral density is presented first, followed by a procedure developed to constrain the neutral density to experimental measurements. The modelling of theoretical fast-ion distributions by TRANSP is discussed, with an emphasis on addressing CX losses. Finally the forward modelling of synthetic passive FIDA spectra by FIDASIM is presented.

6.1 Determination of the neutral density

6.1.1 Discharge overview

To demonstrate the analysis methodology, discharges #35419 and #35678 are used as examples. The discharges were performed with a toroidal magnetic field B_T of $-2.5\,\mathrm{T}$ and plasma current I_p of $0.6\,\mathrm{MA}$. $5\,\mathrm{MW}$ of continuous NBI heating by the off-axis beams Q6

and Q7 was applied, additionally 50 ms beam blips of beam Q3 every 500 ms to measure CXRS and active FIDA. Additionally 2 MW of central ECRH heating was applied to avoid tungsten accumulation.

Figure 6.1 shows the time traces of the electron temperature, density and plasma heating power for a time window of 400 ms for each discharge. During this time window the density and temperature remained relatively constant, with the core density values for both discharges around $5 \times 10^{19}\,\mathrm{m}^{-3}$. The edge density of #35419, however, was slightly lower at $3.5 \times 10^{19}\,\mathrm{m}^{-3}$ compared to $4 \times 10^{19}\,\mathrm{m}^{-3}$ for #35678. This in turn yielded a higher edge-electron temperature as the same level of heating power was applied. Additionally the core electron temperature was also lower for #35678 at 3.5 keV compared to 4.2 keV for #35419. The stable plasma conditions are useful for the analyses as it allows the data acquired during the time window to be combined for an improved statistical interpretation with reduced measurement uncertainties.

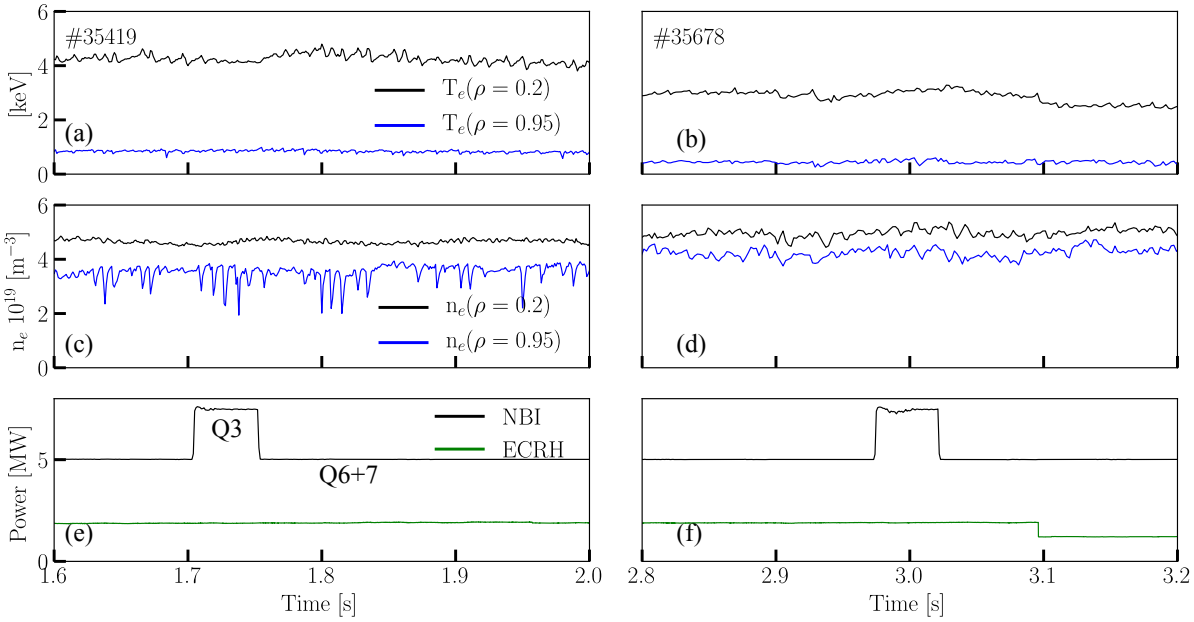

Figure 6.1: Time traces of (a,b) electron temperature, (c,d) density and (e,f) heating power for discharges #35419 and #35678 over a 400 ms interval.

Figure 6.2 shows the fitted plasma kinetic profiles for #35678 based on data from various diagnostics. The data for the electron density and temperature have been filtered to only include measurements between 3.5 and 1.5 ms before ELMs. The points in green are profiles obtained from the standard Bayesian forward modelling technique at AUG that includes measurements of the interferometry and Thomson scattering systems for the electron density and measurements by electron cyclotron emission and Thomson scattering systems for the electron temperature. The forward model, however, does not yet use data from the newly developed He-beam diagnostics which features SOL data with low uncertainties. We therefore perform a TANH fit ([93]) of the electron density to include

the data of the He beam in the analysis. Similarly the ion temperature measured by the CXRS systems during the beam blip is fitted with a TANH function. Here it is assumed that the 50 ms beam blip does not significantly increase the plasma temperature, justified by the time traces of the electron temperature in figure 6.1c and d. In case of the electron temperature profile, the IDA analysis agrees very well with the Helium beam data. An additional TANH-fit has therefore not been applied, but an average of the profiles within the given time interval.

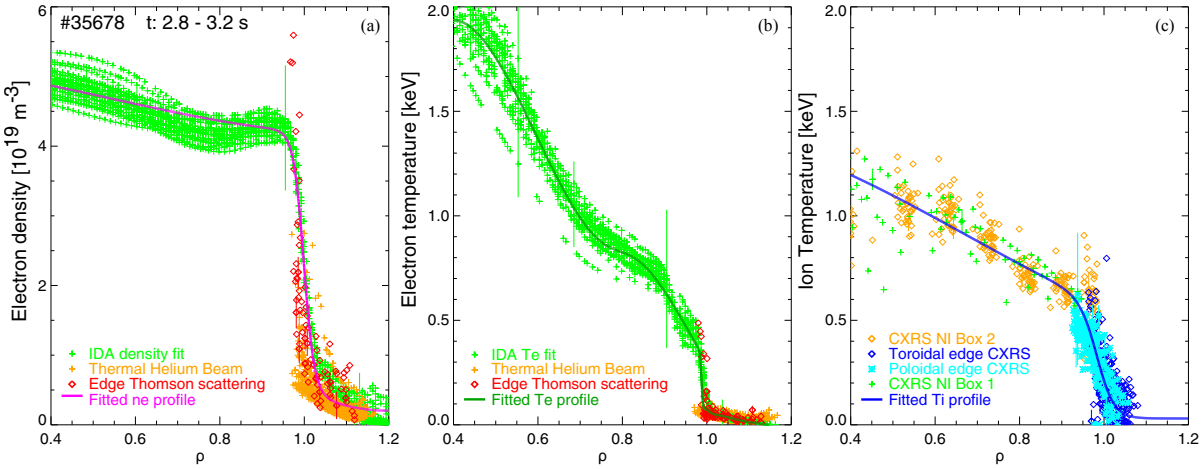

Figure 6.2: Kinetic profiles of the (a) electron density, (b) electron temperature and (c) ion temperature obtained for discharge #35678 by fitting data from multiple diagnostic systems.

6.1.2 Neutral modelling with KN1D

With the plasma kinetic profiles at hand the neutral density is determined through modelling using the KN1D neutral transport code as discussed in 2.4. To simulate the neutral density across the full profile KN1D has been updated with new cross-sections within the framework of this thesis.

KN1D makes use of the reaction rates compiled by [94] for electron impact ionisation and recombination. However, the tabulated atomic ionisation rate in particular was only available up to 706 eV, which in this case would be around ρ =0.8. Therefore cross-sections from FIDASIM have been taken to extend the simulation range to higher temperatures, or deeper into the plasma.

Figure 6.3 shows the neutral density calculated for discharge #35678, using the profiles from figure 6.2 and the D_2 pressure as measured by the AUG manometer plotted in red in figure 3.4. Starting from the wall the neutral density shows a moderate increase in the far SOL from $4.5 \times 10^{15}\,\mathrm{m}^{-3}$ to a maximum of $5.6 \times 10^{15}\,\mathrm{m}^{-3}$ due to strong dissociation of D_2 in this region. The density thereafter starts to decrease and rapidly falls by an order of

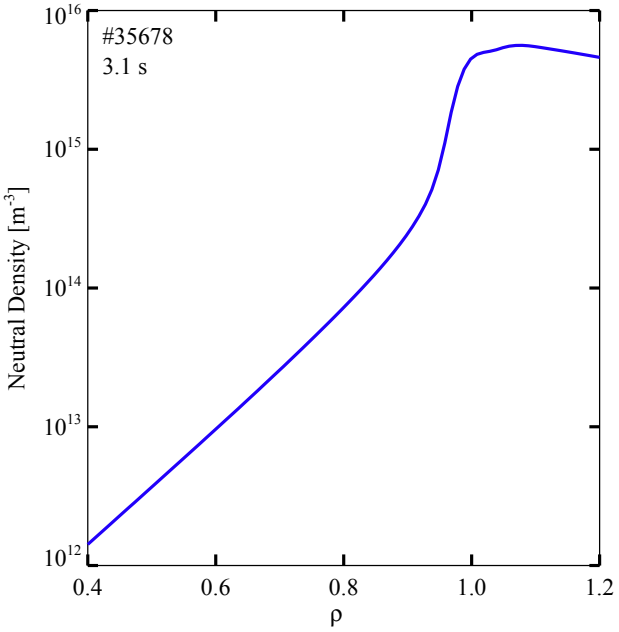

Figure 6.3: KN1D calculated neutral density profile for discharge #35678 at 3.1 s.

magnitude between the separatrix and the position of the pedestal top. The attenuation of the neutral density beyond the pedestal top follows an exponential decay to the core.

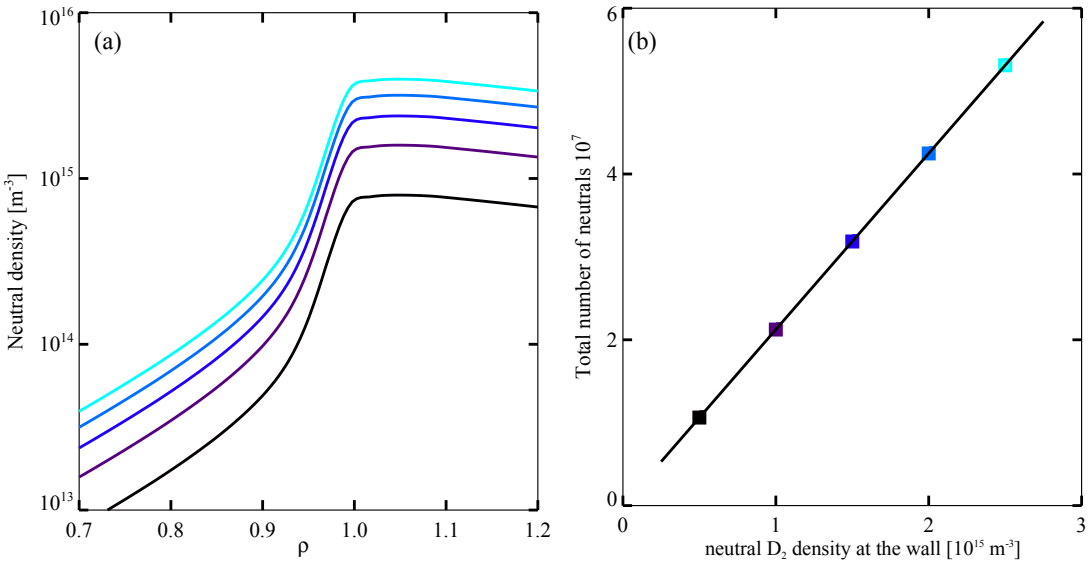

Figure 6.4: (a) KN1D calculated neutral density profiles for linearly increasing $p_{\mathrm{n,wall}}$. (b) Profile integrated number of neutrals versus neutral density at the wall. A linear fit is over plotted in black.

To determine the sensitivity of the calculated neutral density profile on the different inputs, a scan of the input parameters is demonstrated here. Firstly the input neutral pressure at the wall $p_{\mathrm{n,wall}}$ is varied for several KN1D runs from 0.5 to 2.5 times the reference pressure of 0.64 mPa. The resulting density from KN1D is found to depend linearly on the input pressure at the wall, as shown in figure 6.4. This is expected as neutral-neutral collisions or a local depletion of ions are not considered in KN1D. As can be seen in the graph an increasing $p_{\mathrm{n,wall}}$ results in an overall increase in the neutral density profile, without an accompanying change in the profile shape. This is further illustrated in the graph on the right, where the profile integrated number of neutrals is plotted against the neutral density at the wall. A linear fit to the points is plotted with a solid black line and accurately describes the trend observed. The linear response, therefore, effectively allows the $p_{\mathrm{n,wall}}$ to be treated as a free parameter in KN1D.

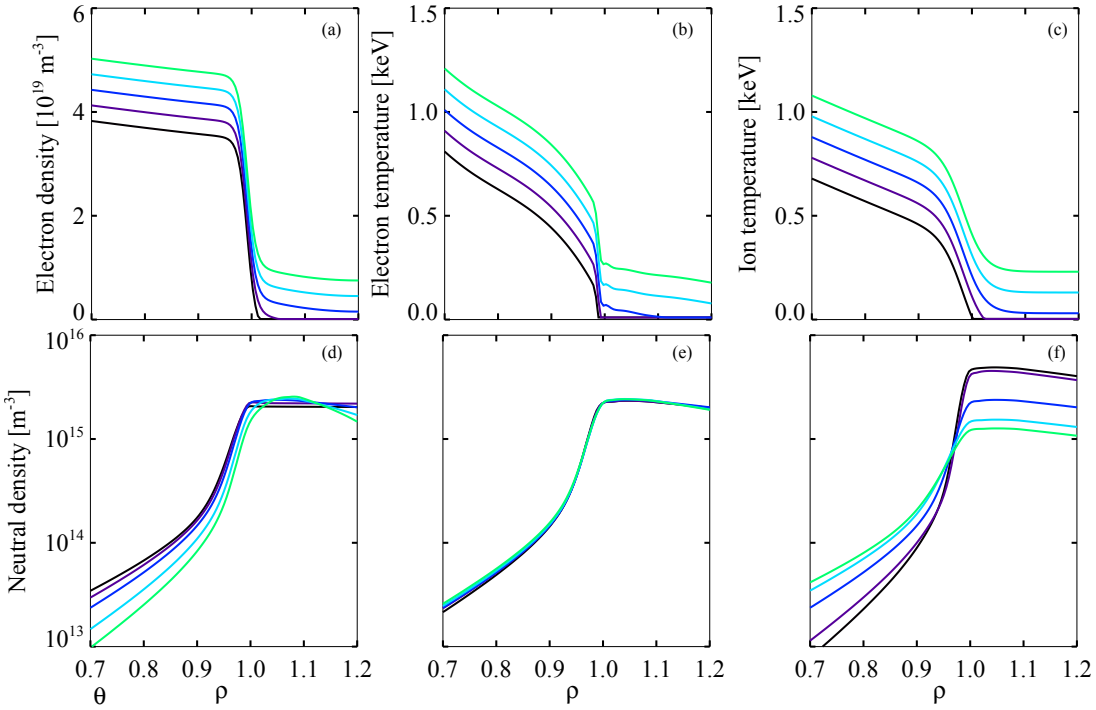

Figure 6.5: Scan of the (a) electron density, (b) electron temperature and (c) ion temperature profiles. (d-f) The corresponding neutral density profiles calculated by KN1D.

To determine the effect of the plasma profiles on the calculated neutral density, test profiles were constructed as shown in the top row of figure 6.5. The test profiles were varied by adding different offset levels with the electron density increased in steps of $3 \times 10^{18}\,\mathrm{m}^{-3}$ and the temperature in steps of 100 eV. The bottom row in figure 6.5 shows the corresponding neutral density profiles using the same colour code. As can be seen the neutral density profile is most sensitive to the input electron density and ion temperature profiles.

The neutral density profiles in the bottom left graph of figure 6.5 shows that an increase in the electron density results in an increased atomic neutral density near the wall,

explained by more molecular dissociation events. In addition, a more rapid attenuation is observed towards the plasma centre. The electron temperature on the other hand is found to have little effect on the neutral density profiles, since the cross-section for electron impact ionisation is typically much smaller than that of ion-impact ionisation. The ion temperature is observed to strongly influence the neutral density profile. An increase of the ion temperature leads to lower SOL and higher core neutral densities. This can be understood considering that the neutrals that undergo CX experience an increase in transport, as neutrals born by CX reactions are faster and can therefore penetrate deeper into the plasma. While high SOL ion temperature values are unlikely in steady state conditions, they can occur during transient events.

The sensitivity of the neutral density profile to the edge conditions requires that the uncertainties of the kinetic profiles are as low as possible.

6.1.3 Comparing the neutral density against CX measurements

Passive thermal D-alpha emission

In order to determine how well the modelled neutral density profile describes the experimental conditions, FIDASIM has been expanded during this work to forward model the passive thermal CX emission, as described in chapter 4. This allows us to assess the neutral density profile based on the measured thermal emission.

As an example, figure 6.6a shows two neutral density profiles from KN1D calculated for the discharge #35678, making use of the profiles presented in figure 6.2. The magenta curve represents the neutral density profile calculated with the measured $p_{\mathrm{n,wall}}$, and the green curve calculated assuming a pressure level that is twice as high. The plot on the right shows the spectrum measured by the inner LOS of the edge FIDA system for the corresponding time point. The thermal CX emission extends from roughly λ =655 to 657 nm. The intense central emission peak is the unshifted emission from cold recycling neutrals, and is not modelled here because this would require a 3D wall source, not implemented in FIDASIM.

The coloured curves represent the corresponding thermal CX spectra calculated by FIDASIM for the neutral density profiles of the two different edge pressures. The synthetic spectrum has been folded with the instrument function of the spectrometer. The CX emission in magenta clearly underestimates the experimentally measured intensity, while the synthetic spectrum in green matches the data reasonably well. Note here that passive FIDA radiation is present in the measurement that has not been modelled (see discrepancy below 655 nm), but the presence of passive FIDA radiation hardly affects the analysis of the thermal emission. The thermal emission is almost two orders of magnitude larger than the FIDA component (see the semi-logarithmic scale in figure 6.6b) such that its impact is below 1 % despite looking significant due to the log-scale in the plot. The good match with the simulation in green shows that the neutral density is, indeed, twice as high as expected based on the pressure gauge data.

This discrepancy might be in part due to the large toroidal spatial separation between the manometer and the LOS. While the LOS are in sector 15 with vessel structures close

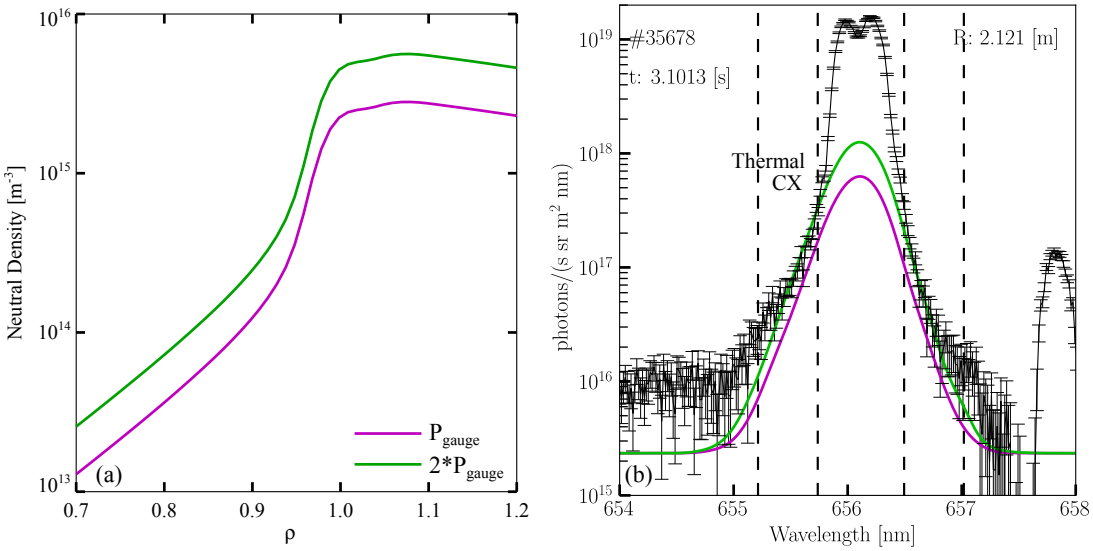

Figure 6.6: (a) KN1D calculated neutral profiles for discharge #35678 at t =3.1 s. (b) Forward modelled thermal CX emission (in colour) compared to the measured edge Balmer spectrum in black.

to the plasma, the manometer is placed in sector 2 inside an open port. Therefore this study will use neutral density profiles from KN1D that are scaled based on measurements of the thermal emission.

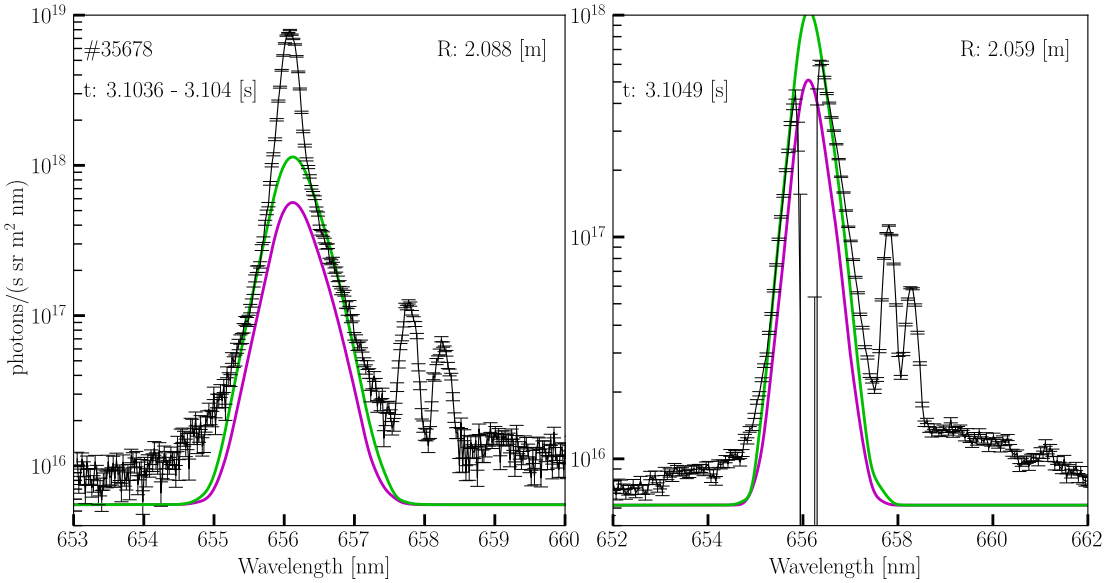

Figure 6.7: Left: Forward modelled thermal CX emission compared to measured spectrum along inner view. Right: Forward modelled thermal CX compared to measured spectrum of the standard FIDA system.

In addition, data from several LOS can be used to validate the neutral density profile from KN1D. Figure 6.7 shows the emission measured additionally with the inner LOS as well as the edge LOS of the standard FIDA system. This additional match between the forward modelled and both experimental spectra demonstrates that the neutral density profile shape from KN1D is representative of the experimental conditions.

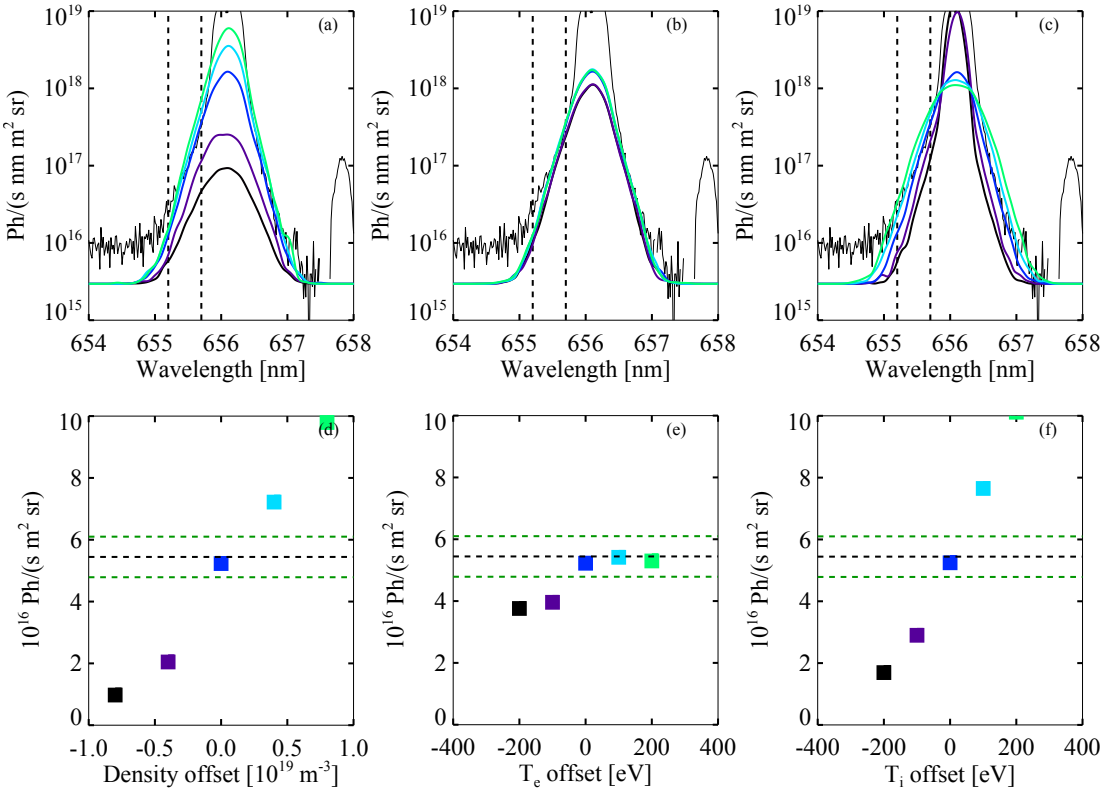

Figure 6.8: Forward modelled thermal CX emission for: n_e (a), T_e (b) and T_i (c) profiles of figure 6.5. (d-f) Comparison of integrated emission with the measured spectrum, represented by the horizontal dashed line. The green dashed lines indicate the uncertainty range.

To understand the sensitivity of the calculated thermal CX emission to uncertainties in the input kinetic profiles, a sensitivity study has been performed. Figure 6.8 shows the forward modelled thermal CX emission for the different profiles, as presented in figure 6.5, while the neutral density profile has been kept constant. Again the modelled results are most sensitive to modifications of the electron density and ion temperature profiles, while insensitive to changes of the electron temperature profile.

The modelled emission is observed to increase for larger electron densities and thus, larger ion densities. This can be explained by more ion impact excitation and charge-exchange processes, populating the emitting n=3 atomic state. The insensitivity of the modelled spectra to the electron temperature can be understood based on a similar argument. The contribution by electron impact excitation is insignificant and hence modifying

the electron temperature does not impact the modelled thermal emission. Modifications to the ion temperature lead to changes in the spectral shape of the modelled emission, and to the intensity in the wavelength range of interest. The former effect can be understood from the increased Doppler broadening due to the larger temperatures. The increased emission can be understood from the energy dependence of the CX cross-section from the ground state to the n=3 state. This cross-section strongly increases with energy until about 20 keV. The sensitivity of the thermal CX spectral shape and intensity, especially on the ion temperature offers a means to gauge the reasonableness of the fitted profiles.

Passive thermal NPA flux

The method based on the thermal emission described above allows to assess the validity of a predicted neutral density profile from KN1D. In addition, this approach can be benchmarked using a technique developed in [95] that allows to directly calculate the background neutral density from the passive thermal flux of neutrals as measured by neutral particle analysers (NPA). The calculation requires the plasma kinetic profiles as input, as well as the NPA LOS geometry and the energy resolved absolute flux of thermal particles.

The technique works by calculating the neutral particle emissivity along the LOS, for a given energy channel. The calculation is performed using the CR model of FIDASIM which models the attenuation of neutrals in a 3D grid. For NPA detectors, a single LOS is sufficient for constructing a neutral density profile, due to the good energy resolution of the diagnostic. Assuming a monotonically increasing temperature profile from the edge to the plasma core, a given energy range can be attributed to a radial region in the plasma. Particles from the core for instance will be more energetic than those from the edge.

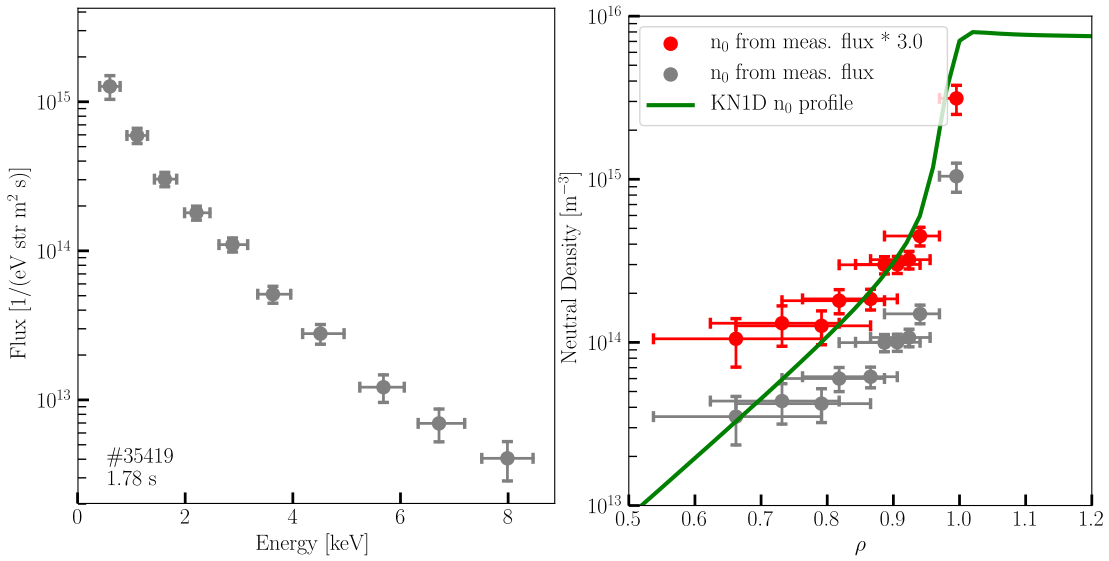

Figure 6.9: Left: Thermal particle flux measured by the AUG passive NPA system. Right: Neutral density as calculated from the measured flux.

Figure 6.9 demonstrates the technique applied to the discharge #35419. The left plot shows the measured thermal particle flux multiplied with a factor three discussed shortly.

The plot on the right presents the calculated neutral density points for the corresponding fluxes. The curve in green represents the KN1D neutral profile that best matches the thermal CX emission.

The comparison with the KN1D neutral profile shows a good qualitative agreement in the profile shape. There is, however, a mismatch found in the absolute density when comparing the NPA results with the profiles from KN1D that have been scaled to match the thermal emission. Here a factor of 3 increase in the thermal flux best matches the KN1D profile. It is interesting to note that the NPA is also in front of a similar open port like the pressure gauge used. The large uncertainty associated with toroidal asymmetry of the background neutral density means the correction factors are reasonably similar. Additionally, it should be noted that the NPA was not calibrated again since its installation 20 years ago and a degradation of the detectors is expected. Nevertheless the good qualitative agreement indicates the modelled profiles are representative of the experimental conditions.

6.2 Fast-ion modelling considering CX losses

Forward modelling of the passive FIDA emission requires a theoretical fast-ion distribution function as input. Several codes exist that predict fast-ion slowing down distribution functions such as TRANSP or LOCUST. For this work neoclassical slowing down distribution functions of beam injected ions were obtained through TRANSP modelling. The advantage of using TRANSP is that it is well benchmarked against multiple devices worldwide. It is also able to model fast-ion CX reactions with background neutrals. In fact, TRANSP has its own module to calculate 1D neutral density profiles called FRANTIC.

Naturally it is desirable to perform TRANSP simulations with neutral background density profiles provided as input. However, as TRANSP calculates the neutral density in a self consistent manner one has only indirect control of the neutral density profile, as discussed in section 2.6. For this work a constant deuterium recycling flux is provided which is adjusted over several TRANSP simulations, until a good match between the FRANTIC and the experimentally tested KN1D profiles is obtained. Several options exist in the name list of TRANSP to modify and control the shape of the neutral density profile. It was found that setting the energy of recycling neutrals entering the plasma to 100 eV and the fraction of escaping neutrals to return as warm neutrals to 0, produced similar profile shapes to KN1D. Lastly the option to include volume recombination was included, however this contribution is essentially negligible.

Figure 6.10 shows the neutral density profiles calculated by FRANTIC for three different TRANSP simulations of discharge #35419 at 1.78 s. The simulations in red and magenta represent a high and low background neutral density respectively. The profile in green represents the simulation that best matches the KN1D neutral profile plotted in black. Here the FRANTIC SOL density is set to the KN1D neutral density value at the edge. The percentages in the figure indicate the portion of heating power calculated to be lost through CX reactions for the corresponding neutral densities. As can be seen, the level of CX losses can reach almost 10 % for AUG.

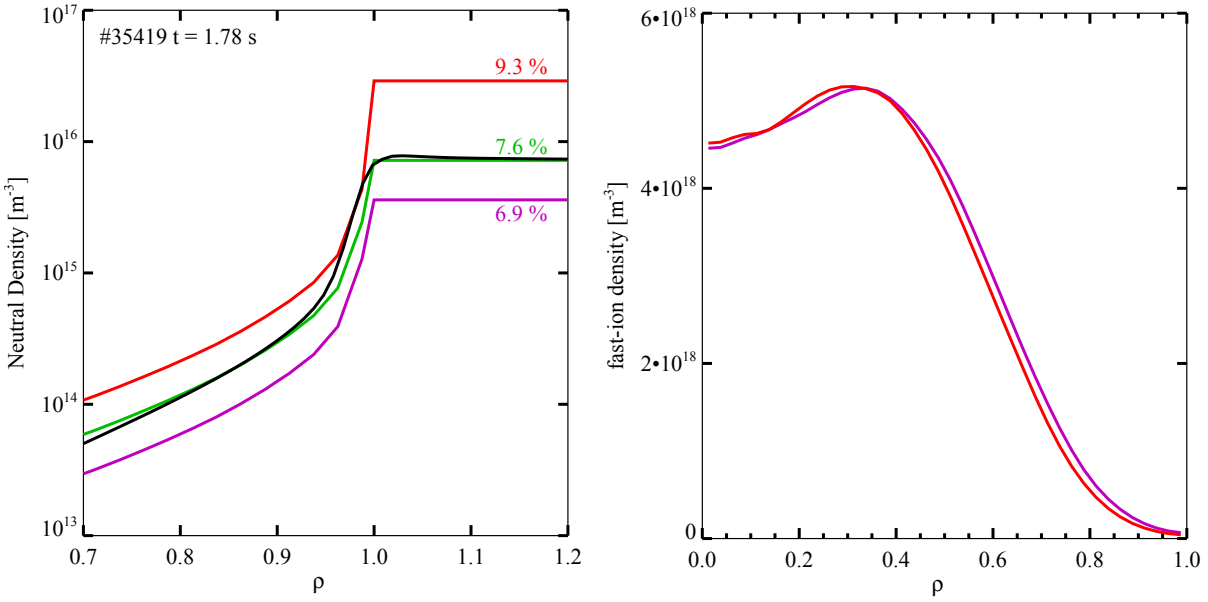

Figure 6.10: (Left) FRANTIC background neutral densities,in colour, for several TRANSP simulations of discharge #35419, compared to the KN1D profile in black. The numbers represent the fraction of heating power lost to CX reactions. (Right) The NUBEAM calculated fast-ion density profiles for the corresponding cases.

The graph on the right of figure 6.10 presents the corresponding fast-ion density profiles calculated by the NUBEAM module, integrated in energy and pitch. The high neutral density case, in red, shows a clear reduction in the edge fast-ion density. The reduction in the edge fast-ion density can be attributed to the increased CX reaction rate due to the higher density of neutrals. CX reactions hence serve as a loss mechanism at the edge. Furthermore a minor increase in core fast-ion density is observed for the high neutral density case, which can be understood by considering that a fraction of the neutralised fast-particles will travel inwards and be re-ionised. The increase in the core fast-ion density can, therefore, be explained by the increased flux of edge neutralised fast particles.

6.3 Passive FIDA modelling

Using the NUBEAM calculated fast-ion distribution the passive FIDA emission can be modelled with FIDASIM. However, NUBEAM does not store the density and distribution of particles for the SOL. Although the fast-ion density is low in the SOL, the large SOL neutral density means that a significant fraction of the passive FIDA emission originates from the SOL. Therefore, simulations by the 3D fast-ion orbit following code LOCUST have been performed to determine the expected SOL fast-ion density.

Figure 6.11 shows a comparison between the outboard midplane, energy-pitch integrated fast-ion density profiles calculated by LOCUST and TRANSP for discharge #35678

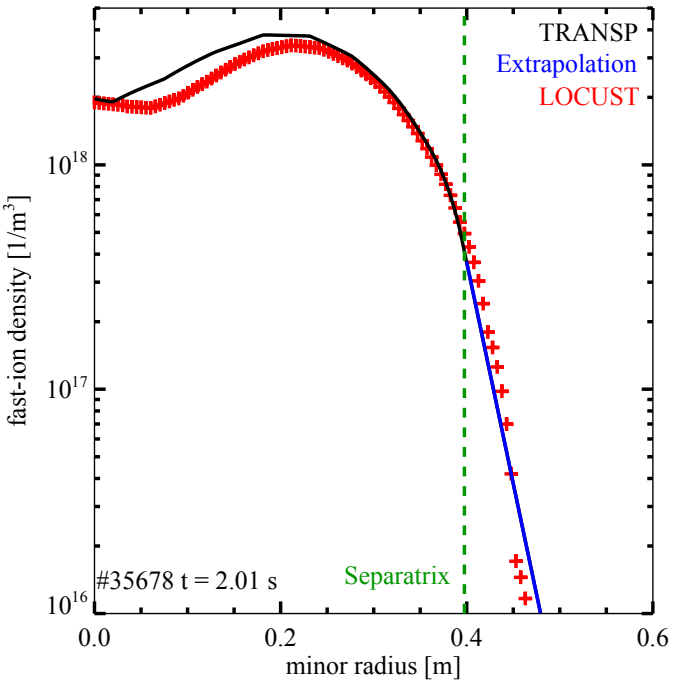

Figure 6.11: A comparison between TRANSP and LOCUST fast ion density profile integrated over energy and pitch along the outboard midplane.

at 2.01 s. An exponential extrapolation has been applied to the TRANSP fast-ion density. As can be seen the density matches well at the separatrix, with the LOCUST density profile slightly larger but close to that of the extrapolated profile in the SOL. The difference is expected as LOCUST does not include for CX reactions, as opposed to TRANSP which takes CX losses into account and is therefore used instead. The extrapolation of the TRANSP density in the SOL matches qualitatively the LOCUST density. Therefore an exponential decay is assumed in FIDASIM modelling given a TRANSP fast-ion distribution. The extrapolation is performed over the 2D poloidal plane, with the decay length determined by fitting an exponential decay of the last two radial points inside the separatrix. The fast-ion energy-pitch distribution is, however, not extrapolated and is assumed to be equivalent to the edge distribution.

Figure 6.12(a) shows the velocity space distribution of fast ions in the SOL, 1 cm outside the separatrix, at the outboard midplane calculated by LOCUST. The distribution clearly shows peaks at the full (90 keV), half (45 keV) and third (30 keV) components of the beam injection energy. The particles here are largely co-passing with little pitch angle scattering due to the low plasma density at the edge. As an extrapolation of the NUBEAM distribution is not performed, the plot on the right represents the distribution calculated at the separatrix. The NUBEAM distribution has a similar pitch distribution, but the energy peaks are less pronounced. Note the statistical noise in the NUBEAM run.

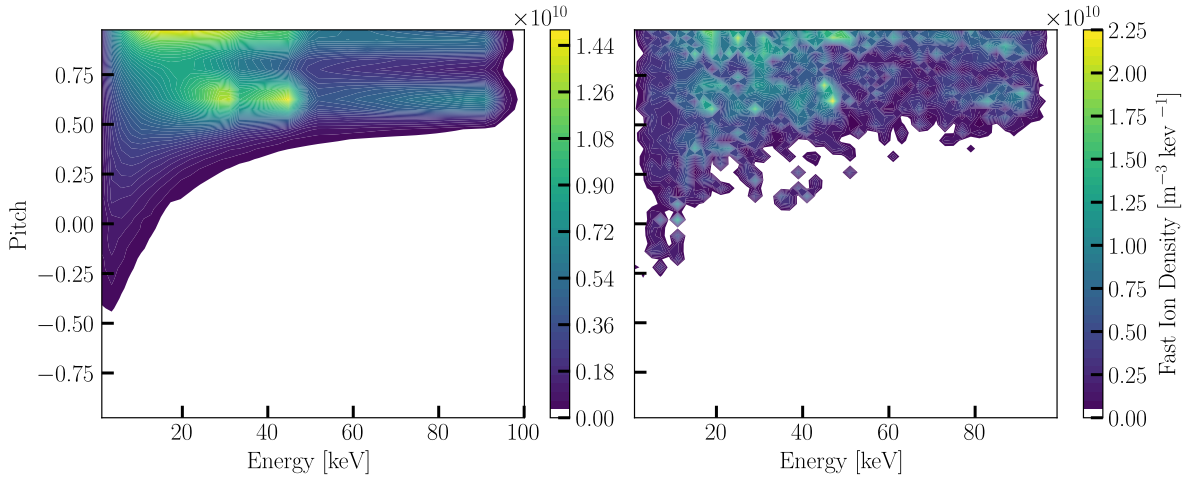

Figure 6.12: A comparison between LOCUST (left) and TRANSP (right) calculated fast-ion velocity space at the outboard midplane for#35678 at 2.01 s

Finally with the theoretical fast-ion distribution extended to the SOL the passive FIDA emission is calculated using FIDASIM. Given that the background neutral density is constrained against the thermal particle emission and flux, as discussed in the previous sections, the theoretical fast-ion distribution can be evaluated against the measured spectra. Figure 6.13 presents the forward modelled passive emission, in magenta, for the measured spectra presented in figures 6.6 and 6.7. The synthetic spectrum includes both the passive FIDA and thermal emission contributions, and shows a good absolute agreement with the measured spectrum.

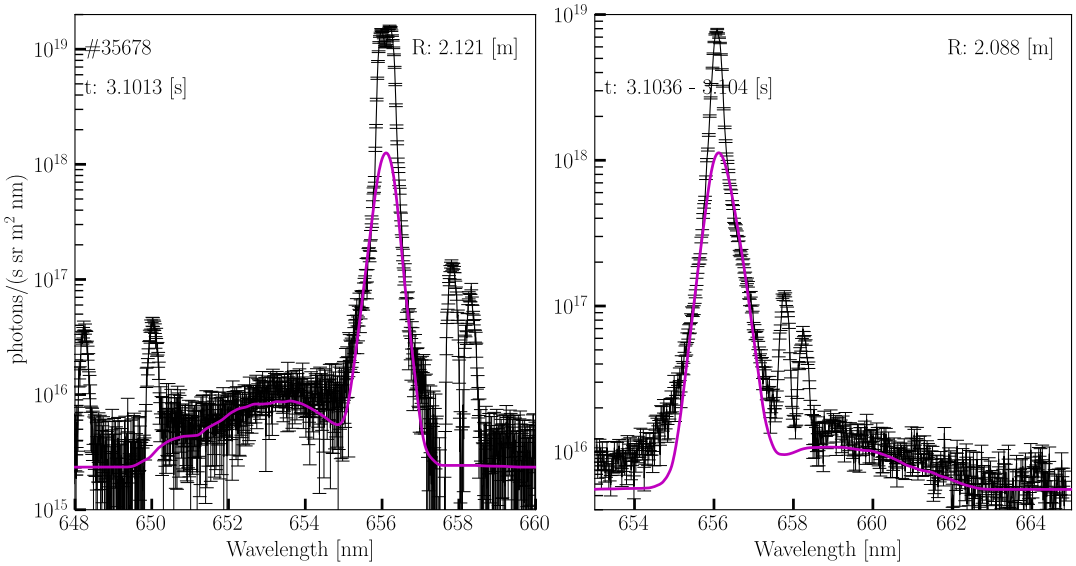

Figure 6.13: Synthetic passive FIDA and thermal CX spectra (magenta) compared to measured spectra (black) along the outer (left) and inner (right) LOS.

The methodology presented here allows to forward model the passive CX contributions to the Balmer spectra in a self consistent manner. This allows to assess theoretical fast-ion distribution, whilst also extracting information on the background neutral density. As an outlook modelling of the unshifted D-alpha emission can be included in the forward modelling.

Chapter 7

ELM induced fast-ion transport

The new edge FIDA diagnostic installed at AUG and described in chapter 5 allows to obtain information on the density and distribution of confined fast ions close to the plasma boundary. This opens the possibility to investigate the effect that edge phenomena have on fast-ion confinement. One phenomenon of interest is the fast-ion transport induced by ELMs. ELMs have been found to cause increased fast-ion losses as measured by FILDs at AUG [13, 47], but the absolute quantity of fast ions lost during an ELM crash could not be addressed, yet. However, such measurements, as well as studies of the radial extent of ELM-induced modifications could provide important information for the development and benchmark of theories that describe the non-linear dynamics of ELMs and their impact on fusion devices' first wall.

This chapter presents the first results on the ELM-induced fast-ion redistribution, as obtained from the analysis of passive FIDA emission. First, the overview of a representative experiment is presented, then forward modelling results of pre and post-ELM cases are discussed. Possible changes to the background neutral density due to ELMs are addressed followed by systematic modelling of the post-ELM passive FIDA spectra. Results on the absolute quantity and radial extent that ELMs influence fast ions are finally presented and compared to theoretical predictions.

7.1 Experimental overview

7.1.1 Discharge overview

To investigate the impact of ELMs on the fast-ion content, a low density H-mode discharge was performed (#35681) with with a toroidal magnetic field B_T of $-2.5\,T$ and plasma current I_p of $0.6\,MA$. In addition to $2.5\,MW$ of central ECRH heating, $5\,MW$ of off-axis NBI heating was applied to obtain a large fast-ion population at the plasma edge and thus maximise the FIDA emission in the ELM affected region. Additionally blips of beam Q3 were performed, in $500\,ms$ intervals, for active FIDA and CXRS measurements.

Fig. 7.1 shows several time traces for a time window, from 1 5 to $2.2\,s$, during which the

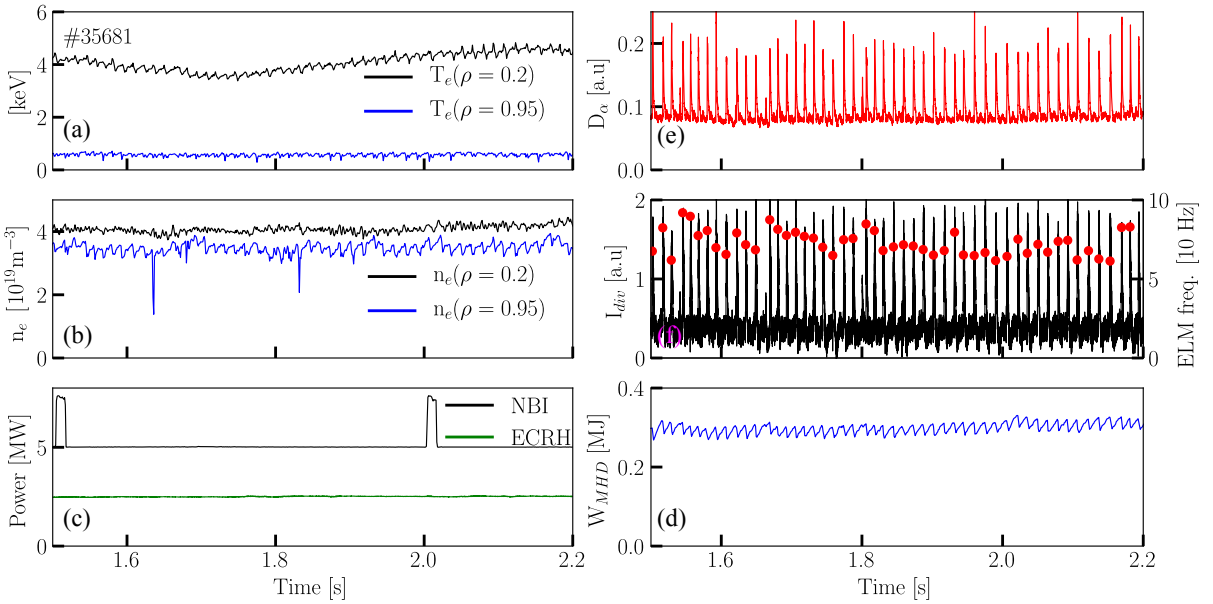

Figure 7.1: Time traces of the (a) electron temperature, (b) electron density and (c) heating power for discharge #35681 for the time window from 1.5 to 2.2 s. The right column shows the time traces of the (d) D-alpha emission, (e) divertor shunt current (in black) and (f) plasma store energy for the corresponding time. The ELM frequency is plotted in red in (f).

discharge exhibited quasi regular ELMs. As can be seen from fig. 7.1b the core (in black) and edge electron density (in blue) remain relatively constant at around $4 \times 10^{19}\,\mathrm{m}^{-3}$ and $3.5 \times 10^{19}\,\mathrm{m}^{-3}$, respectively. The periodic drops in the edge density are linked to ELM crashes. A similar effect is also seen on the measured edge electron temperature plotted in fig. 7.1a. The core electron temperature shows a slow moderate evolution during the time window.

Fig. 7.1e shows data from a D-alpha emission diagnostic that monitors the outer divertor target using photo-diodes. The ELM crashes become apparent by spikes in the signal since particles flushed out by the ELMs will stream down to the target plates and thereby enhance the local radiation. Data from a second ELM monitor is plotted in fig. 7.1f (in black) namely the outer divertor shunt current, I_{div}. Similarly, the I_{div} signal increases sharply following an ELM crash due to the increase in the currents flowing onto the divertor [96]. The start time of ELM crashes are defined with the onset of the rise of the I_{div} signal. It should be noted here that this corresponds to the time that thermal plasma expelled by the ELM reaches the divertor. This combined with the 3D structure of the ELM may result in an offset in the ELM start time observed by diagnostics at different positions. The ELM frequency is observed to range between 60 and 90 Hz. This frequency range is relatively low for AUG and therefore makes this time window ideal for analysis. Furthermore the plasma is in steady state during the roughly 50 ELMs inside the displayed time range such that the data can be synchronised with respect to the ELM onset times.

Fig. 7.1d, shows the plasma stored energy as calculated from the CLISTE equilibrium reconstruction. A clear reduction in the plasma stored energy is seen following the ELM crashes, which on average expel about 12 % of the plasma stored energy. Lastly, an MHD stability analysis indicates that the experimental pedestal pressure and current are close to the peeling ballooning boundary, identifying the ELMs as type I ELMs.

7.1.2 Mode activity

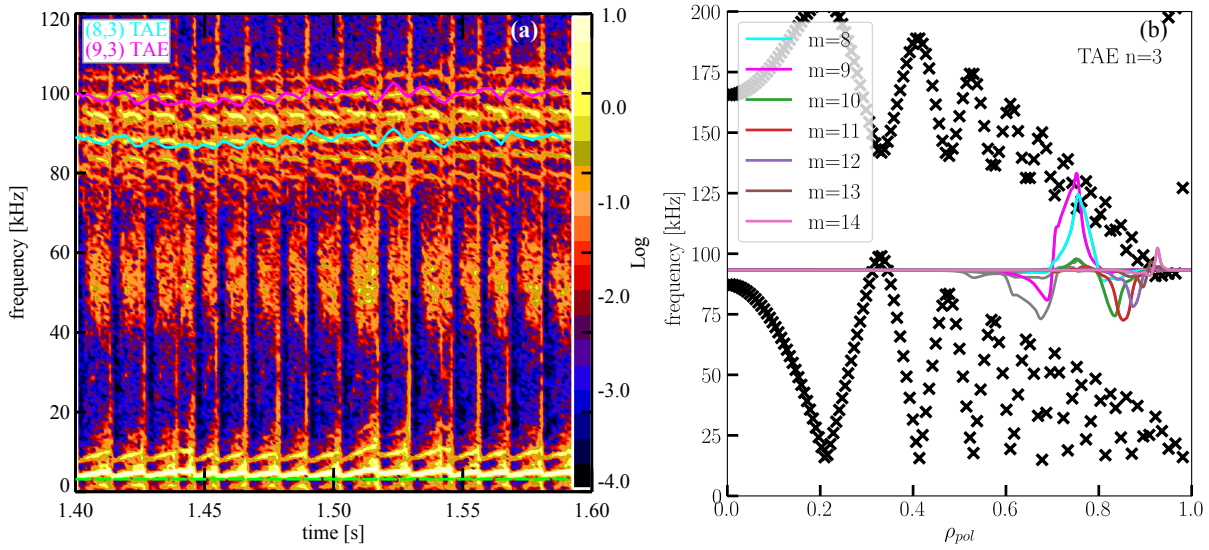

Figure 7.2: Left: A spectrogram of a magnetic pickup coil signal over plotted with the frequencies calculated for m=8 (cyan) and 9 (magenta) TAE's and a (3,1) NTM (green). Right: Dispersion relation for n=3 Alfvén modes calculated using the MHD code LIGKA. The coloured lines represents the amplitude of several poloidal mode numbers for a n=3 TAE.

It should be noted that the time window was not MHD quiescent. Figure 7.2a shows a spectrogram of the signal measured by a magnetic pickup coil. The signal produced by the coil is proportional to the rate of change of the radial magnetic field component, $\frac{dB_r}{dt}$, and shows multiple coherent frequency structures corresponding to various MHD modes. A high frequency band of modes between 80 and 100 kHz are observed as well as a lower frequency mode at around 5 kHz. The low frequency mode is found to be a (m=3,n=1) NTM situated at ρ_{pol} ~0.7. The mode numbers have been identified from a cross-phase analysis of signals from sets of toroidally and poloidally separated magnetic pick up coils. The radial location is determined from the position of the resonant flux surface, i.e the $q = \frac{m}{n}$ =3 flux surface. The toroidal rotation frequency at the q=3 position, as measured by the CXRS system, multiplied by the toroidal mode number produces a good match to the observed frequency, providing further confirmation of the mode identity. It should be noted that coherent frequency structure around 10 kHz is simply a numerical artefact of

the Fourier transform, as it coincides with the second harmonic of the real NTM frequency.

The high frequency band, on the other hand, corresponds to Alfvén eigenmodes driven by the gradient in the fast-ion density. LIGKA [97] simulations have been performed, supplied with the kinetic profiles and information on the equilibrium to characterise the mode structure and location. The LIGKA calculated Alfvén continuum are plotted in black crosses in Fig. 7.2b along with the global TAE mode structure of the least damped mode in the TAE gap for the experimentally determined toroidal mode number (n=3). The dominant poloidal mode structures are found to be m=8 and 9. A time trace of the frequency corresponding to the given mode numbers matches the measured frequency well.

Note that although both NTMs and Alfvén eigenmodes are known to interact resonantly with fast ions [98], the modes are located further inside of the plasma than probed by the edge FIDA system. Moreover, only the presence of many overlapping modes is likely to redistribute fast ions significantly [99]. The presence of a single TAE might hardly affect the fast-ion confinement.

7.1.3 Passive FIDA measurements

For this experiment the edge FIDA system was configured with both spectrometers measuring in burst mode with an exposure time of 200 µs. Measurements were performed with the system connected to the inner and outer LOS as discussed in chapter 5.

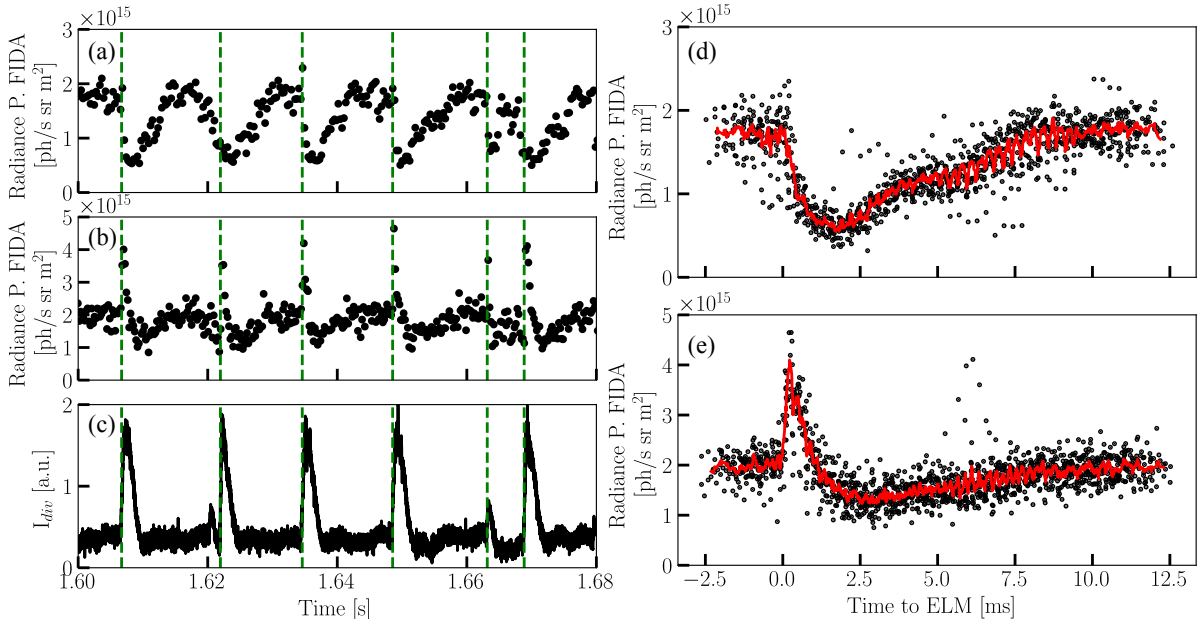

Figure 7.3: Time traces of the (a) passive FIDA radiance for the outer and (b) inner LOS and (c) divertor shunt current. The vertical green lines mark the start of ELM crashes. ELM synchronised data points of the passive FIDA radiance for the (d) outer and (e) inner LOS. The solid red line represents the rolling average for a ten point data window.

Figure 7.3 shows the time traces of the passive FIDA emission measured for the outer and inner LOS. Here the Bremsstrahlung emission has been subtracted from the emission traces, which is observed to be affected by ELMs as discussed later. The vertical green dashed lines mark the onset of ELM crashes which is determined from the outer divertor shunt current signal plotted in fig. 7.3c. The plots in figs. 7.3d and e present the passive FIDA emission synchronised with respect to the ELM onset times. The temporal reordering is done such that 0 ms represents the ELM onset. Positive values indicate time points after the ELM crash, and negative values time points before the ELM crash. The rolling mean plotted in solid red illustrates the data trend.

The presence of ELMs is observed to have a strong modulating effect on the passive FIDA emission for both views. The emission measured along the edge LOS decreases immediately following a crash and reaches a minimum on average after around 1.5 ms at about 35 % of the pre-ELM emission intensity as seen in figure 7.3d. The emission thereafter increases and recovers to pre-ELM levels around 8 ms after the crash and well before the onset of the following ELM. The inner LOS on the other hand shows, in figure 7.3e, a sharp initial increase in the emission to more than twice the pre-ELM intensity and peaks at around 250 µs after the ELM crash. The emission thereafter decreases strongly, reaching a minimum around 2.5 ms after the crash at about 65 % of the pre-ELM emission intensity. The emission thereafter recovers to pre-ELM levels on a similar time scale to that of the outer view.

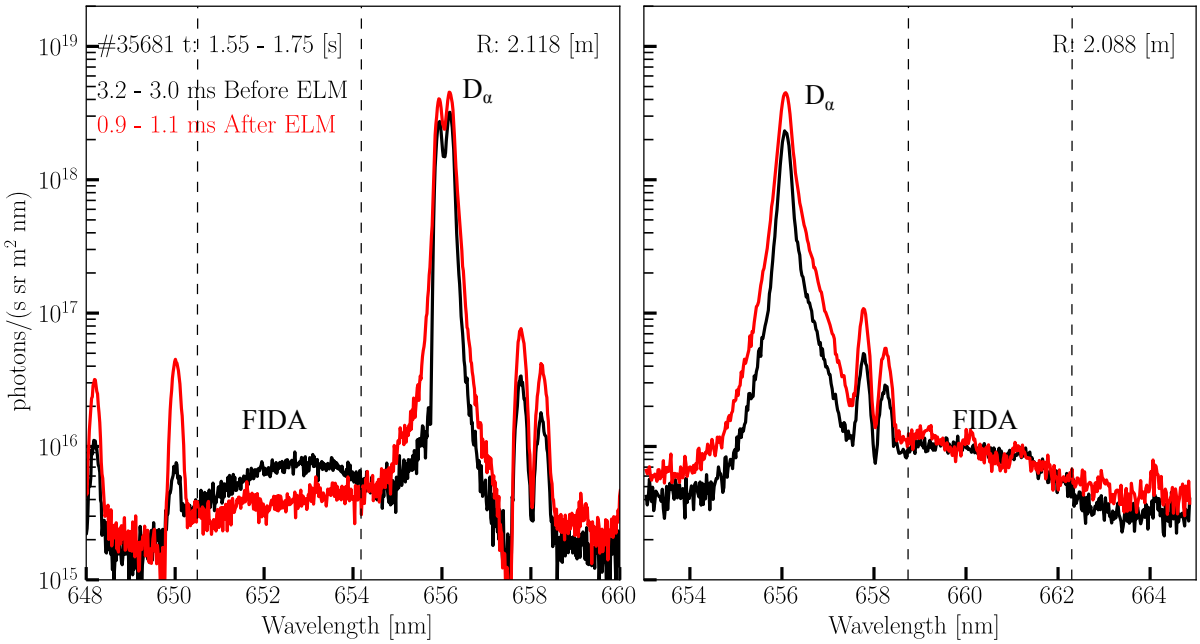

Figure 7.4: Conditionally averaged pre- and post ELM passive spectra, in red and black respectively, measured by the new edge FIDA spectrometers using the "spectra-kinetics" mode. The graph on the left corresponds to the outer LOS and the right to inner LOS.

Figure 7.4 compares the pre and post-ELM, conditionally averaged spectra of the mea-

surements presented in figure 7.3. The black spectrum is the average of frames −3.2 to −3.0 ms relative to the synchronised ELM crash (t_{ELM}= 0 s), while the red spectrum is the averaged spectrum of frames measured 1.3 to 1.5 ms after the ELM crash. A clear reduction and flattening of the passive FIDA spectrum (from about 651 to 654 nm) is observed for the outer view, accompanied by increased unshifted D-alpha emission. The inner view shows a similar increase in the unshifted D-alpha emission, however, the passive FIDA emission (from about 659 to 652 nm) observed between 0.9 to 1.1 ms after the ELM crash is close to the pre-ELM passive FIDA intensity. This indicates a strong impact of ELMs on the edge fast-ion distribution function along the LOS, however forward modelling is required for a quantitative evaluation.

7.1.4 Line emission and Bremsstrahlung measurements

The unshifted D-alpha emission measured along the outer LOS, plotted in figure 7.5a, is observed to strongly increase with each ELM crash. The trend is similar for the inner view (not plotted) and to that of the D-alpha emission measured by the divertor diode array in figure 7.1e. Similarly the impurity emission is observed to increase strongly during the ELM cycle, as shown in figure 7.5b. Additionally the Bremsstrahlung emission plotted in figure 7.5c shows a modest increase after the ELM crash.

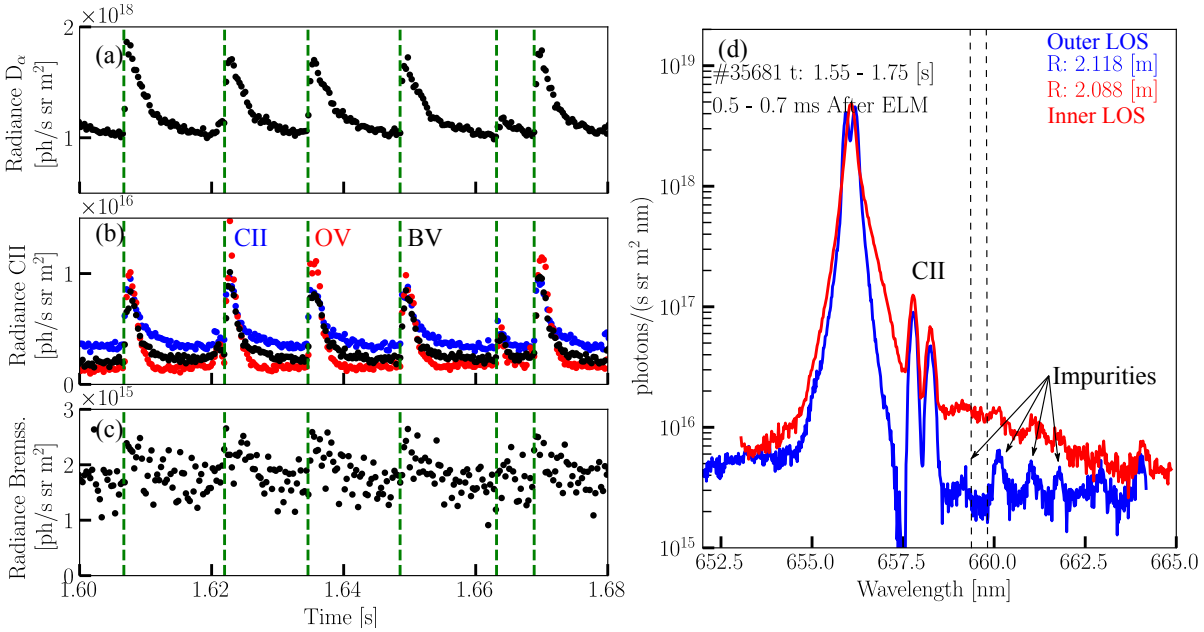

Figure 7.5: Time traces of the (a) unshifted D-alpha, (b) CII (blue), OV (red), BV (black) emission lines and the (c) visible Bremsstrahlung radiance for the same time window of figure 7.3. (d) The post ELM conditionally averaged spectra of the outer (blue) and inner (red) LOS.

Given that the impurity emission is observed to strongly increase due to ELMs, the

passive FIDA wavelength range must be carefully selected so as not to contain impurity contributions that would compromise the interpretation. Figure 7.5d shows the full, conditionally averaged spectra for the inner and outer LOS 0.6 ms after an ELM. The geometry of the outer LOS, along with the largely co-passing fast-ion distribution, results in the wavelengths above 659 nm being free of FIDA emission. Up to 5 impurity lines are exposed in the post ELM spectrum for the wavelength range extending up to 653 nm. Carbon and aluminium emission lines have been reported for this wavelength range by [8] in AUG. These lines are visible on the inner LOS post ELM spectrum. The region between 659.4 and 659.7 nm falls between two impurity lines and is therefore used for the time traces of the inner LOS in figure 7.3b and e and other comparison against the experimental spectra.

7.1.5 Comparison with NPA measurements

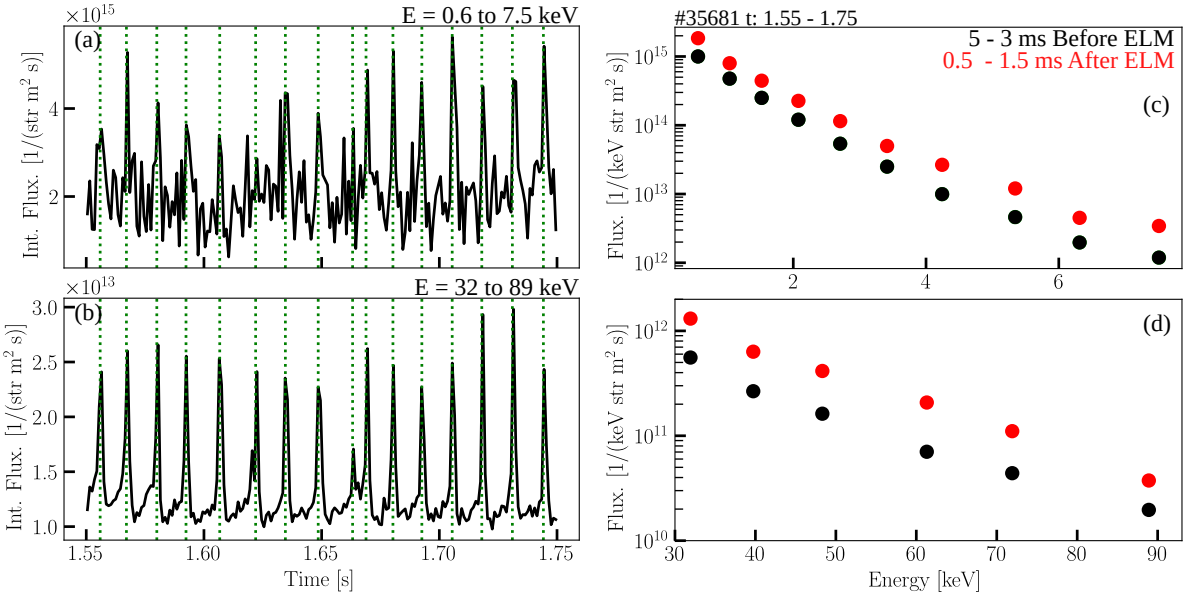

Figure 7.6: Time traces of energy integrated (a) thermal and (b) energetic neutral particle flux measured by NPA detectors. Conditionally averaged pre- and post-ELM energy resolved (c) thermal and (d) energetic particle flux for corresponding time window.

Figure 7.6 presents the passive NPA measurements for the time window 1.5 to 1.75 s. The time traces of both the energy integrated thermal and energetic particle fluxes show an increase following ELM crashes. The energetic particle flux in particular shows a consistent increase of more than twice the pre-ELM flux. It should be noted that the integration time of the NPA detectors was set to 1 ms which could explain the increase in particular of the energetic flux observed before the ELM onset. The conditionally averaged pre and post-ELM, energy resolved fluxes are shown in the right column of figure 7.6. The post ELM energetic particle flux does not appear to have a strong energy dependence. As the change in flux depends on both the background neutral and charged particle densities an increase

in flux would result from an increase in either quantities. The simultaneous increase in flux over the full energy range points to a common underlying mechanism namely an increase in the background neutral density. However, once again forward modelling is required for a quantitative interpretation of the data which will be presented in section 7.2.2.

7.1.6 Comparison with FILD measurements

ELM resolved FILD measurements are not available for the analysed discharge. However such measurements are available for a discharge (#36498) with the same experimental parameters (heating scheme, I_p, B_t), similar plasma conditions and in particular ELM properties. High speed passive FIDA measurements were performed for the discharge measuring on the outer LOS, however not for the inner LOS.

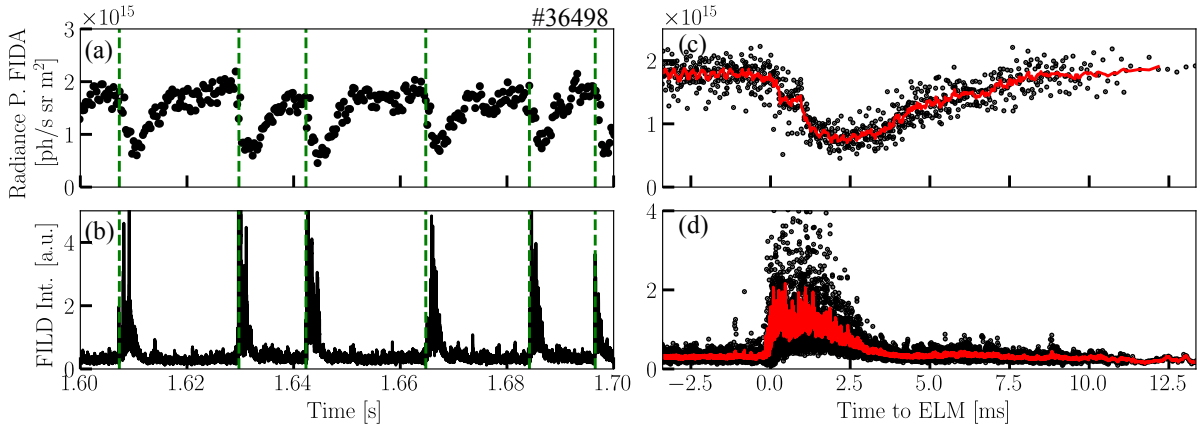

Figure 7.7: Time traces of (a) passive FIDA and (b) FILD signal for the discharge #36 498. The ELM synchronised data points of the (c) passive FIDA emission and (d) FILD signal for the time window 1.55 to 1.95 s. The solid red curves indicate the respective moving averages.

Figure 7.7 shows the time traces of the passive FIDA emission measured and the signal from a FILD situated at the outer midplane. The trend in the passive FIDA trace is similar to that of the analysed discharge (see figure 7.3). The FILD signal shows a large increase in losses measured immediately following the ELM crash lasting around 2.5 ms. During this time the passive FIDA emission decreases and only begins to increase again around 3 ms after the ELM crash. At this point the intensity of the FILD signal has decreased to pre-ELM values.

It should be noted that the FILD measures trapped particles as opposed to the passive FIDA emission resulting from largely passing particles. However the measurements provide further insight into the time scales of ELM induced losses. Future work may look to obtain measurements of the absolute losses by the FILDs to compare measurements of the passive FIDA emission.

7.1.7 Time coherent averaging of profiles

Analysis of the pre and post-ELM spectra and flux requires kinetic profiles for forward modelling. Time coherent averaging has been applied to the electron density and temperature data acquired during the investigated time interval. Data during 1 ms intervals starting from 3 ms before and 1 ms after ELMs, respectively, are conditionally selected and averaged. Figure 7.8 shows profiles fitted to the conditionally averaged data. As can be seen the post-ELM electron density is characterised by a lower pedestal top value and increased SOL density. The post-ELM profiles show a reduction in density extending inwards up to ρ_{pol} ~0.7. Similarly the electron temperature has a decreased pedestal top value, however, the SOL temperature is not significantly increased. ELM resolved ion temperature profiles from the standard CXRS data is not feasible for this discharge as only short 10 ms active NBI beam blips were performed. Since the ELM period is around 15 ms no more than two ELMs occur during the beam on phases. Therefore the ion temperature data is simply averaged over the full time interval. However, as the thermal CX emission contains information on the ion temperature the spectra have been fitted in an attempt to extract ELM resolved ion temperature data for the edge.

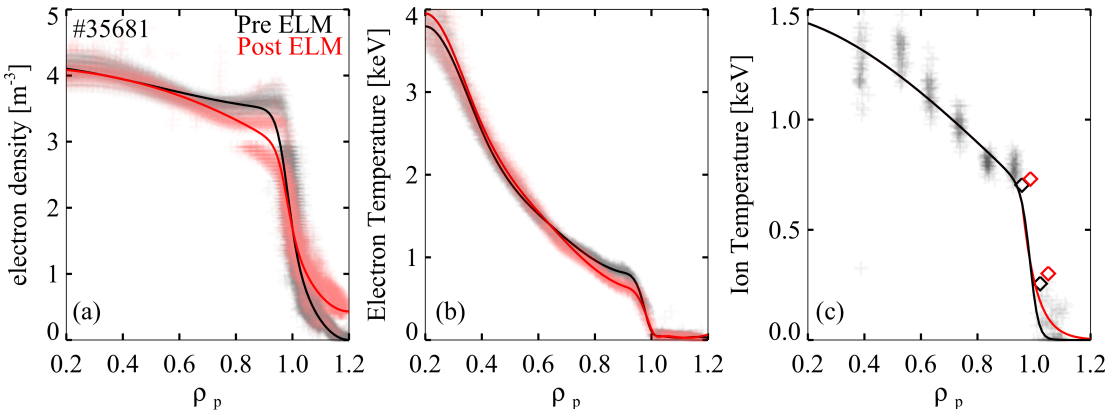

Figure 7.8: A comparison of the pre- (black) and post-ELM (red) profiles of the (a) electron density, (b) electron temperature and (c) ion temperature. The diamond data points represent the ion temperature obtained from fitting the passive D-alpha emission, see figure 7.9. The post-ELM ion temperature profile results in the best match to the thermal CX emission when forward modelled.

7.1.8 Determination of post-ELM ion temperature

Figure 7.9 shows a fit of the unshifted and thermal CX emission measured along the inner view for the pre- and post-ELM times. Here, we assume two Gaussians to describe the passive D-alpha emission. First, radiation from electron impact excitation is considered which is supposed to be dominant in the scrape off layer featuring temperatures of about 20 eV. Secondly, charge exchange radiation is considered from further inside the plasma which contains information on the main-ion temperature.

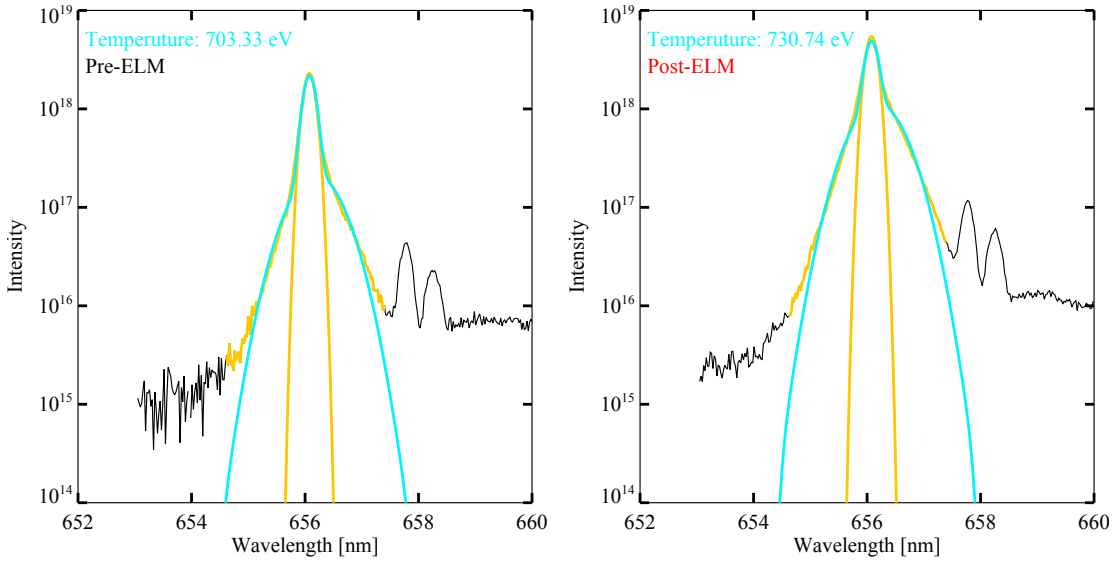

Figure 7.9: Double Gaussian fits to the passive, unshifted and thermal Balmer-alpha emission of the (left) pre- and (right) post-ELM spectra for the inner view. The fit to the unshifted D-alpha emission is plotted in yellow and the combined unshifted and thermal CX emission in cyan from which the temperature is obtained.

The unshifted D-alpha emission has been fitted with a Gaussian restricted to 20 eV. It should be noted that the instrument and Zeeman broadening has been accounted for in the fitting. The measurement region plotted in black has been excluded from the fitting. The cyan plot represents the sum of fit to the unshifted emission and a Gaussian fit to the thermal CX data. The resulting temperatures are shown in figure 7.8c in addition to the profiles measured during the NBI on-phase. The temperature is found to be close to that measured by the active CXRS system. The radial position of the points have been taken where the line of sight is tangential to the flux surfaces. However, as the emission is passive, the localisation of the emission is expected to be broad. The occurrence of the data-points at different positions in ρ_{pol} is explained by the inward movement of the separatrix during the ELMs. Interestingly, the measurement after the ELM crash shows slightly enhanced temperatures in the SOL region which is in line with results from [45], which found that the ion temperature in the SOL increases during ELMs.

7.2 Modelling results

Forward modelling is performed for the times 3 ms before and 1 ms after an ELM. The post-ELM time of 1 ms is chosen as this includes the largest displacement of the plasma separatrix. Note here that the separatrix is not perfectly symmetric during the ELM crash such that the description used here is a simplification. However, modelling results show that the non-axisymmetric contribution is small compared with the overall displacement.

7.2.1 TRANSP modelling

TRANSP modelling with a time step of 1 ms has been performed for a reduced time window considered during this study (1.35 to 1.6 s). Pre and post-ELM phases are modelled by providing the corresponding CLISTE calculated separatrix position and profiles, as presented in figure 7.8. The simulation is initiated with the pre-ELM input, and allowed to evolve up to 1.556 s, after which the post ELM input is considered.

Figure 7.10a compares the plasma stored energy calculated by CLISTE with that of TRANSP. A good comparison for the pre-ELM phase is observed. The post ELM phase is characterised by a decreased thermal stored energy, as result of the collapse in the edge profiles. The calculated fast ion contributing, which constitutes 38 % the stored energy is unaffected. A discrepancy between the measured and simulated store energy for the post-ELM case is observed. This could be a result of the uncertainties in the kinetic input profiles or due to the fact that no fast-ions are removed from the plasma in this simple model. The simulation shows that changes in the kinetic profiles do not result in differences for the fast-ion distribution and beam penetration.

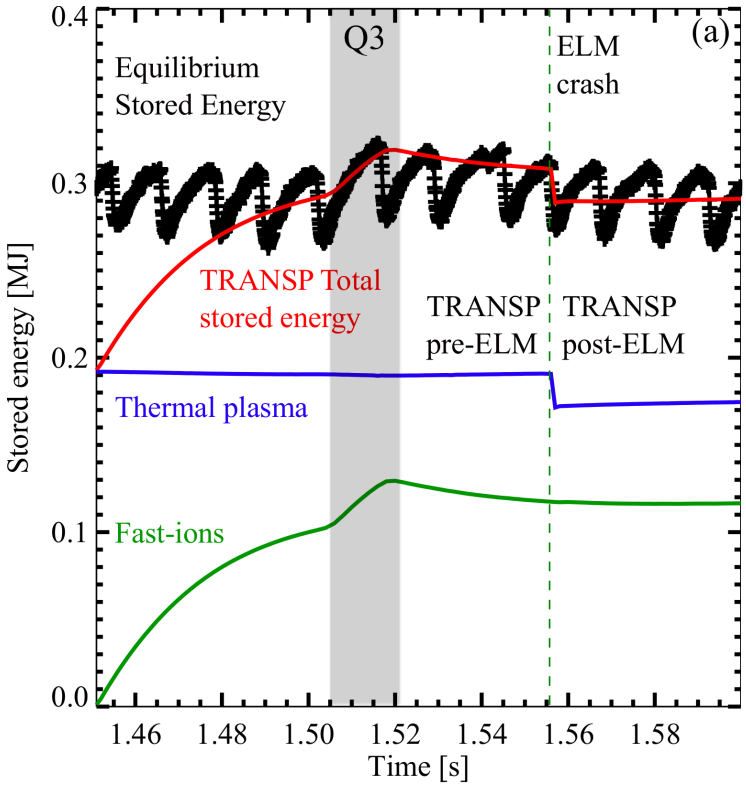

Figure 7.10: Time traces of the plasma stored energy as calculated by CLISTE (black) and TRANSP (red). The thermal (blue) and fast ion (green) contributions are shown. The grey box indicates a time during which beam Q3 was on.

For the calculation of the fast-ion slowing down distribution, no additional anomalous fast-ion transport was considered. The resulting distribution functions were stored and

output for two time points before and after the ELM crash. Figure 7.11 shows the pre-ELM calculated fast-ion distribution.

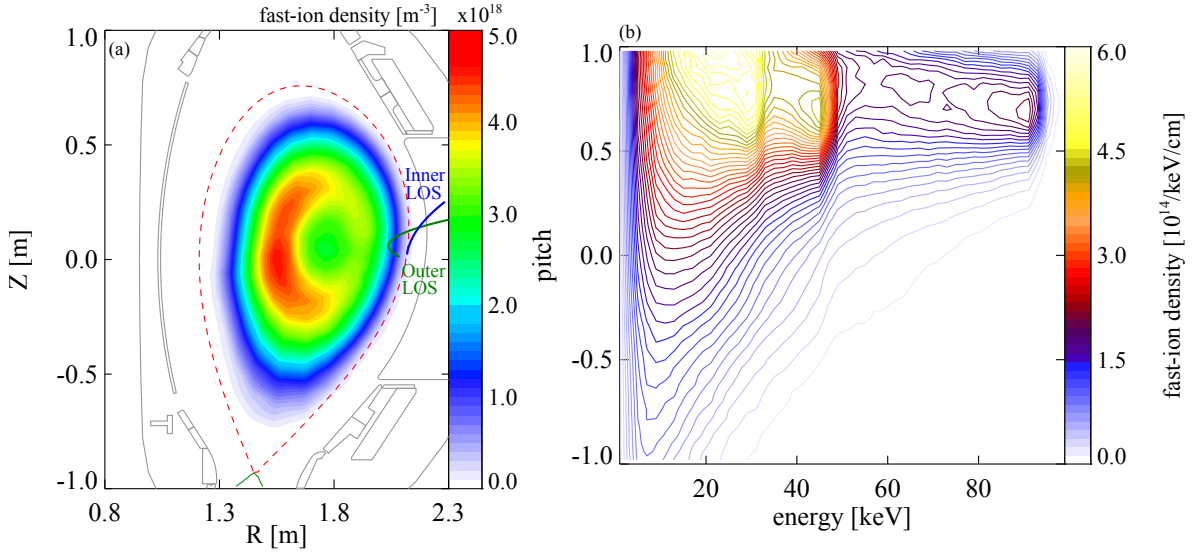

Figure 7.11: (a) Poloidal projection of the TRANSP calculated pre-ELM fast-ion density distribution for the analysed discharge, summed over energy and pitch. The geometry of the inner (green) and outer (blue) LOS are also indicated. (b) The fast-ion velocity space distribution averaged over the R and z.

7.2.2 Background neutral density characterisation

The increase in D-alpha emission as shown in figure 7.5a suggests a possible increase in the neutral density. However, the intensity of the D-alpha emission does also depend on the electron density and temperature, as electron impact collision is the dominant excitation process. As shown in figure 7.9 the fitted kinetic profiles show a clear increase in SOL electron density and temperature. The change in SOL plasma conditions may, further, explain the increase in impurity and Bremsstrahlung emission observed during the ELM cycle, as shown in figure 7.5b and c, as their intensities are proportional to the impurity density. However, it should be noted that ELMs are known to cause impurity flushing [100]. It is interesting to note that the Boron V impurity emission, a known CX line, is also strongly affected by the ELMs.

On the other hand, the decrease in passive FIDA emission observed along the outer LOS, as shown in figures 7.3a and 7.4a may be a result of a reduction in the background neutral density. A decrease in the background neutral density would, however, contradict the increase in FIDA emission observed by the inner LOS as observed in figure 7.3b. It is unlikely that this increase is due to an enhanced or modified fast-ion distribution function. In contrast, it might be well explained by an increased neutral densities shortly after the ELM. Such modifications of the background neutral density may be inferred from the

thermal CX spectra measured along the FIDA lines of sight. Detailed modelling of the background density has been carried out.

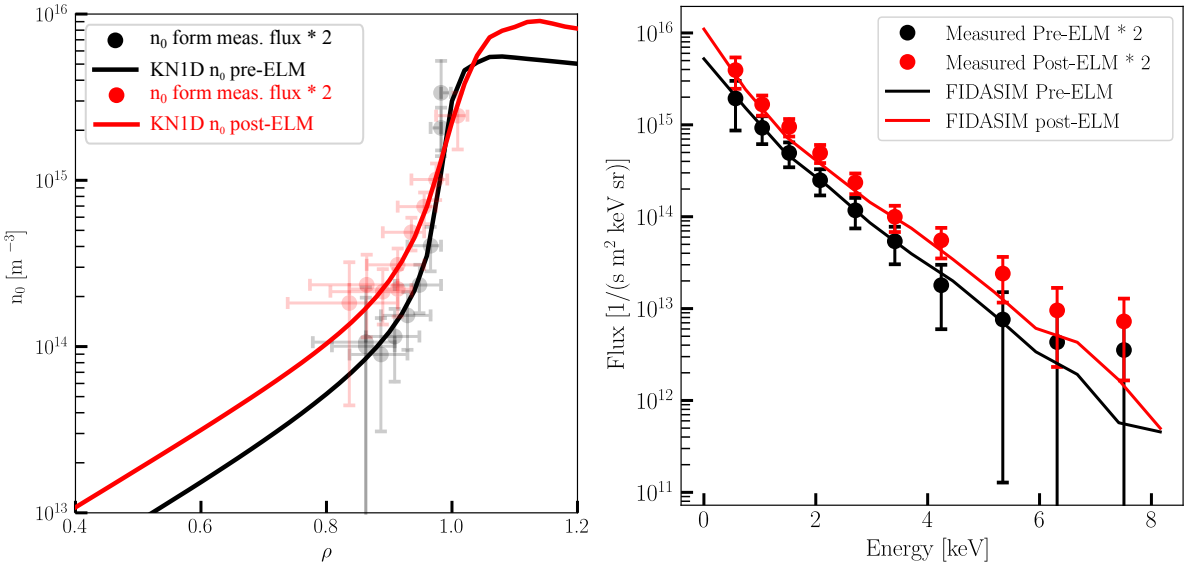

Figure 7.12: Left: A comparison of the pre- and post-ELM background neutral density n_0 obtained from modelling. The n_0 calculated from the measured passive thermal flux (multiplied by a factor 2) is included as points. Right: A comparison between the pre- and post-ELM thermal neutral flux and the synthetic flux calculated by FIDASIM using the corresponding neutral density profiles.

The pre and post-ELM neutral density profiles have been modelled using KN1D and were constrained by the thermal neutral particle spectra. Figure 7.12 shows a comparison of the pre and post-ELM neutral density profiles. Additionally the profiles are compared to the neutral density values calculated from the thermal neutral particle flux as measured by the NPA diagnostic. An excellent qualitative agreement in the profiles shapes is found, while a factor of two is needed to match absolute fluxes (see discussion at the end of section 6.1.3). Both the shape and integrated value of the post-ELM background neutral density differs from the pre-ELM case. The post-ELM neutral density is observed to be increased, likely explained by an increased level of wall recycling following the ELM crash

7.2.3 Comparison modelled spectra

Following the technique described in chapter 6 the pre-ELM passive FIDA emission has been calculated. Figure 7.13 compares the FIDASIM modelled spectra for the pre-ELM case with the measured spectra for both the inner and outer views. The synthetic spectrum (in magenta) includes the thermal contribution. For the outer LOS, a good match between the synthetic and measured spectra is obtained. Only around 655 nm there is a slight mismatch. However, this is most likely due to the camera readout error discussed in

chapter 5, where a decrease in the measured counts is seen to the left of strong emission peaks.

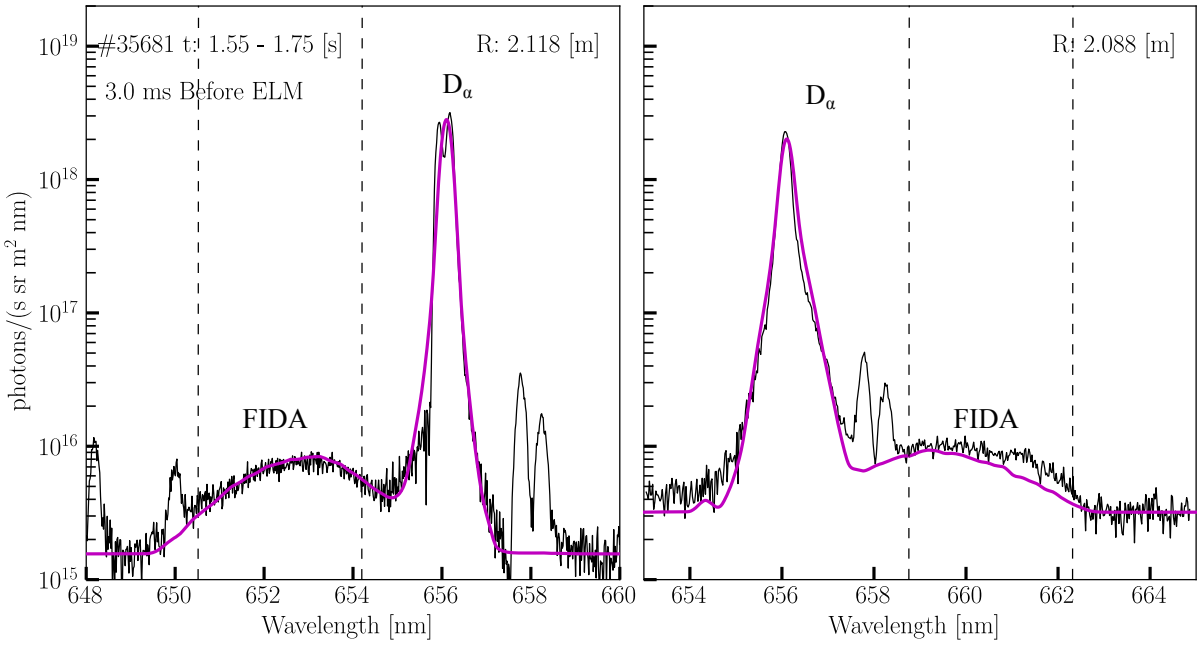

Figure 7.13: Pre-ELM averaged spectra compared to synthetic spectrum calculated using FIDASIM for the (left) outer and (right) inner LOS.

The synthetic spectrum calculated for the inner LOS shows also a reasonably good agreement with the measured spectrum. The calculated thermal emission matches the measurement well. Together with the good comparison between the predicted and measured thermal CX emission of the outer LOS, this suggests that the edge neutral density, considered here, is representative of the experimental conditions.

In contrast, the passive FIDA is underestimated at wavelengths roughly above 661 nm. This discrepancy can, in part, be attributed to additional line radiation from impurity lines and in part by a modified or larger fast-ion population than what is expected from TRANSP. The Doppler shift indicates that this emission region corresponds to particles with energies larger than 45 keV.

Figure 7.14 shows the post-ELM forward modelled spectra compared to the experimental spectra for both LOS. A good match of the calculated thermal CX emission to measured spectra suggest that also the post-ELM modelled neutral density profiles describes the experimental conditions well. The outer LOS shows an overestimation of the FIDA emission while the inner LOS exhibits a better agreement between measurement and modelling. The post-ELM synthetic spectrum of the outer view further does not show the same discrepancy for large Doppler shifted wavelengths as observed for the pre-ELM calculation. This suggests that the high energy particles are preferentially lost. Also for the outer LOS, the synthetic FIDA spectrum is well above the measured one, when accounting for impurity lines. This overestimation is attributed to a non neoclassical loss of fast-ions

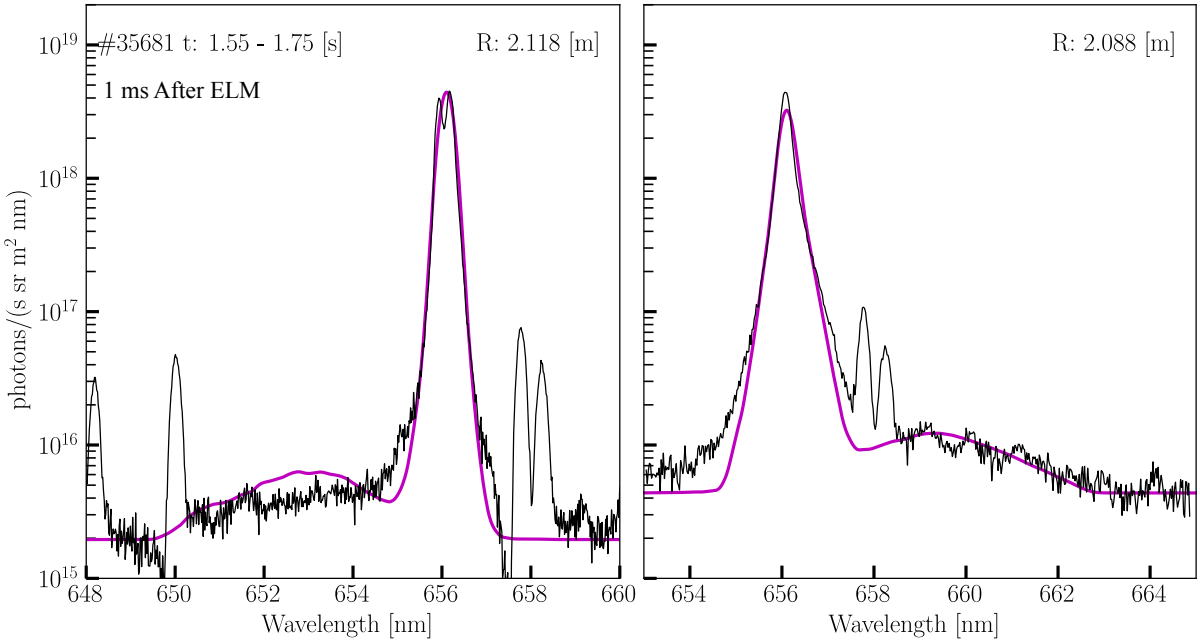

Figure 7.14: A comparison of the conditionally averaged post-ELM passive spectra to the FIDASIM calculated spectra for the (left) outer and (right) inner LOS.

induced by ELMs. However, before a quantitative calculation of the fast-ion losses is made the change in the plasma position is further investigated.

7.2.4 ELM-induced change plasma boundary position

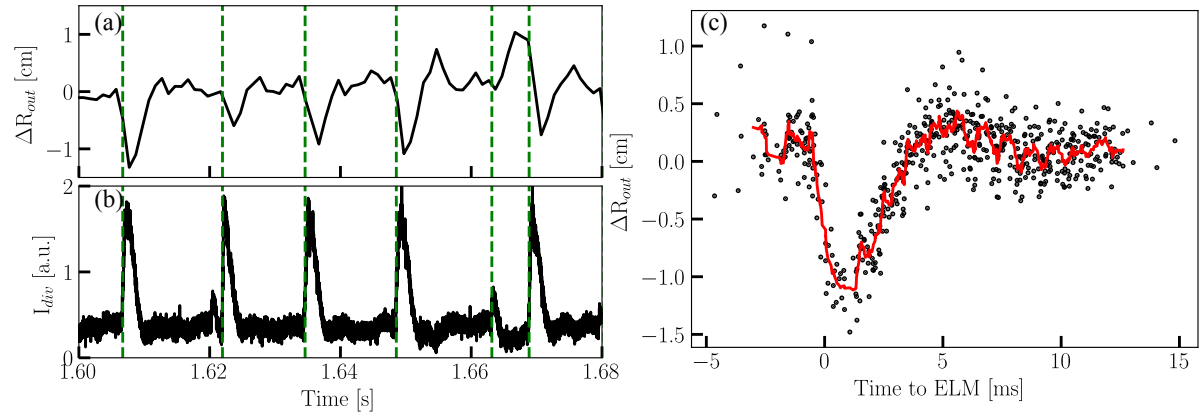

Figure 7.15: Time traces of the (a) average displacement of outer most separatrix position R_{out} (b) and outer divertor shunt current. Negative ΔR_{out} indicates inward movement. (c) ELM synchronised data points of ΔR_{out} (black) with the rolling average in red.

One effect that would result in a reduction of the fast ion density along the LOS

is the change in plasma position during the ELM cycle. Figure 7.15 shows the time trace of the change in the outer separatrix position, with respect to the average position (R_{sep} =2.12 cm), as calculated by the equilibrium code CLISTE. The trace shows that the calculated separatrix moves up to 1.5 cm inwards during an ELM cycle. However, the average recovery time of the plasma position is only about 5 ms. This is shorter than the recovery of the passive FIDA light and therefore indicates that the plasma movement does not dominate the observed changes of passive FIDA light. Moreover, small ELMs exist that show hardly any plasma movement but still exhibit strong changes of the passive FIDA light. Examples are the ELM at 1.62 s and another shortly after 1.66 s in figs. 7.3a and 7.15a. The movement calculated in the plasma position for these times is low yet the FIDA emission over the same time period behaves similar to most other ELMs.

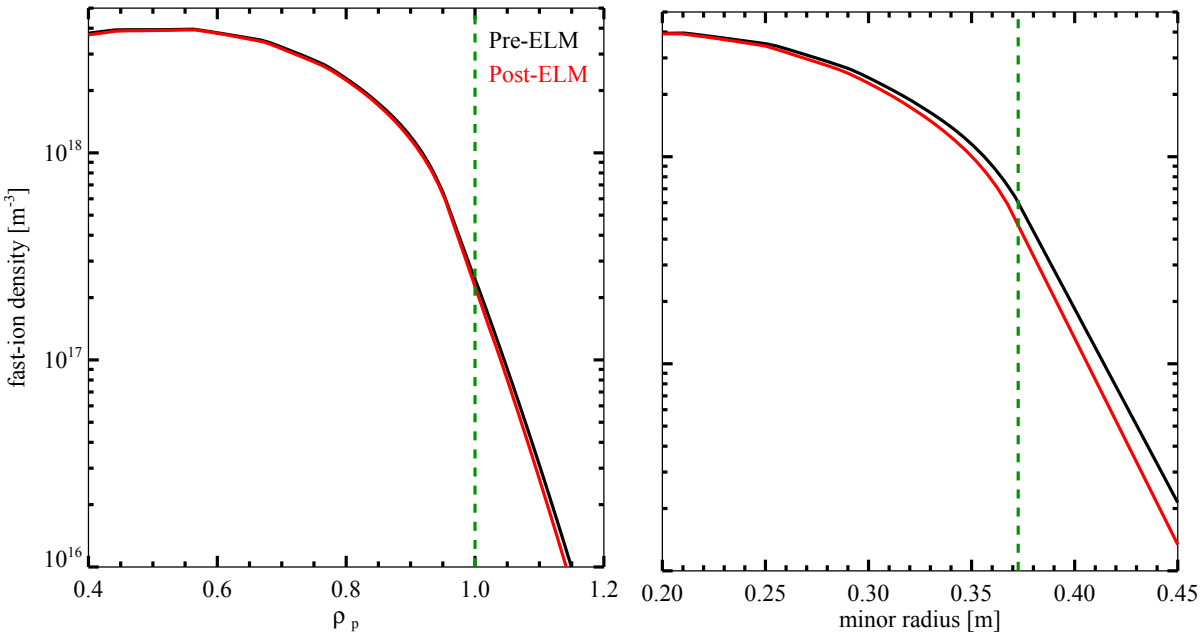

Figure 7.16: A comparison of the TRANSP calculated pre- and post-ELM fast-ion density profiles mapped to the (left) normalised poloidal flux coordinate ρ_{pol} and (right) minor radius.

For the analysed discharge the movement of the plasma separatrix is on average more than 1 cm. It is necessary to consider the change in passive FIDA as a result of the plasma movement as the fast-ion density would necessarily decrease along a given LOS if the plasma were to move inward. Therefore the post-ELM separatrix position has been taken from a time point where the plasma has moved more than 1 cm. Figure 7.16 compares the fast-ion density profile of the TRANSP calculated pre- and post-ELM distributions along the outer midplane. On the left the profiles are plotted with respect to the normalised poloidal flux coordinate, ρ_{pol}, and on the right against the minor radius in real space. As can be seen, there is little change in the profile as plotted against ρ_{pol}, however when plotting the profiles in real space, the inward movement does result in a reduction of the

fast-ion density at the measurement location.

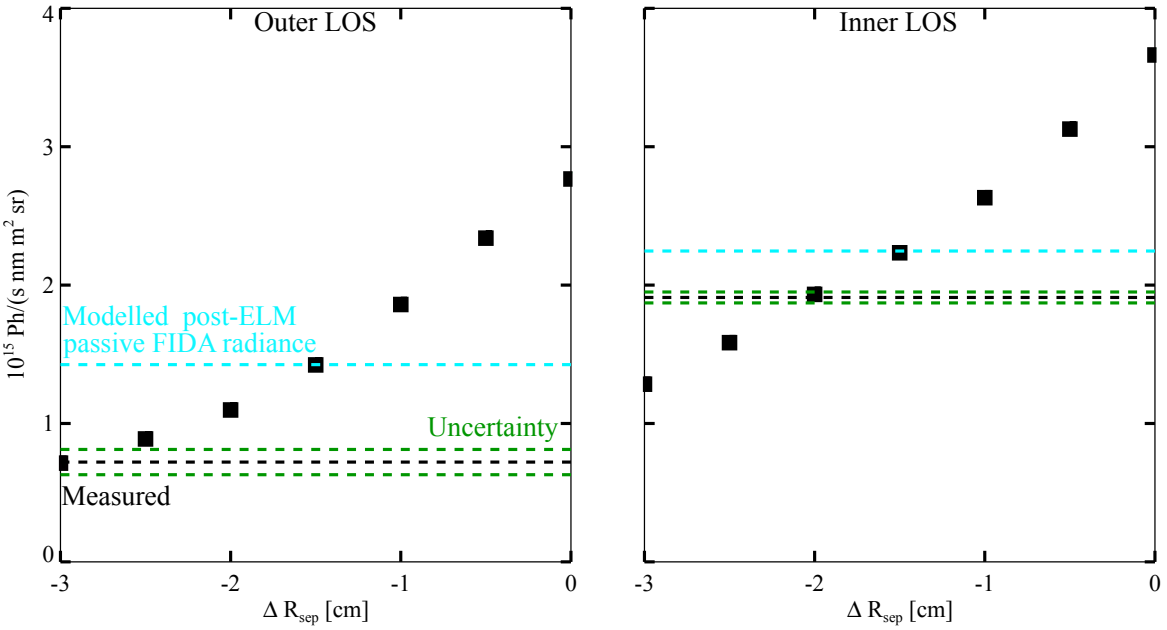

Figure 7.17: A scan of the synthetic passive FIDA radiance (black squares) calculated for 0.5 cm inward radial movements of the pre-ELM TRANSP fast-ion distribution for the (left) outer and (right) inner LOS. The measured post-ELM FIDA radiance is indicated by the horizontal black dashed lines with the uncertainty range represented by the green lines. The post-ELM modelled FIDA radiance is indicated by the cyan lines.

A scan modifying the global radial position of the TRANSP calculated pre-ELM fast-ion distribution function has been performed. Hereby the relative change in the measured passive FIDA radiance that results from the movement in the separatrix position can be addressed. Figure 7.17 presents the results of the scan whereby the distribution function is moved inwards in steps of 0.5 cm with respect to the separatrix position R_{sep}. The black dashed lines indicate the measured post-ELM FIDA intensity and the green lines the uncertainty range. The cyan dashed lines represent the synthetic FIDA intensity calculated from the post ELM distribution function. Comparing the radiance calculated for the unshifted distribution to that of the post-ELM modelled emission, it can be concluded that the movement represents around 65 % of the observed post-ELM reduction in passive FIDA emission for the outer view and around 80 % for the inner view. To explain the measurements with a shift of the plasma boundary, an additional 1 cm would be necessary. This is double the observed variation and indicates that additional physics processes need to be taken into account. Since the movement of the plasma separatrix has already been considered in the analysis presented we therefore conclude the discrepancy to be a result of the ejection of fast ions.

7.2.5 Modification of the fast-ion distribution function

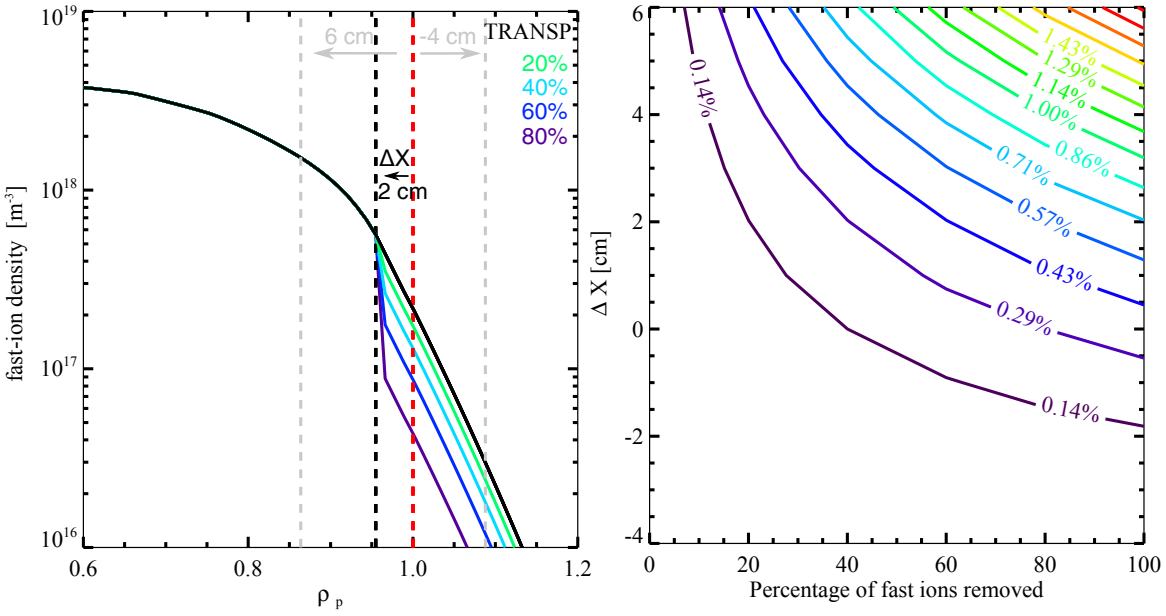

Figure 7.18: Left: A scan of modifications to the TRANSP post-ELM fast-ion density profile (black). Modifications extend outwards from ΔX marked by the vertical black dashed line. The scan range of ΔX is indicated by the vertical grey lines. The coloured profiles represent modifications where the density is reduced by factors of 20 %. Right: A contour plot presenting the corresponding fast-ion losses for the modification scan, as a percentage of the total fast-ion content.

To estimate the quantity of fast ions ejected and the radial region affected as a result of an ELM crash a scan is performed whereby the TRANSP post-ELM fast-ion density profile is modified in two dimensions ΔX and Δn_{fast} as illustrated in figure 7.18. Starting from $\Delta X = 6\,\text{cm}$ inside the separatrix and extending outwards, the fast-ion density is reduced in increments of 20 %, between 0 and 100 %. The starting position of the region modified, labelled ΔX, is scanned by incrementally moving outwards in steps of 1 cm, from 6 to $-4\,\text{cm}$, where positive values mark positions inside the separatrix and negative values positions outside. The graph on the right of figure 7.18 shows the corresponding losses for the scan of modifications to the fast-ion density profiles, as a percentage of the total fast-ion content. The horizontal axis indicates the fraction of fast ions removed and the vertical axis the radial starting point of the modifications. The upper right corner ($\Delta X = 6\,\text{cm}$, $\Delta n_{\text{fast}} = 100\,\%$) therefore represents the modification whereby all fast ions from within 6 cm of the plasma are removed. As can be seen from the point (0 cm, 100 %), the total number of fast-ions outside the separatrix constitutes around 0.4 % of the total fast-ion content. It should be noted that the fraction of particles is applied uniformly with respect to pitch end energy.

Figure 7.19 presents the FIDASIM calculated spectra for modifications of the SOL fast-

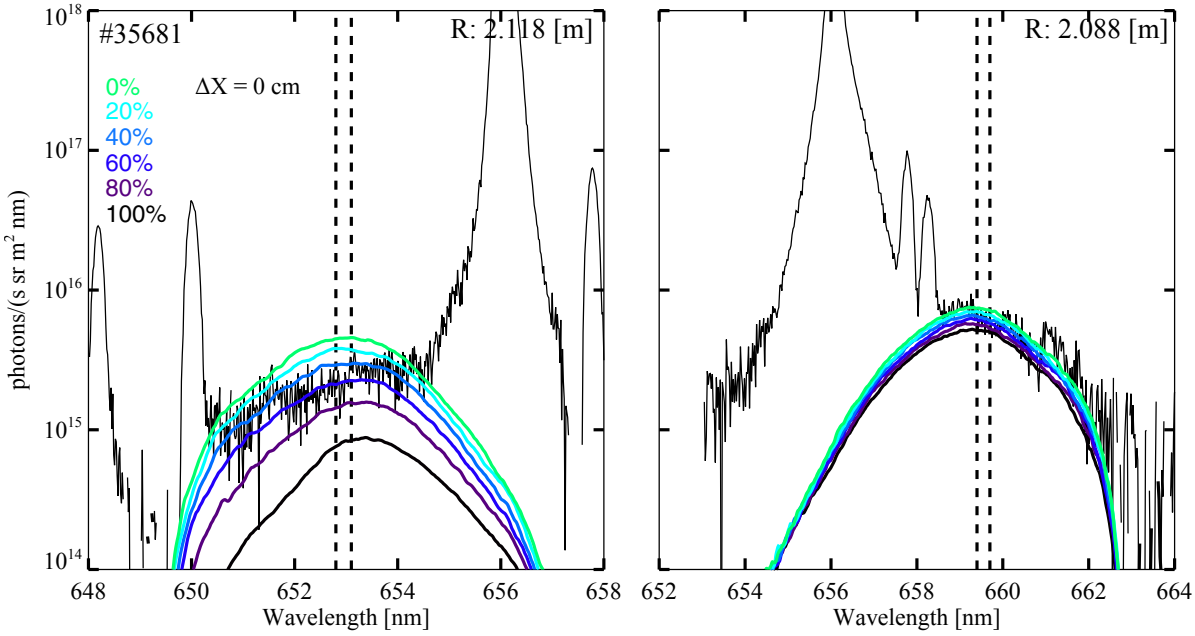

Figure 7.19: A comparison of the post-ELM measured spectra to the synthetic spectra obtained from the scan of the modifications to fast-ion density profile presented in figure 7.18, for the (left) outer and (right) inner LOS. The vertical dashed lines indicate the wavelength range over which the comparison against the measured spectra is made.

ion content, i.e. ΔX =0 cm for both LOS. The synthetic spectra are plotted in different colours corresponding to the percentage of particles removed. The green spectra labelled 0 % represents the unmodified TRANSP post-ELM case. For an increasing amount of particles removed the calculated passive FIDA intensity decreases. As expected, the outer view is more susceptible to changes in the SOL fast-ion density, as compared to the inner view. This can be explained by the spatial regions probed by the two LOS as presented in figure 7.20. The inner LOS observes emission over a broad region extending from ρ_{pol} ~0.75 to 1.15. Therefore, emission from the SOL contributes only a minority of the signal and modifications to the SOL are not significant. The outer view, however, observes emission largely from the separatrix outward and is sensitive to modifications in this region. Here the best match between the calculated and measured spectrum is a reduction of 60 % of the SOL fast-ion density (the simulation plotted in blue) for the outer view and a reduction in the range of 20 to 60 % for the inner LOS.

Figure 7.21 presents a 2D overview of the degree of agreement between the measured and modelled spectra as a function of ΔX and the modified percentage. The colour code is as follows. Black represents a match with less than 5 % absolute difference as compared to the measured spectrum. The relative error of the measured passive FIDA emission is calculated to be less than 15 % for the outer view, while the inner view is less than 5 %. Therefore the contours within light purple correspond to calculated spectra falling within the uncertainty for the outer LOS, while black falls within the uncertainty for the inner

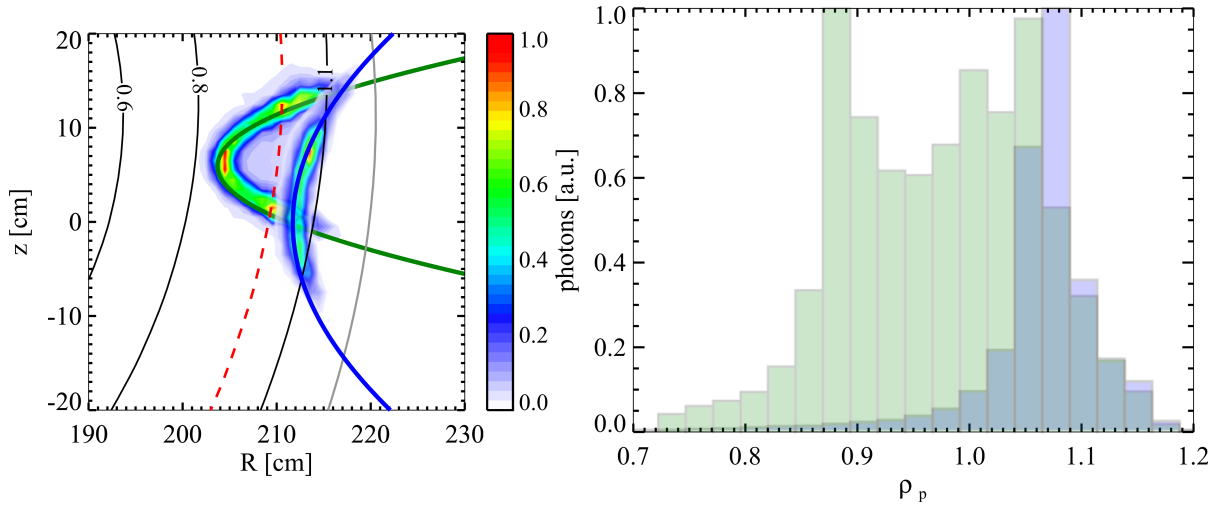

Figure 7.20: (Left) Poloidal view of passive FIDA emission observed by the inner (blue) and outer (green) LOS. (Right) The corresponding region passive FIDA emission is collected from in terms of ρ_{pol}.

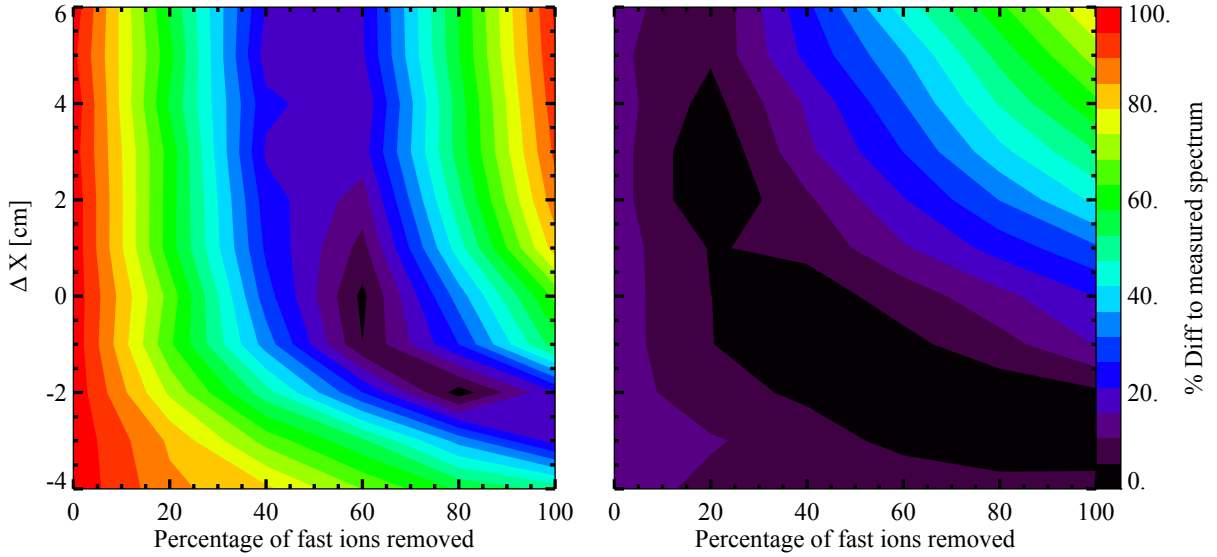

Figure 7.21: Results from the comparison of the measured post-ELM passive FIDA radiance to the synthetic passive FIDA calculated from the scan of modifications to the fast-ion density profile presented in figure 7.18 for the (left) outer and (right) inner LOS.

LOS.

Figure 7.21 shows that the best match to spectra corresponds to a 60 % reduction of fast-ion content with delta ΔX =0, i.e. from the separatrix increasing for modifications to radial locations further outside. As the outer LOS does not probe significantly deeper than the separatrix, modifications to the fast-ion density extending further into the plasma

reveals no additional radial information. The depth of ELM induced modifications can be inferred from the comparison with the inner LOS. A reduction of 20 % of the particles up to 4 cm matches the ELM induced change in emission intensity of the inner LOS. According to figure 7.18 the amount of fast ion lost with respect to the total fast ion content is found to be less than 0.3 %. This corresponds to a loss of less than 1 % of the fast-ion stored energy with respect to the pre-ELM total and can hence not explain the difference of the TRANSP stored energy with respect to the measurement in figure 7.10.

7.2.6 Comparison with theoretical predictions

To estimate the radial extent that an ELM is expected to have on the fast-ion content a comparison against the MHD code JOREK [101] is made. Non-linear simulations of multiple type-I ELM crashes with realistic temporal evolution have been obtained for the first time by [102]. The simulation results are for an AUG H-Mode plasma similar to discharge #33616 at 7.2 s. The average ELM frequency and the thermal energy expelled are around half that of ELMs from the analysed discharge at 40 Hz and 6 % respectively. Despite the difference in ELM magnitude and frequency between the analysed and JOREK modelled ELMs the comparison is still useful to obtain a qualitative comparison.

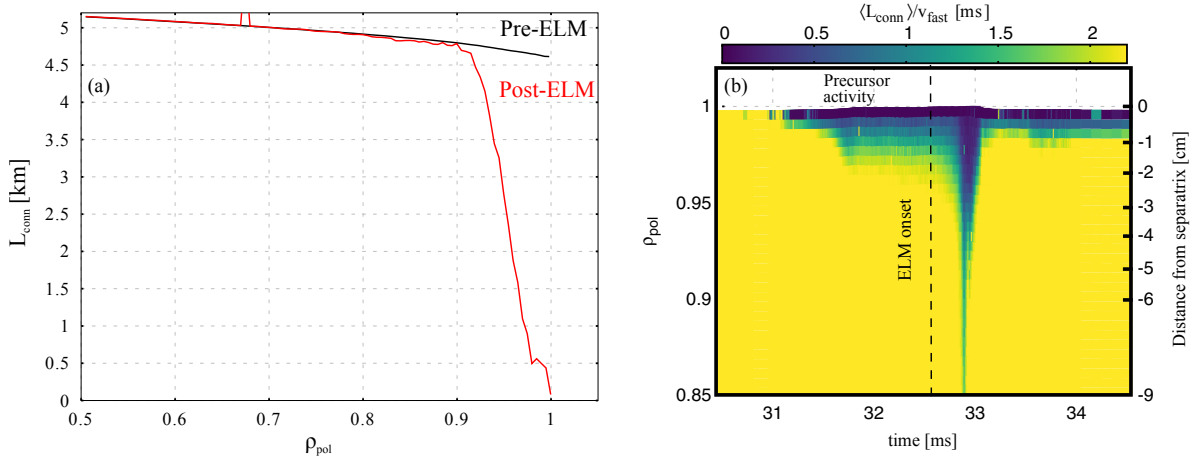

Figure 7.22: Left: A comparison of the JOREK calculated pre and post-ELM connection length L_{conn}. Right: JOREK calculated evolution of L_{conn} divided by v_{fast} =20.8 km s^{-1}, representing the speed of a 45 keV fast deuterium particle travelling parallel to the field lines. The ELM crash starts around 32.5 ms, with modifications prior related to precursor activity not observed in the analysed discharge [102].

The connection length is used as a proxy to determine the radial extent on which fast-ions are expected to be affected. Figure 7.22a shows the modelled connection length L_{conn} profile, for pre and post-ELM phases. The pre-ELM connection length has finite values due to numerically constraining the length confined field lines are traced. Hence these values can be considered as infinitely long. As can be seen the post ELM connection

length is modified and decreases with respect to the pre-ELM profile, with the modification extending up to around 4 cm ($\rho_{\mathrm{pol}} \sim 0.9$).

Figure 7.22b shows the evolution of L_{conn} divided by a speed of a (v_{fast} =) 45 keV fast particle with pitch =1. Considering such a fast particle travelling parallel to the magnetic field, the quantity represents the average time to reach the end of the associated field line, in effect a loss time. Colours in yellow correspond to the unmodified pre-ELM connection length, therefore these values can be disregarded. Shades of blue indicate the region modified. A short spike extending more than 6 cm is observed during the ELM crash but is likely too short lived to significantly impact particles. A prolonged modification extending up to around 4 cm is observed. The estimated loss time during the ELM crash is observed to be significantly less than 1 ms for 45 keV fast particles.

Despite the good qualitative agreement with the results from passive FIDA measurements further modelling is required for a quantitative comparison, in particular of the absolute loss fraction. This would involve considering the full kinetic distribution of fast ions. Additionally the temporal evolution of the connection length should be considered, as L_{conn} is observed to change on time scales comparable to the loss time. Thus particle tracing of a representative fast-ion distribution in JOREK is planned for future work. Lastly it should be noted that JOREK does not simulate the SOL. Here modelling by LOCUST with JOREK calculated field perturbations as input could be considered.

7.3 Summary

High speed measurements of Balmer emission viewed along two edge LOS show ELM correlated modulation of the passive FIDA intensity. Despite the presence of TAE's and an NTM, the pre-ELM passive FIDA emission at the edge could be well modelled with a neo-classical fast-ion distribution calculated by TRANSP. Post-ELM modelling addressed both the change in neutral density and movement of the plasma separatrix as a result of the ELM. Kinetic profile changes n_{e}, T_{e}, T_{i} are not expected to influence the FIDA signal. The post-ELM background neutral density, constrained against the thermal CX emission, is found to increase significantly. This is in good qualitative agreement with calculations of the neutral density from the measured passive thermal neutral particle fluxes. The movement of the plasma separatrix is found to be partly responsible for the change in the measured emission, however, the post-ELM decreased passive FIDA emission cannot be explained by only the separatrix movement. The discrepancy is concluded to be a result of ELM induced fast-ion losses. To quantify both the absolute losses and the radial extent of modifications to the fast-ion distribution a scan is performed removing particles in step like manner. Comparing the FIDASIM calculated spectra to the measured spectra shows that a reduction of 60 % of the SOL fast-ion content and 20 % of the fast-ion content up to 4 cm inside the separatrix best agree with measurements. This is less than 0.3 % of the total fast ion content. The ELM affected region is found to be up to 4 cm inside the separatrix which is in good agreement with the radial extent of modifications to the connection length calculated by a simulation of an ELM crash using the nonlinear MHD code JOREK.

Chapter 8

Summary and Outlook

Good confinement of fusion born alpha particles is important for future fusion reactors as losses would not only degrade plasma heating and therefore fusion performance, but can also lead to damage of the first wall components if the losses are localised. Several mechanisms and plasma instabilities have been identified that can degrade fast-ion confinement. Fast ions at the edge are especially at risk as they need only be displaced by a small amount to enter loss orbits. One type of instability, known as the edge localised mode (ELM) is of particular interest as it provides a strong perturbation at the plasma edge and might cause significant fast-ion losses. However, studies of ELM-induced fast-ion loss and redistribution require sensitive fast-ion diagnostics that cover a broad range of the fast-ion phase space which were hardly available. A new edge fast-ion D-alpha (FIDA) spectroscopy system has therefore been developed within the framework of this thesis making use of passive radiation and providing for the first time radially resolved information of the confined fast-ion density.

A pair of prototype high photon throughput spectrometers has been assembled. The spectrometers make use of a blocking bar placed close to the attached CCD camera, to dim but not completely block the bright unshifted D-alpha emission. The design therefore allows to measure the unshifted D-alpha emission and the red and blue shifted FIDA emission with high dynamic range. The use of blocking bars are common in FIDA spectroscopy, however the new design removes the need for additional correcting lenses, reducing transmission losses and improving the image quality. The spectrometers have been connected to an optical system with lines of sight (LOS) that intersect a neutral heating beam close to the plasma edge. The geometry of the LOS imposes that the Doppler shifted FIDA emission observed is largely from passing fast ions. An array of LOS can be connected to the spectrometer which provides profile information with a radial resolution of $\rho = 0.03$ (1.5 cm) for active FIDA measurements. Additionally, the spectrometers can be configured to measure with only one channel but with a time resolution of 200 µs making use of a burst mode feature of the CCD cameras. This significantly improves on the temporal resolution of the existing core FIDA system which is typically operated with 5 ms and is the main mode of operation for this study. An absolute intensity and wavelength calibration has been performed for both spectrometers. Comparing the new spectrometers to a standard

non optimised CXRS spectrometer at AUG shows an increase of up to 100 % in the photon throughput. Both multi-channel and single channel burst mode measurements have been demonstrated.

Measurements in discharges with 5 MW of off-axis NBI heating power have shown a significant passive contribution to the edge FIDA emission. This complicates the analysis of the active emission, in particular, during transient events such as ELMs. Therefore, a method for extracting information from the passive FIDA emission has been developed. This method provides information on both the fast-ion and background neutral density and is based on forward modelling using the FIDASIM code. FIDASIM has been upgraded to additionally model the passive thermal emission based on input 1D neutral density profiles. This allows to constrain the background neutral density profiles modelled with the neutral transport code KN1D via comparisons of synthetic and experimental spectra. Typically a good agreement between the synthetic and measured thermal emission can be achieved for multiple lines of sight, suggesting the experimental neutral densities are well described. Additionally, it is found that the neutral density profile calculated from the thermal particle spectra measured by NPA detectors is in good qualitative agreement with the KN1D neutral profiles. This is also found for the ELM resolved background neutral density evolution.

TRANSP modelling has been applied to obtain theoretical fast-ion distribution functions. Hereby, it turned out that including the experimental neutral density profiles is important since CX fast-ion losses can be as large as 10 % of the total fast-ion content. With the TRANSP predicted fast-ion distribution functions and the calculated neutral densities, passive FIDA spectra can be determined. However, a significant fraction of the passive FIDA emission is found to originate from the SOL, in particular for the outer LOS, while TRANSP only yields information of the confined plasma region inside the separatrix. Modelling has been performed with the 3D fast-ion orbit following code LOCUST to determine the SOL fast-ion density. It is found that the fast-ion density can be well approximated by an exponential extrapolation of the density near the separatrix. Applying the extrapolation to the TRANSP fast-ion density the calculated passive FIDA spectra show typically good agreement with the measurements.

However, after ELM crashes, passive FIDA measurements acquired with high temporal resolution show a clear drop of the FIDA emission which does not agree with TRANSP/FIDASIM modelling. In particular measurements of the outer LOS that views largely emission from the SOL show a strong reduction of the passive FIDA emission due to ELMs. In contrast, the FIDA emission from the inner LOS, with a deeper view through the plasma, shows increased FIDA radiation immediately after ELM crashes, followed by a slight reduction. The FIDA emission is observed to recover on the same time scale for both LOS.

The initial increase observed by the inner LOS can be explained by an increase of the neutral density right after ELMs, as suggested by the analysis of the post-ELM neutral density by the KN1D neutral code, constrained by the thermal CX emission. This is further supported by calculations of the post-ELM neutral density from the passive thermal particle flux. The following drop of the FIDA signal in the outer and inner LOS can be

in part explained by the ELM-induced inward movement of the separatrix. Calculations of the separatrix position by the CLISTE equilibrium solver shows an inward movement of ∼1 cm of the separatrix, which can explain the reduced signals in the inner and outer views to 80 % and 60 %, respectively. The remaining discrepancy (still 20 % to 40 %) can then be attributed to a fast-ion redistribution which is further supported by measurements from fast-ion loss detectors that report increased signals during the ELMs studied, here. Sensitivity studies show that the observed discrepancy of 20 to 40 % cannot be attributed to further uncertainties in the separatrix position. Furthermore, the occurrence of "small" ELMs with little to no effect on the separatrix position are still observed to reduce the passive FIDA emission. This emphasises that the change in separatrix position alone is not responsible for the reduction in FIDA emission.

To gain information on the radial dependence of the ELM-induced redistribution, a forward model to fit the ELM losses to the experimental data has been developed. It consists of a scan of the extent of the ELM affected area and the strength of ELM losses. By using both lines of sight we find a 60 % reduction in the SOL fast-ion content and a reduction of around 20 % extending from the separatrix inward up to 4 cm into the plasma. The corresponding amount of fast-ion losses is less than 0.3 % of the total population.

The results from the scan are compared to recent results from the JOREK code which allows simulating the evolution of the ELM cycle. In particular, modifications to the connection length are provided by JOREK which can be used to estimate the region that the fast-ion distribution will be affected. A shortening of connection lengths up to 4 cm inside the confined region is predicted during ELMs which agrees very well with the passive FIDA measurements. It should be noted, however, that the simulation corresponds to a discharge with different plasma conditions and in particular less intense ELM crashes.

Outlook

Further modelling of the ELM redistribution of fast ions is planned using JOREK. It is foreseen to carry out particle tracking with a representative fast-ion distribution to calculate absolute fast-ion losses. In addition, the analysis of passive FIDA can be extended to discharges with differing ELM frequencies and amplitudes. In combination with modelling by JOREK this would provide a clear benchmark as not only absolute values but also trends and dependencies could be addressed. Importantly, modelling of the ELM induced fast-ion losses, would allow to address the expected local heating of plasma facing components due to ELM ejected fast ions in future fusion devices such as ITER.

Moreover, the new edge FIDA system allows to quantitatively study several mechanisms known to induce fast-ion losses. In particular Alfvén eigenmodes close to the edge could be addressed. These modes are of particular concern for ITER, the next generation fusion device, as they could lead to an unacceptable amount of alpha particle losses in presence of many overlapping modes [15, 99].

Furthermore, radially resolved active FIDA measurements would allow to study transport induced by resonant magnetic field perturbations. Modelling and measurements from FILD suggest an edge resonant transport layer results in increased fast-ion losses [30]. The new system would allow to determine the radial extent and the absolute change in the

fast-ion density.

Minor modifications to the system could be considered to further improve the measurement capabilities. For example, the inclusion of LOS with different angles with respect to the neutral beam would allow for tomographic reconstruction of the fast-ion distribution at the edge. This technique is often applied during core FIDA measurements on AUG to directly calculate the velocity space distribution [88]. Furthermore, an increase in the temporal resolution of the system down to the tens of microseconds would allow to infer detailed information on the velocity space redistribution of lower frequency MHD modes such as NTMs with frequencies less than about 10 kHz. The time resolution of the system is currently limited by the SNR at shorter exposure times. This is less severe for core active FIDA measurements, where the fast-ion density is larger. Therefore, this motivates such measurements along core LOS, to compliment the core FIDA system.

Additionally, an increase in the temporal resolution for FIDA measurements on the edge LOS could be achieved by making use of a gas puff injection system, already present. The gas puff can provide an active source of donor neutrals which can be modulated on the sub millisecond timescale for passive subtraction. In this way localised active FIDA emission can be measured during the ELM cycle. However, molecular emission lines present an additional source of noise that may be difficult to disentangle from the FIDA emission. This can be counteracted by moving the plasma closer to the gas puff during experiments, such that the molecular deuterium is dissociated before reaching the LOS, or alternatively measuring along deeper LOS.

The analysis of the passive Balmer emission during this thesis has allowed to obtain information on the background neutral density. In this work 1D neutral density profiles were found to sufficiently describe the experimental conditions along the LOS. However, a quantitative discrepancy with profiles calculated from passive NPA measurements was found. This is in part suspected to be a result of the toroidal asymmetry in the background neutral density. However, 3D modelling of the background neutral density using EMC3-EIRENE would be able to address this.

Lastly, given the sensitivity of passive FIDA emission to small relative modifications of the fast-ion distribution at AUG, a feasibility study could be considered to determine whether such measurements in ITER would be practical. The large plasma volume and density will produce a large Bremsstrahlung contribution which will add a significant level of photon noise to core FIDA measurements. A passive FIDA system with LOS viewing the edge observes less of the plasma and therefore a lower Bremsstrahlung intensity compared to core LOS. However, it will need to be determined if the expected background neutral density integrated along edge LOS would provide a sufficiently large source of donor neutrals for the passive FIDA emission to be measurable on reasonable timescales.

Acknowledgements

Here I would like to thank some of the people without whom this work would not have been possible. Firstly, I would like to thank my academic supervisor professor Hartmut Zohm, both for the opportunity to carry out this PhD work at IPP and for his insightful discussions. Furthermore, I would like to especially thank professor Benedikt Geiger for his excellent supervision during this work. His expertise in the field of fast ions and experimental physics was key for the progress of this work.

Additionally, I would like to thank Dr. Philip Schneider for his great collaborative supervision. His many helpful conversations are greatly appreciated. I would also like to thank Dr. Asger Jacobsen for his support during this work and for instructing me on how to use the LOCUST code.

I would like to thank many of the people who contributed and provided assistance with hardware and installations in the laboratory including: Holger Köhnlein for designing the spectrometers; Dr. Marco Cavedon for his help with using the edge CXRS optical system, as well as for his input in running the cameras in the spectra-kinetics mode; Dr. Ralph Dux for providing direction with the installation of the spectrometers; Michael Rolffs for preparing and optimising many of the spectrometer components; Dr. Rachael McDermott and Dr. Athina Kappatou for their helpful advice and support in the laboratory.

Additionally, I would like to thank many of the people who contributed and aided this work through software and simulation tools namely: Dr. Tilmann Lunt for his help with running the EMC3-EIRENE code; Dr. Mathias Bernhardt and Johannes Gnilsen for getting me started with KN1D; Dr. Giovanni Tardini for his continued assistance with TRANSP; Dr. Michael Dunne for his ELM stability analysis; Dr. Philipp Lauber for his TAE modelling efforts with HAGIS; Klara Bogar for providing me with her scripts to calculate the neutral density from the NPA measurements; Dr. Matthias Hölzl and Andres Cathey for providing theoretical predictions from the JOREK code; and Dr. Markus Weiland his very useful python-IDL wrapper.

Importantly, I would like to thank the entire ASDEX Upgrade team for their great support and the wonderful work environment over the course of my time at IPP.

I would also like to thank the W7-X team for the great support provided during my stay there, a special thanks to: Dr. Oliver Ford, Dr. Jürgen Balzun and Dr. Thomas Wegner and to professor Thomas Klinger for the opportunity.

Furthermore, I would like to thank many of my colleagues who have greatly enriched my experience during this work: Emile, Peter, Teo, Davide, Monika, Maxi, Joaquin, Diego,

Javi and especially Pilar thank you so much.

Last but not least, I would like to thank my parents Anton and Marieta, and my sister Paula, for their fantastic moral support and encouragement from back home.

Bibliography

[1] Fusion in the sun-nuclear fusion. https://en.wikipedia.org/wiki/Nuclear_fusion#/media/File:FusionintheSun.svg. Accessed: 2020-03-03.

[2] Plotting nuclear fusion cross sections. https://scipython.com/blog/plotting-nuclear-fusion-cross-sections. Accessed: 2020-03-03.

[3] IAEA nuclear data services. https://www-nds.iaea.org/. Accessed: 2020-03-03.

[4] J. D. Lawson. Some criteria for a power producing thermonuclear reactor. *Proceedings of the Physical Society. Section B*, 70(1):6–10, Jan 1957.

[5] E. G. Adelberger et al. Solar fusion cross sections. ii. the pp chain and cno cycles. *Rev. Mod. Phys.*, 83:195–245, Apr 2011.

[6] Tokamak principle. https://www.euro-fusion.org/news/detail/detail/News/tokamak-principle. Accessed: 2020-03-01.

[7] M. Weiland. *Influence of RF heating and MHD instabilities on the fast-ion distribution in ASDEX Upgrade*. Ph.D. thesis, Ludwig Maximilian University of Munich, Jan 2016.

[8] B. Geiger. *Fast-ion transport studies using FIDA spectroscopy at the ASDEX Upgrade tokamak*. Ph.D. thesis, Ludwig Maximilian University of Munich, Jan 2013.

[9] ITER Physics Expert Group on Energy Drive and ITER Physics Basis Editors. Chapter 5: Physics of energetic ions. *Nuclear Fusion*, 39(12):2471–2495, Dec 1999.

[10] F. Wagner et al. Regime of improved confinement and high beta in neutral-beam-heated divertor discharges of the ASDEX tokamak. *Phys. Rev. Lett.*, 49:1408–1412, Nov 1982.

[11] J. W. Connor, A. Kirk, and H. R. Wilson. Edge localised modes (ELMs): Experiments and theory. *AIP Conference Proceedings*, 1013(1):174–190, 2008.

[12] H. Kishimoto, M. Nagami, and M. Kikuchi. Recent results and engineering experiences from JT-60. *Fusion Engineering and Design*, 39-40:73 – 81, 1998.

[13] M. García-Muñoz et al. Fast-ion losses induced by ELMs and externally applied magnetic perturbations in the ASDEX Upgrade tokamak. *Plasma Physics and Controlled Fusion*, 55(12):124014, Nov 2013.

[14] D. Moseev, M. Salewski, M. Garcia-Muñoz, B. Geiger, and M. Nocente. Recent progress in fast-ion diagnostics for magnetically confined plasmas. *Reviews of Modern Plasma Physics*, 2(1):7, Sep 2018.

[15] A. Fasoli et al. Chapter 5: Physics of energetic ions. *Nuclear Fusion*, 47(6):S264–S284, Jun 2007.

[16] U. Stroth. *Plasmaphysik: Phänomene, Grundlagen, Anwendungen*. Vieweg+Teubner Verlag, 2011.

[17] M. Kraus. *Heiz-und stromprofile bei neutralteilcheninjektion in tokamakplasmen*. Diplomarbeit, Technische Universität München, Jul 2010.

[18] K. H. Berkner, R. V. Pyle, and J. W. Stearns. Intense, mixed-energy hydrogen beams for CTR injection. *Nuclear Fusion*, 15(2):249–254, Apr 1975.

[19] W. W. Heidbrink and G. J. Sadler. The behaviour of fast ions in tokamak experiments. *Nuclear Fusion*, 34(4):535–615, Apr 1994.

[20] T. H. Stix. Heating of toroidal plasmas by neutral injection. *Plasma Physics*, 14(4):367–384, Apr 1972.

[21] J. D. Huba. *NRL Plasma Formulary*. Naval Research Laboratory, Washington, DC, 2013.

[22] S. J. Zweben, R. L. Boivin, C-S. Chang, G. W. Hammett, and H. E. Mynick. Radial diffusion coefficient for counter-passing MeV ions in the TFTR tokamak. *Nuclear Fusion*, 31(12):2219–2245, Dec 1991.

[23] H. Zohm et al. MHD stability and disruption physics in ASDEX Upgrade. *Plasma Physics and Controlled Fusion*, 37(11A):A313–A324, Nov 1995.

[24] B. Streibl, P. T. Lang, F. Leuterer, J-M. Noterdaeme, and A. Stäbler. Chapter 2: Machine design, fueling, and heating in ASDEX Upgrade. *Fusion Science and Technology*, 44(3):578–592, 2003.

[25] E. Strumberger, S. Günter, E. Schwarz, and C. Tichmann. Fast particle losses due to NTMs and magnetic field ripple. *New Journal of Physics*, 10(2):023017, Feb 2008.

[26] V. Hynönen, T. Kurki-Suonio, W. Suttrop, and A. Stäbler and. Effect of radial electric field and ripple on edge neutral beam ion distribution in ASDEX Upgrade. *Plasma Physics and Controlled Fusion*, 50(3):035014, Feb 2008.

[27] W. Suttrop et al. Mitigation of edge localised modes with magnetic perturbations in ASDEX Upgrade. *Fusion Engineering and Design*, 88(6):446 – 453, 2013. Proceedings of the 27th Symposium On Fusion Technology (SOFT-27); Lige, Belgium, September 24-28, 2012.

[28] W. Suttrop et al. In-vessel saddle coils for MHD control in ASDEX Upgrade. *Fusion Engineering and Design*, 84(2):290 – 294, 2009. Proceeding of the 25th Symposium on Fusion Technology.

[29] M. García-Muñoz et al. Fast-ion redistribution and loss due to edge perturbations in the ASDEX Upgrade, DIII-D and KSTAR tokamaks. *Nuclear Fusion*, 53(12):123008, Nov 2013.

[30] L. Sanchis et al. Characterisation of the fast-ion edge resonant transport layer induced by 3D perturbative fields in the ASDEX Upgrade tokamak through full orbit simulations. *Plasma Physics and Controlled Fusion*, 61(1):014038, Nov 2018.

[31] A. J. Wootton et al. Fluctuations and anomalous transport in tokamaks. *Physics of Fluids B: Plasma Physics*, 2(12):2879–2903, 1990.

[32] E. J. Doyle et al. Chapter 2: Plasma confinement and transport. *Nuclear Fusion*, 47(6):S18–S127, Jun 2007.

[33] F. Ryter et al. Experimental evidence for gradient length-driven electron transport in tokamaks. *Phys. Rev. Lett.*, 86:2325–2328, Mar 2001.

[34] B. Geiger et al. Quantification of the impact of large and small-scale instabilities on the fast-ion confinement in ASDEX Upgrade. *Plasma Physics and Controlled Fusion*, 57(1):014018, Nov 2014.

[35] C. M. Muscatello et al. Velocity-space studies of fast-ion transport at a sawtooth crash in neutral-beam heated plasmas. *Plasma Physics and Controlled Fusion*, 54(2):025006, Jan 2012.

[36] B. Geiger et al. Fast-ion transport in the presence of magnetic reconnection induced by sawtooth oscillations in ASDEX Upgrade. *Nuclear Fusion*, 54(2):022005, Jan 2014.

[37] F. Wagner et al. Development of an edge transport barrier at the H-mode transition of ASDEX. *Phys. Rev. Lett.*, 53:1453–1456, Oct 1984.

[38] T. Casper et al. Development of the ITER baseline inductive scenario. *Nuclear Fusion*, 54(1):013005, Dec 2013.

[39] H. Zohm. Edge localized modes (ELMs). *Plasma Physics and Controlled Fusion*, 38(2):105–128, Feb 1996.

[40] T. E. Evans. ELM mitigation techniques. *Journal of Nuclear Materials*, 438:S11 – S18, 2013. Proceedings of the 20th International Conference on Plasma-Surface Interactions in Controlled Fusion Devices.

[41] P. T. Lang et al. ELM pace making and mitigation by pellet injection in ASDEX Upgrade. *Nuclear Fusion*, 44(5):665–677, Apr 2004.

[42] E. Wolfrum et al. Investigation of inter-ELM pedestal profiles in ASDEX Upgrade. *Plasma Physics and Controlled Fusion*, 51(12):124057, Nov 2009.

[43] A. Burckhart et al. Inter-ELM behaviour of the electron density and temperature pedestal in ASDEX Upgrade. *Plasma Physics and Controlled Fusion*, 52(10):105010, 2010.

[44] F. M. Laggner et al. Pedestal structure and inter-ELM evolution for different main ion species in ASDEX Upgrade. *Physics of Plasmas*, 24(5):056105, 2017.

[45] M. Cavedon et al. Pedestal and er profile evolution during an edge localized mode cycle at ASDEX Upgrade. *Plasma Physics and Controlled Fusion*, 59(10):105007, Aug 2017.

[46] G. A. Cottrell et al. Ion cyclotron emission measurements during JET deuterium-tritium experiments. *Nuclear Fusion*, 33(9):1365–1387, Sep 1993.

[47] J. Galdon-Quiroga et al. Beam-ion acceleration during edge localized modes in the ASDEX Upgrade tokamak. *Phys. Rev. Lett.*, 121:025002, Jul 2018.

[48] B. Geiger et al. Fast-ion transport in low density l-mode plasmas at TCV using FIDA spectroscopy and the TRANSP code. *Plasma Physics and Controlled Fusion*, 59(11):115002, Sep 2017.

[49] M. R. Tournianski, R. J. Akers, P. G. Carolan, and D. L. Keeling. Anisotropic fast neutral particle spectra in the MAST spherical tokamak. *Plasma physics and controlled fusion*, 47(5):671, 2005.

[50] R. Clary et al. A photodiode-based neutral particle bolometer for characterizing charge-exchanged fast-ion behavior. *Review of Scientific Instruments*, 83(10):10D713, 2012.

[51] Y. Feng and others. 3D edge modeling and island divertor physics. *Contributions to Plasma Physics*, 44(1-3):57–69, 2004.

[52] D. Reiter, M. Baelmans, and P. Börner. The eirene and B2-eirene codes. *Fusion Science and Technology*, 47(2):172–186, 2005.

[53] B. LaBombard. KN1D: A 1-D space kinetic, 2-D velocity, transport algorithm for atomic molecular hydrogen in an ionizing plasma. Research Report PSFC-RR-01-3, Massachusetts Institute of Technology, Plasma Science and Fusion Center, 175 Albany St., Cambridge, MA 02139 USA, 2001.

[54] J. Breslau et al. Transp. Technical report, Princeton Plasma Physics Lab.(PPPL), Princeton, NJ (United States), 2018.

[55] A. Pankin, D. McCune, R. Andre, G. Bateman, and A. Kritz. The tokamak Monte Carlo fast ion module NUBEAM in the National Transport Code Collaboration library. *Computer Physics Communications*, 159(3):157 – 184, 2004.

[56] S. Tamor. Antic: A code for calculation of neutral transport in cylindrical plasmas. *Journal of Computational Physics*, 40(1):104 – 119, 1981.

[57] R. J. Akers, E. Verwichte, T. J. Martin, S. D. Pinches, and R. Lake. GPGPU Monte Carlo calculation of gyro-phase resolved fast ion and n-state resolved neutral deuterium distributions. In *Proc. 39th EPS Conference on Plasma Physics*, page P5, 2012.

[58] R. Akers et al. High fidelity simulations of fast ion power flux driven by 3D field perturbations on ITER. In *26th IAEA Fusion Energy Conference*, 2018.

[59] A. Herrmann and O. Gruber. Chapter 1: ASDEX Upgrade - introduction and overview. *Fusion Science and Technology*, 44(3):569–577, 2003.

[60] G. F. Matthews. Plasma operation with an all metal first-wall: Comparison of an ITER-like wall with a carbon wall in jet. *Journal of Nuclear Materials*, 438:S2 – S10, 2013. Proceedings of the 20th International Conference on Plasma-Surface Interactions in Controlled Fusion Devices.

[61] B. Streibl, P. T. Lang, F. Leuterer, J-M. Noterdaeme, and A. Stäbler. Chapter 2: Machine design, fueling, and heating in ASDEX Upgrade. *Fusion Science and Technology*, 44(3):578–592, 2003.

[62] R. Neu et al. Impurity behaviour in the ASDEX Upgrade divertor tokamak with large area tungsten walls. *Plasma Physics and Controlled Fusion*, 44(6):811–826, May 2002.

[63] S. S. Denk et al. Shine-through in electron cyclotron emission measurements. In *44th EPS Conference on Plasma Physics*. European Physical Society, 2017.

[64] H. Murmann, S. Götsch, H. Röhr, H. Salzmann, and K. H. Steuer. The Thomson scattering systems of the ASDEX Upgrade tokamak. *Review of Scientific Instruments*, 63(10):4941–4943, 1992.

[65] A. Mlynek et al. Design of a digital multiradian phase detector and its application in fusion plasma interferometry. *Review of Scientific Instruments*, 81(3):033507, 2010.

[66] M. Willensdorfer et al. Characterization of the Li-BES at ASDEX Upgrade. *Plasma Physics and Controlled Fusion*, 56(2):025008, Jan 2014.

[67] R. Fischer et al. Integrated data analysis of profile diagnostics at ASDEX Upgrade. *Fusion Science and Technology*, 58(2):675–684, 2010.

[68] M. Griener et al. Qualification and implementation of line ratio spectroscopy on helium as plasma edge diagnostic at ASDEX Upgrade. *Plasma Physics and Controlled Fusion*, 60(2):025008, Dec 2017.

[69] R. M. McDermott et al. Extensions to the charge exchange recombination spectroscopy diagnostic suite at ASDEX Upgrade. *Review of Scientific Instruments*, 88(7):073508, 2017.

[70] G. Haas and H-S. Bosch. In vessel pressure measurement in nuclear fusion experiments with ASDEX gauges. *Vacuum*, 51(1):39 – 46, 1998.

[71] M. García-Muñoz, H-U. Fahrbach, H. Zohm, and the ASDEX Upgrade Team. Scintillator based detector for fast-ion losses induced by magnetohydrodynamic instabilities in the ASDEX Upgrade tokamak. *Review of Scientific Instruments*, 80(5):053503, 2009.

[72] P. A. Schneider et al. A new compact solid-state neutral particle analyser at ASDEX Upgrade: Setup and physics modeling. *Review of Scientific Instruments*, 86(7):073508, 2015.

[73] R. Bartiromo et al. Design and calibration of the jet neutral particle analyzer. *Review of Scientific Instruments*, 58(5):788–795, 1987.

[74] L. Giannone et al. Real-time diamagnetic flux measurements on ASDEX Upgrade. *Review of Scientific Instruments*, 87(5):053509, 2016.

[75] L. Giannone et al. Note: Internal diamagnetic flux measurements on ASDEX Upgrade. *Review of Scientific Instruments*, 89(10):106101, 2018.

[76] G. Tardini, C. Höhbauer, R. Fischer, and R. Neu and. Simulation of the neutron rate in ASDEX Upgrade H-mode discharges. *Nuclear Fusion*, 53(6):063027, May 2013.

[77] W. W. Heidbrink, K. H. Burrell, Y. Luo, N. A. Pablant, and E. Ruskov. Hydrogenic fast-ion diagnostic using Balmer-alpha light. *Plasma Physics and Controlled Fusion*, 46(12):1855–1875, Nov 2004.

[78] W. W. Heidbrink. Fast-ion dα measurements of the fast-ion distfribution (invited). *Review of Scientific Instruments*, 81(10):10D727, 2010.

[79] W. L. Wiese, M. W. Smith, and B. M. Miles. Atomic transition probabilities, nsrds-nbs 22, vol. *I1 Washington DC*, 1969.

[80] F. M. Levinton et al. Magnetic field pitch-angle measurments in the pbx-m tokamak using the motional Stark effect. *Phys. Rev. Lett.*, 63:2060–2063, Nov 1989.

[81] W. W. Heidbrink, D. Liu, Y. Luo, E. Ruskov, and B. Geiger. A code that simulates fast-ion d-alpha and neutral particle measurements. *Communications in Computational Physics*, 10(3):716741, 2011.

[82] M. Salewski et al. Tomography of fast-ion velocity-space distributions from synthetic CTS and FIDA measurements. *Nuclear Fusion*, 52(10):103008, Aug 2012.

[83] E. Schrödinger. Quantisierung als eigenwertproblem. *Annalen der Physik*, 385(13):437–490, 1 1926.

[84] M. A. Van Zeeland et al. Active and passive spectroscopic imaging in the DIII-D tokamak. *Plasma Physics and Controlled Fusion*, 52(4):045006, Mar 2010.

[85] A. Jansen van Vuuren et al. An edge fast-ion d-alpha system installed at ASDEX Upgrade. *Review of Scientific Instruments*, 90(10):103501, 2019.

[86] M. Czerny and A. F. Turner. Über den astigmatismus bei spiegelspektrometern. *Zeitschrift für Physik*, 61:792, Nov 1930.

[87] Y. Luo, W. W. Heidbrink, K. H. Burrell, D. H. Kaplan, and P. Gohil. Measurement of the d-alpha spectrum produced by fast ions in DIII-D. *Review of Scientific Instruments*, 78(3):033505, 2007.

[88] M. Weiland et al. Enhancement of the FIDA diagnostic at ASDEX Upgrade for velocity space tomography. *Plasma Physics and Controlled Fusion*, 58(2):025012, Jan 2016.

[89] M. Podestà, W. W. Heidbrink, R. E. Bell, and R. Feder. The NSTX fast-ion D-alpha diagnostic. *Review of Scientific Instruments*, 79(10):10E521, 2008.

[90] W. W. Heidbrink et al. Calibration techniques for fast-ion Dα diagnostics. *Review of Scientific Instruments*, 83(10):10D903, 2012.

[91] A. Kramida, Yu. Ralchenko, J. Reader, and NIST ASD Team. NIST Atomic Spectra Database (ver. 5.6.1), [Online]. Available: `https://physics.nist.gov/asd` [2019, May 23]. National Institute of Standards and Technology, Gaithersburg, MD., 2018.

[92] R. E. Bell. Exploiting a transmission grating spectrometer. *Review of Scientific Instruments*, 75(10):4158–4161, 2004.

[93] P. A. Schneider. *Characterization and scaling of the tokamak edge transport barrier*. Ph.D. thesis, Ludwig Maximilian University of Munich, 2012.

[94] L. C. Johnson and E. Hinnov. Ionization, recombination, and population of excited levels in hydrogen plasmas. *Journal of Quantitative Spectroscopy and Radiative Transfer*, 13(4):333 – 358, 1973.

[95] K. Mitosinkova et al. Direct determination of background neutral density profiles from neutral particle analyzers. In *45th EPS Conference on Plasma Physics*. European Physical Society, 2018.

[96] A. Kallenbach et al. Divertor power and particle fluxes between and during type-I ELMs in the ASDEX Upgrade. *Nuclear Fusion*, 48(8):085008, Jul 2008.

[97] P. Lauber, S. Günter, A. Könies, and S. D. Pinches. LIGKA: A linear gyrokinetic code for the description of background kinetic and fast particle effects on the MHD stability in tokamaks. *Journal of Computational Physics*, 226(1):447 – 465, 2007.

[98] M. García-Muñoz et al. MHD induced fast-ion losses on ASDEX Upgrade. *Nuclear Fusion*, 49(8):085014, Jul 2009.

[99] C. S. Collins et al. Observation of critical-gradient behavior in Alfvén-eigenmode-induced fast-ion transport. *Phys. Rev. Lett.*, 116:095001, Feb 2016.

[100] T. Pütterich, R. Dux, M. A. Janzer, and R. M. McDermott. ELM flushing and impurity transport in the H-mode edge barrier in ASDEX Upgrade. *Journal of Nuclear Materials*, 415(1, Supplement):S334 – S339, 2011. Proceedings of the 19th International Conference on Plasma-Surface Interactions in Controlled Fusion.

[101] G. T. A. Huysmans and O. Czarny. MHD stability in X-point geometry: simulation of ELMs. *Nuclear Fusion*, 47(7):659–666, Jun 2007.

[102] C. Cathey et al. Non-linear magnetohydrodynamic simulations of edge-localized-mode cycles in tokamak plasmas and their underlying triggering mechanism, In preparation.